To the Graduate Council:

I am submitting herewith a thesis written by Ho Jong Kang entitled "Structural Development and Residual Stresses in Thick Filament." I have examined the final copy of this thesis for form and content and recommend that it be accepted in partial fulfillment of the requirements for the degree of Master of Science, with a major in Polymer Engineering.

James L. White, Major Professor

We have read this thesis and recommend its acceptance:

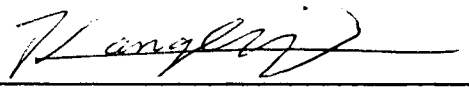
Accepted for the Council:

Vice Provost and
Dean of the Graduate School

STATEMENT OF PERMISSION TO USE

In presenting this thesis in partial fulfillment of the requirements for a Master's degree at The University of Tennessee, Knoxville, I agree that the Library shall make it available to borrowers under rules of the Library. Brief quotations from this thesis are allowable without special permission, provided that accurate acknowledgment of source is made.

Permission for extensive quotation from or reproduction of this thesis may be granted by my major professor, or in his absence, by the Head of Interlibrary Services when, in the opinion of either, the proposed use of the material is for scholarly purposes. Any copying or use of the material in this thesis for financial gain shall not be allowed without my written permission.

Signature 

Date Aug. 12 1985

STRUCTURAL DEVELOPMENT AND RESIDUAL STRESSES IN THICK FILAMENTS

A Thesis

Presented for the

Master of Science

Degree

The University of Tennessee, Knoxville

Ho Jong Kang

August 1985

This thesis is dedicated to my thoughtful parents,

SOONHO KANG, OKHI KIM

to my generous parents-in-law

MINDONG HAN, JUNGYAE SUH

and to my lovely devoted wife

JHEEYOUN

ACKNOWLEDGMENT

The author wishes to express sincere appreciation to his advisor, Professor James L. White, for his wisdom, stimulating discussions and encouragement during the course of this research.

The Polymer Engineering Center at The University of Akron made its facilities available and the experimental studies were carried out in almost their entirety. The faculty of the Polymer Engineering Center have provided useful suggestions and discussions of research.

The author thanks Professor A. I. Isayev, Professor Thein Kyu, Dr. Mukerrem Cakmak and Dr. Kyonsuku Min, for their advice, instruction and support that have helped him to achieve his academic goal.

Financial support was provided by a research assistantship from The University of Akron. This support is gratefully acknowledged.

Thanks are also extended to all the student colleagues, especially Chih-Hung Chen, Hideki Yamane, Yoshiyuki Suetsugu and Sangmoon Lee, for their help and suggestions.

Appreciation is also extended to the Polymer Engineering faculty, Professors Joseph E. Spruiell and Donald C. Bogue, for their advice.

Finally, the author wishes to express his deepest appreciation to his wife JheeYoun, his parents and his parents-in-law, for their encouragement and continuous support.

ABSTRACT

Orientation distribution and residual stresses are well known problems in fabricated polymeric parts. However, little concentrated effort has been made in this field. In this thesis, the study of orientation development and residual stress in thick melt spun filaments are reported. The influence of processing conditions on characteristics of orientation and thermal quenched stresses in melt spun fiber are emphasized.

The relationships between stress and birefringence were obtained. Amorphous and crystalline materials were both considered and interpretation carried out using Hermans' orientation factors. Birefringence distributions were measured by the wedge method. Predictions of birefringence distribution was carried out and then comparison was made between theoretical and experimental results.

Estimation of thermal quench stresses in melt spun fibers was attempted and results are interpreted. Fibrillation was observed in the melt spun fiber of glassy polymer. SEM and small-angle x-ray diffraction were used to characterize.

Special characterization efforts were made on polycarbonate fiber as well as polycarbonate film using DSC. A small amount of crystallinity was suspected in melt spun polycarbonate fiber. Several techniques were performed to crystallize the polycarbonate film and then characterize the degree of crystallinity in crystallized polycarbonate films.

TABLE OF CONTENTS

CHAPTER		PAGE
I.	INTRODUCTION	1
II.	BACKGROUND REVIEW AND LITERATURE SURVEY	3
2.1.	Definition of Uniaxial Orientation	3
2.2.	Measurement of Orientation	5
2.2.1.	Birefringence	5
2.2.2.	Wide Angle X-ray Scattering	19
2.2.3.	Infrared Dichroism	20
2.3.	Orientation Development in Flow of Polymer Melt	21
2.4.	Dynamics and Heat Transfer of Fiber Spinning .	23
2.4.1.	Force Balance	23
2.4.2.	Heat Transfer	26
2.5.	Orientation in Fabricated Glassy Polymers . . .	32
2.5.1.	Fibers	32
2.5.2.	Other Fabricated Operations	33
2.6.	Orientation and Morphology in Crystallized Polymers	34
2.6.1.	Melt Spinning Fibers	34
2.6.2.	Other Fabrication Operations	36
2.7.	Residual Stresses (Thermal Quench Stresses) . .	36
2.7.1.	Theory of Transient Thermal Stresses .	37
2.7.2.	Theory of Thermal Quenched Stresses . .	39
2.7.3.	Residual Stresses Effect on Polymer Properties	41
III.	EXPERIMENTAL	43
3.1.	Material	43
3.2.	Fiber Processing	43
3.3.	Preparation of Crystallized Polycarbonate Samples	48
3.4.	Mean Birefringence Measurement	52
3.5.	Birefringence Distribution Measurement	54
3.6.	Experiments for Structural Changes in Fibers .	58
3.6.1.	Measurements of Crystallinity	58
3.6.2.	Fibrillation Experiments	61
IV.	STRUCTURE DEVELOPMENT IN SPUN FILAMENTS	63
4.1.	Mean Birefringence	63

CHAPTER PAGE

4.1.1. Results 63
4.1.2. Discussion 69
4.2. Birefringence Distribution Across the Thickness Direction 77
4.2.1. Results 77
4.2.2. Discussion 81

V. ANALYSIS OF SPINNING DYNAMICS AND ORIENTATION IN THE THICK FILAMENT 88

5.1. Prediction of Spinning Dynamics 88
5.1.1. Approach 88
5.1.2. Results and Discussion 92
5.2. Prediction of Mean Orientation and Orientation Distribution 95
5.2.1. Approach 95
5.2.2. Results and Discussion 103

VI. CRYSTALLIZATION OF A POLYCARBONATE 110

6.1. Introduction 110
6.2. Results 112
6.3. Discussion 114

VII. FIBRILLATION IN MELT SPUN POLYSTYRENE AND POLYCARBONATE FIBERS 118

7.1. Introduction 118
7.2. Results 119
7.3. Discussion 119

VIII. ESTIMATION OF THERMAL QUENCH STRESSES 126

8.1. Approach 126
8.2. Discussion 133

IX. SUMMARY AND CONCLUSION 142

REFERENCES 144

APPENDIX. COMPUTER PROGRAMS 154

VITA 164

LIST OF TABLES

TABLE		PAGE
III-1.	Processing Conditions Which Were Used in This Study	44
III-2.	Physical Constants for Cooling Media	46
IV-1.	Ratio of Stress-Optical Coefficient to Intrinsic Birefringence (PS, PC, PET, PP, PE)	78
V-1.	Physical Constants for PS and PC	91
VI-1.	Crystallinity and Melting Range of Polycarbonate in Different Crystallization Procedures	116
VIII-1.	Physical Constants for PS and PC to Calculate Residual Stresses	130

LIST OF FIGURES

FIGURE		PAGE
II-1.	Optical System to Determine the Birefringence	9
II-2.	Typical Interference Patterns on the Fiber Between Crossed Polarizers (Upper Half) and Parallel Polarizers (Lower Half)	11
II-3.	Cross Section of a Monofilament Showing the Variables Used in the Mathematical Development . . .	13
II-4.	Diagram of a Cone on the End of a Monofilament . . .	14
II-5.	Diagram of Wedge on the End of a Monofilament	16
II-6.	Typical Distribution of Birefringence in a Fiber . .	18
II-7.	Scheme of the Melt Spinning	24
III-1.	Melt Spinning Scheme with Different Quench Conditions	47
III-2.	Bending Moment at the Tensiometer	49
III-3.	Equipment Setup for Fiber Calibration	50
III-4.	Relationship Between Calibrated Stress and Birefringence at Air Cooling with Water Bath and Without Water Bath	51
III-5.	Sample Positions on a Microscopy Stage for PS, PC and PP	53
III-6.	Cut Fiber With a Desired Angle to Measure a Birefringence Distribution	55
III-7.	Mold and Fiber Containing Epoxy Slab	56
III-8.	Typical Fringe Pattern on the Wedge	57
III-9.	Calculation of Retardation from Fringe Patterns . . .	59
III-10.	Typical Retardation Distribution Along the Diameter Direction	60

FIGURE		PAGE
III-11.	Sample Preparation for SAXS. (a) Sample Holder; (b) Mounted Sample	62
IV-1.	Birefringence Versus Drawdown Ratio at Different Processing Conditions for Polystyrene Fibers	64
IV-2.	Birefringence Versus Drawdown Ratio at Different Processing Conditions for Polycarbonate Fibers . . .	65
IV-3.	Birefringence Versus Drawdown Ratio at Different Processing Conditions for Polypropylene Fibers . . .	66
IV-4.	Cooling Condition Effects on Birefringence (PS) . . .	67
IV-5.	Cooling Condition Effects on Birefringence (PC) . . .	68
IV-6.	Relationship Between Applied Stress and Birefringence for Polystyrene Fibers	70
IV-7.	Relationship Between Applied Stress and Birefringence for Polycarbonate Fibers	71
IV-8.	Relationship Between Applied Stress and Birefringence for Polypropylene Fibers	72
IV-9.	Comparison About the Relationship Δn and Stress for PC, PS and PET Fibers	75
IV-10.	Orientation Factors as a Function of Stress for Amorphous Polymer and Crystallized Melt Spun Fiber	76
IV-11.	Typical Fringe Patterns on Wedge for Polystyrene Fibers	79
IV-12.	Typical Fringe Patterns on Wedge for Polycarbonate Fibers	80
IV-13.	Birefringence Distributions for Polystyrene Fibers. (Drawdown Ratio = 127)	82
IV-14.	Birefringence Distributions for Polystyrene Fibers. (Drawdown Ratio = 60)	83
IV-15.	Birefringence Distributions for Polycarbonate Fibers. (Drawdown Ratio = 127)	84

FIGURE PAGE

IV-16. Birefringence Distributions for Polycarbonate Fibers. (Drawdown Ratio = 60) 85

IV-17. Birefringence Distributions for Polycarbonate Fibers. (Air Cooling) 86

V-1. Predicted Radius Profile Along the Spinline for PS Fibers 93

V-2. Predicted Radius Profile Along the Spinline for PC Fibers 94

V-3. Predicted Velocity Profile Along the Spinline for PS Fibers 96

V-4. Predicted Velocity Profile Along the Spinline for PC Fibers 97

V-5. Predicted Temperature Profile Along the Spinline for PS Fibers 98

V-6. Predicted Temperature Profile Along the Spinline for PC Fibers 99

V-7. Predicted Heat Transfer Coefficient Profile Along the Spinline for PS Fibers 100

V-8. Predicted Heat Transfer Coefficient Profile Along the Spinline for PC Fibers 101

V-9. Mean Birefringence Versus Drawdown Ratio for Polystyrene Fibers 105

V-10. Mean Birefringence Versus Drawdown Ratio for Polycarbonate Fibers 106

V-11. Orientation Distribution for Polystyrene Fibers . . . 108

V-12. Orientation Distribution for Polycarbonate Fibers . . 109

VI-1. DSC Results for Polycarbonate Fibers 111

VI-2. DSC Results for Heat Treated Polycarbonate Films at 175°C 113

VI-3. DSC Results for Acetone Treated Polycarbonate Films (3 Days Acetone Treated) 115

FIGURE		PAGE
VII-1.	SEM Photomicrographs of Peeled Polystyrene Fibers	120
VII-2.	SEM Photomicrographs of Peeled Polycarbonate Fibers	121
VII-3.	SEM Photomicrographs of Peeled PS and PC Fibers . . .	122
VII-4.	SEM Photomicrographs of Peeled Fibers	123
VII-5.	SAXS Patterns for Fibers (HPC, PC, PS, CAB)	124
VIII-1.	Value of $(1 - \nu)\sigma_r/E\alpha(T - T_a)$ and $(1 - \nu)\sigma_\theta/E\alpha(T - T_a)$ as a Function of $K\ t^*/R^2\rho C_p$ (Nusselt No. = 5)	131
VIII-2.	Value of $(1 - \nu)\sigma_r/E\alpha(T - T_a)$ and $(1 - \nu)\sigma_r/E\alpha(T - T_a)$ as a Function of $K\ t^*/R^2\rho C_p$ (Nusselt No. = 0.1) . . .	132
VIII-3.	Residual Stresses for Polystyrene Fibers (Air Cooling)	135
VIII-4.	Residual Stresses for Polystyrene Fibers (Ice Water Cooling)	136
VIII-5.	Residual Stresses for Polystyrene Fibers (Isopropanol Cooling)	137
VIII-6.	Residual Stresses for Polycarbonate Fibers (Air Cooling)	138
VIII-7.	Residual Stresses for Polycarbonate Fibers (Ice Water Cooling)	139
VIII-8.	Residual Stresses for Polycarbonate Fibers (Isopropanol Cooling)	140

CHAPTER I

INTRODUCTION

Polymeric products are generally made by the deformation and shaping of materials in the molten state. Solidification of fabricated parts whether filaments during melt spinning or in mold occurs slowly through the thickness from the outside in. Nonuniform solidification insures nonuniform orientation distribution, and the development of thermal quench stresses. This nonuniform orientation distribution and residual stresses have a major effect on the properties of fabricated products.

In most investigations of fabricated polymeric parts, orientation has been considered uniform through the cross section. While various researchers have noted such nonuniformity there has been little concentrated effort at attacking the general problem. The thermal quench residual stresses which also arise during processing have similarly received only limited treatment.

In this thesis, we are concerned with distribution of orientation and thermal quench stresses through the thickness of fabricated polymeric products.

We specifically investigate the distribution of orientation in filaments as a function of process conditions and seek to interpret them in terms of mathematical models of orientation development and solidification. We also model the residual stresses of thick fibers.

We seek to develop a perspective of the influence of processing conditions on characteristics of orientation and thermal quench stresses in melt spun filaments. Our efforts emphasize three polymers: polystyrene, polycarbonate and polypropylene.

CHAPTER II

BACKGROUND REVIEW AND LITERATURE SURVEY

2.1. DEFINITION OF UNIAXIAL ORIENTATION

Uniaxial orientation refers to orientation with cylindrical symmetry. Serious studies of orientation in polymers date to the work of Preston (125), Morey (104) and Sisson (146) in the early 1930s. P. H. Hermans and his co-workers (63, 64, 65, 66) reported the first adequate quantification of uniaxial molecular orientation. They specified orientation through the anisotropy of polarizability.

$$f_H = \frac{\overline{\alpha_1 - \alpha_2}}{\Delta\alpha^0} \qquad [2\text{-}1]$$

where α_1 and α_2 are the mean polarizabilities in the axial and radial directions $\Delta\alpha^0$ is the difference in polarizability along and perpendicular to a polymer chain. They show that f_H can be expressed through the angle ϕ_{c1} between the fiber axis and the polymer chain axis.

$$f_H = \frac{3\,\overline{\cos^2\phi_{c1}} - 1}{2} \; . \qquad [2\text{-}2]$$

Hermans and Platzek (64) showed that f_H can be determined by birefringence.

$$f_H = \frac{\Delta n}{\Delta^0} \qquad [2\text{-}3]$$

where Δ^0 is the intrinsic birefringence. Hermans et al. also show how f_H may be determined in crystalline material using wide angle x-ray diffraction (66) and for specific chemical groups by dichroism (47, 150).

Muller (108) considered the orientation distribution in uniaxially oriented polymers. He represented the orientation distribution about a preferred axis in terms of an expansion of even Legendre spherical harmonic functions $P_n(\overline{\cos\theta}_c)$. The first two terms are:

$$P_2(\cos\theta_{c1}) = \frac{1}{2}(3\,\overline{\cos^2\theta}_1 - 1) \qquad [2\text{-}4a]$$

$$P_4(\cos\theta_{c2}) = \frac{35}{8}\,\overline{\cos^4\theta}_1 - \frac{15}{4}\,\overline{\cos^2\theta}_1 + \frac{3}{8}\,. \qquad [2\text{-}4b]$$

The term in P_2 can be seen to be the Hermans orientation factors. Nomura and Kawai (113, 114, 115) and Roe and Krigbaum (129, 130, 87) expand these views.

Stein (150, 151) generalized the Hermans orientation factor to the three crystallographic axes in a crystalline polymer. He wrote

$$f_a = (3\,\overline{\cos^2\phi}_{a1} - 1)/2 \qquad [2\text{-}5a]$$

$$f_b = (3\,\overline{\cos^2\phi}_{b1} - 1)/2 \qquad [2\text{-}5b]$$

$$f_c = (3\,\overline{\cos^2\phi}_{c1} - 1)/2\,. \qquad [2\text{-}5c]$$

For an orthorhombic unit cell, the three axes are

$$\cos^2\phi_{a1} + \cos^2\phi_{b1} + \cos^2\phi_{c1} = 1 \qquad [2\text{-}6]$$

so

$$f_a + f_b + f_c = 0 \ . \qquad [2\text{-}7]$$

Thus the three f's are not independent and only two of them are necessary to characterize the orientation of the three crystallographic axes.

2.2. MEASUREMENT OF ORIENTATION

The primary methods used to characterize orientation are birefringence, wide-angle x-ray scattering and infrared dichroism (47, 76, 150, 151). Fluorescence (16, 35), laser Raman scattering (16, 77), sound-velocity measurement (36, 167) and nuclear magnetic resonance (100) have also been used. They refer to effects resulting partly from chain orientation, partly from crystalline orientation and partly from a combination of these.

2.2.1. Birefringence

2.2.1.1. General. The interaction of isotropic material with light waves is determined by a single constant, a refractive index "n" defined by

$$n = c/v \qquad [2\text{-}8]$$

where c is the velocity of light in a vacuum and v is the velocity of light in a medium. In anisotropic materials such as oriented polymer systems, this refractive index is a second order tensor with components.

$$\bar{n} = \begin{vmatrix} n_{11} & n_{12} & n_{13} \\ n_{12} & n_{22} & n_{23} \\ n_{13} & n_{23} & n_{33} \end{vmatrix} = \begin{vmatrix} n_1 & 0 & 0 \\ 0 & n_2 & 0 \\ 0 & 0 & n_3 \end{vmatrix} \qquad [2\text{-}9]$$

where the second matrix corresponds to the principal axis form. The difference between each pair of the principal refractive indices is called the birefringence Δn.

There is a basic relationship between molecular orientation and the optical properties of a homogeneous polymer. The partial alignment of polymer chains during orientation produces a difference between the electronic polarizability in the direction of stretch and that in the direction perpendicular to the stretch. The birefringence method of measurement of orientation presumes

$$\frac{n_1 - n_2}{\Delta^0} = \frac{\alpha_1 - \alpha_2}{\Delta\alpha^0} \; . \qquad [2\text{-}10]$$

One justification of this is through the Lorentz-Lorentz equation (90, 15) which relates refractive index to polarizability in isotropic materials

$$\frac{n^2 - 1}{n^2 + 2} = \frac{4}{3} \pi \frac{N\rho\alpha}{M} \qquad [2\text{-}11]$$

where α is the molecular polarizability, N is the Avogadro's number, ρ is density and M is the molecular weight per structure unit. This equation has been proposed by Kuhn and Grun (88) and later investigators to be valid for the component polarizabilities and refractive indices in two different directions.

$$\frac{n_1^2 - 1}{n_1^2 + 2} - \frac{n_2^2 - 1}{n_2^2 + 2} = \frac{4}{3} \pi \frac{N\rho}{M} (\alpha_1 - \alpha_2) \ . \qquad [2\text{-}12]$$

For small values of the birefringence $(n_1 - n_2)$ we make use of the approximation

$$\left(\frac{n_1^2 - 1}{n_1^2 + 2} - \frac{n_2^2 - 1}{n_2^2 + 2}\right) \simeq \frac{6\bar{n}}{(\bar{n}^2 + 2)^2} (n_1 - n_2) \qquad [2\text{-}13]$$

where $\bar{n}$ is the arithmetic average of n_1 and n_2. So we can express the Lorentz-Lorentz by

$$\Delta n = (n_1 - n_2) = \frac{2}{9} \pi N(\bar{n}^2 + 2)^2(\alpha_1 - \alpha_2) \ . \qquad [2\text{-}14]$$

This is the desired relation between birefringence and polarization anisotropy.

There are two primary methods to measure mean birefringence: (a) measurement of refractive indices; (b) measurement of retardation. The former method is only readily applicable to films or slabs and is generally applied using an Abbe refractometer (134, 136, 137). The retardation method involves determination of the phase lay between

the two waves, corresponding to the two refractive indices, which propagate through the material. This procedure is generally applied to determine birefringence in filaments. Experiments make use of an optical system of the type shown in Figure II-1 where a polarizer, analyzer and detection system are used. The detector may determine total intensity or retardation.

If the intensity is measured then, Δn is determined from

$$I = C \sin^2(\pi \Delta n \, d/\lambda) \qquad [2\text{-}15]$$

where λ is the wavelength of light and C is a constant depending on the intensity of the entering beam and the angle between the principal axis of the sample and the optic axis of the polarizer. The retardation Γ is expressed as

$$\Gamma = \Delta n \, d \qquad [2\text{-}16]$$

where Γ is retardation and d is the thickness of the sample.

Retardation may be conveniently measured using a compensator such as Babinet, Soleil and Berek type (78, 157).

The most widely used compensator is that of Babinet which consists of two quartz wedges whose optical axes are aligned perpendicular to each other. By sliding these relative to each other so that one has thickness x_1 and the other x_2, retardation of magnitude

$$\Gamma = \frac{2\pi}{\lambda} (n_e - n_o)(x_1 - x_2) \qquad [2\text{-}17]$$

may be introduced. A Berek compensator uses a rotating crystal plat.

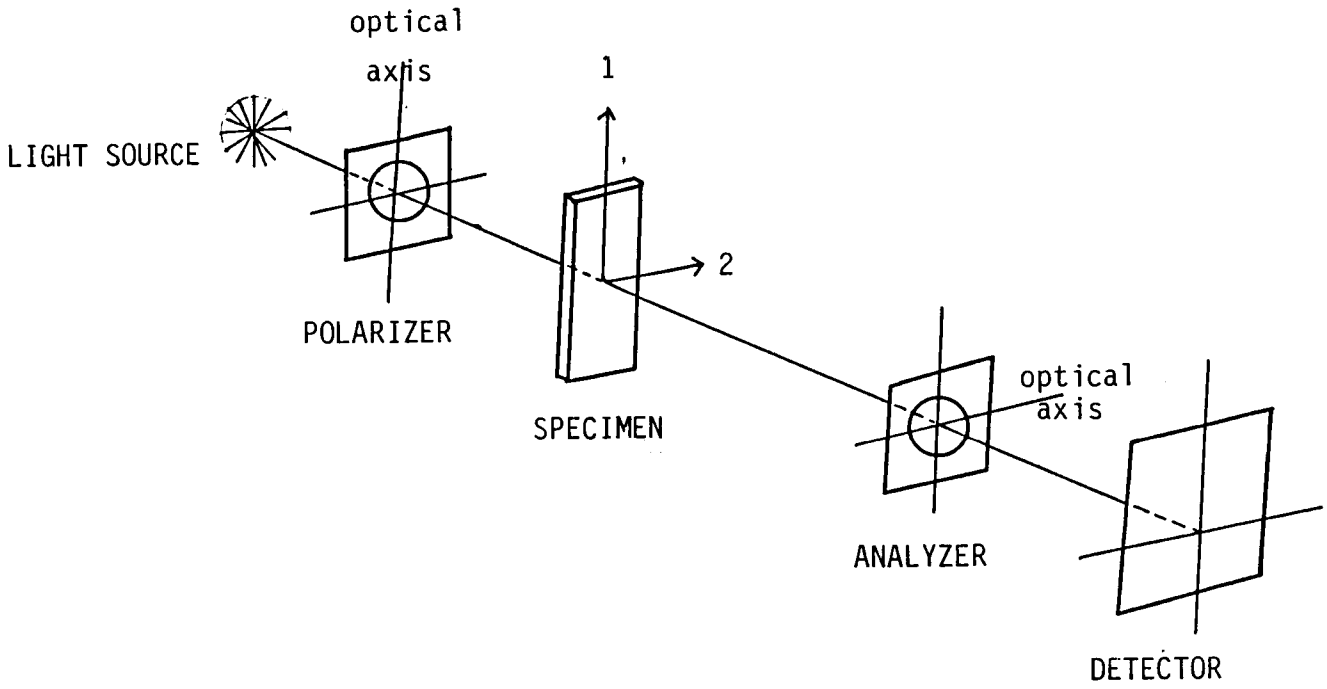


Figure II-1. Optical system to determine the birefringence.

2.2.1.2. Birefringence distribution. When a filament is examined between crossed polarizers using monochromatic light, with the filament axis at an angle of 45° with respect to the optic axes of the polarizer, dark bands are seen where the retardation equals the integral number of wavelengths. It means that

$$\Gamma = N\lambda \qquad [2\text{-}18]$$

where N is zero. This is called zero order fringe. When N is unity we have first order fringe, etc. To evaluate the magnitude of the local birefringence it is necessary to know the order of the fringes. Figure II-2 shows typical interference patterns in an oriented fiber. Kolb and Sturkey (86) have proposed a method for analyzing the interference patterns of an oriented filament which does not require a knowledge of the order of the fringes. Cleereman, Karam, and Williams (25) have also used this method. In this method, the thickness of the sample is calculated at the points where two adjacent fringes are located. Since the difference between two adjacent fringes is one wavelength and the difference in thickness is known, an average birefringence for the part of the sample between the two fringes can be calculated from the equation.

$$\Delta n = \lambda/t_i - t_{i-1} \qquad [2\text{-}19]$$

where λ is the wavelength of the light and $t_i - t_{i-1}$ is the difference in thickness. However, it is impossible to exactly specify to which integral multiple each fringe corresponds. This is because it is not

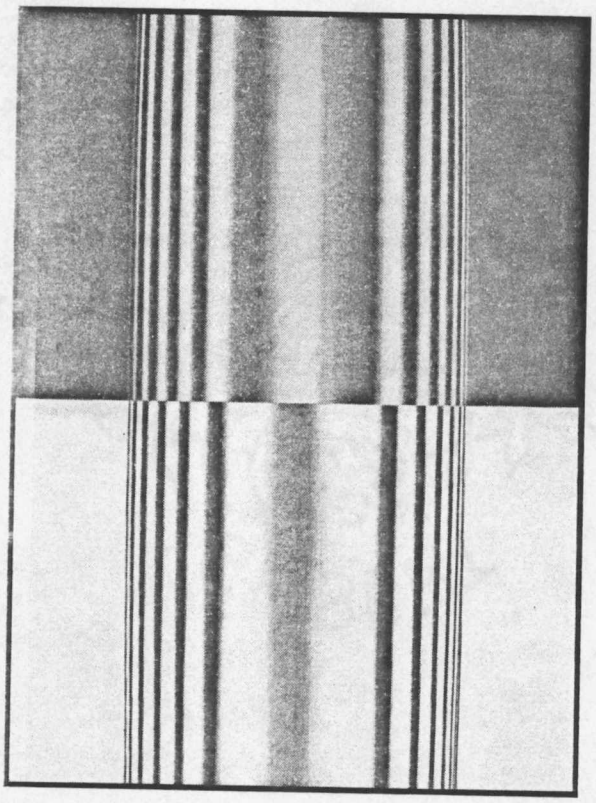


Figure II-2. Typical interference patterns on the fiber between crossed polarizers (upper half) and parallel polarizers (lower half).

possible to resolve the fringe near the edge, and because the radial variation of birefringence is not a known function.

Andrews (8) and Gurnee (54) have developed a method which is desirable that not only gives the location of the fringes, but also unambiguously gives the order of each fringe. They have proposed that the birefringence in a filament is in general a function of the radial distance from the central axis. If the birefringence at any point r on the radius vector is given by the function D(r), then the retardation through the element of vertical distance dr at the fixed point y is given by

$$\Gamma(y) = 2 \int_{r}^{R} (r^2 - y^2)^{-1/2} D(r) \cdot r \, dr \, . \qquad [2\text{-}20]$$

This is illustrated schematically in Figure II-3. If the retardation is divided by the optical path length P, one obtains an average birefringence

$$\Delta n_{av} = \frac{\Gamma(y)}{P(y)} = \frac{\int_{y}^{R} (r^2 - y^2)^{-1/2} D(r) \, r \, dr}{(R^2 - y^2)^{1/2}} \, . \qquad [2\text{-}21]$$

Gurnee (54) described two methods of determining the birefringence distribution in filament D(r), or n(r).

(i) Cone Method

Consider an oriented filament that has been cut cone shaped at one end as shown in Figure II-4. The fringe pattern through a cone with uniform distribution of birefringence is a series of

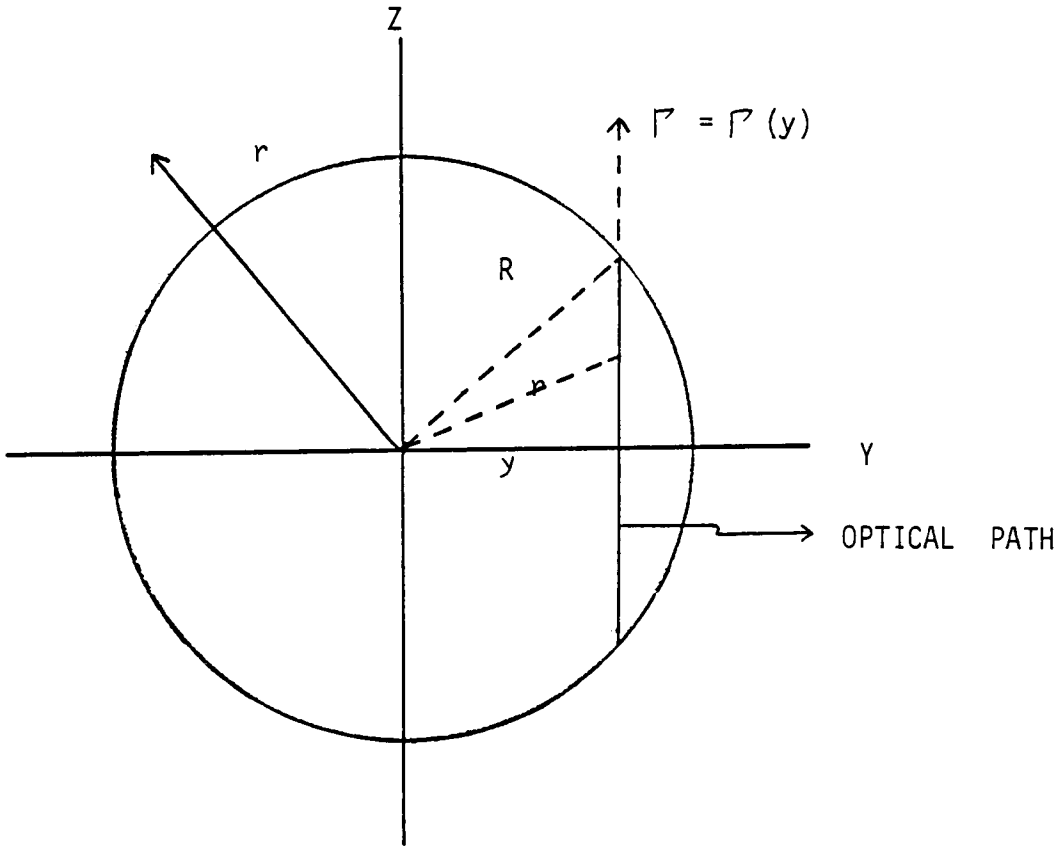


Figure II-3. Cross section of a monofilament showing the variables used in the mathematical development.

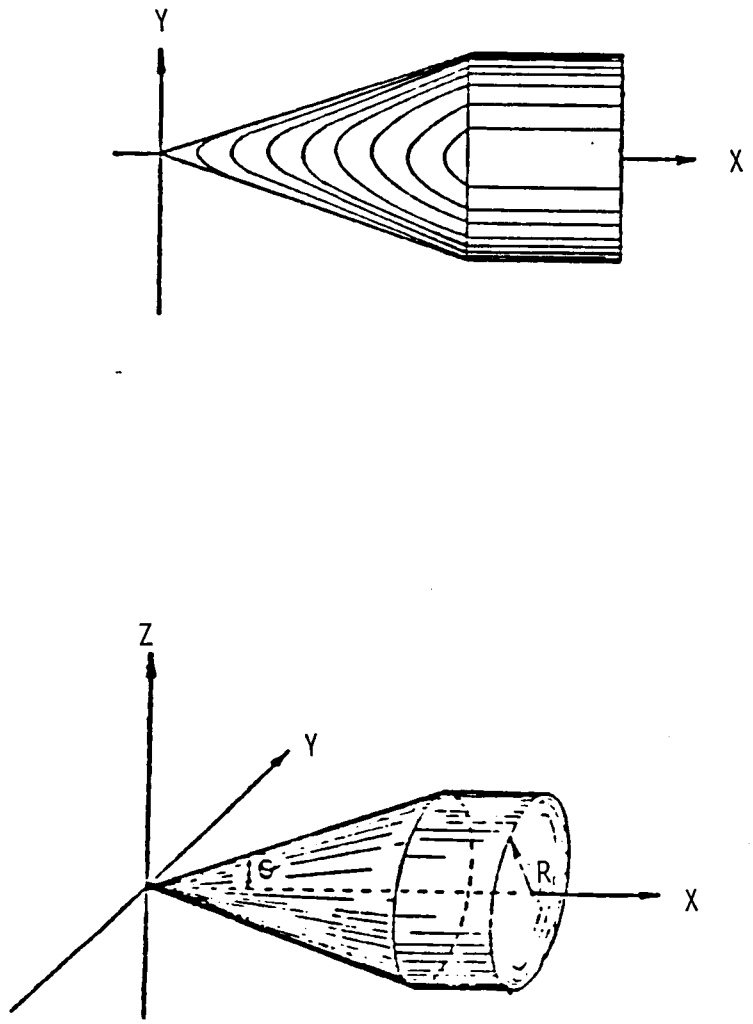


Figure II-4. Diagram of a cone on the end of a monofilament.

hyperbolas. These hyperbolas all have the same asymptote, namely, $y = \pm x \tan\theta$, which is the equation for the projection of the cone itself onto the x,y plane. If the birefringence through the original filament is not uniform but is given by the function D(r), then the retardation at any point (x,y) on the cone is given by

$$\Gamma_{xy} = \int_{y}^{x \tan\theta} (r^2 - y^2)^{-1/2} D(r) \cdot r \, dr \, . \qquad [2\text{-}22]$$

Consider only those points for which y = 0. Then

$$\Gamma_{x,0} = 2 \int_{0}^{x \tan\theta} D(r) \, dr \qquad [2\text{-}23]$$

and consequently

$$D(r) = \frac{1}{2} \cot\theta \frac{d\Gamma_{x,0}}{dx} \, . \qquad [2\text{-}24]$$

The quantity $\Gamma_{x,0}$ is determined experimentally from the fringe pattern on the cone. Equation [2-24] applied to a "double wedge" with its apex at the center of the filament. This is also rather difficult to form but it immediately suggests simply cutting the monofilament at an angle and using a "single wedge."

(ii) Wedge Method

Consider a filament cut at an angle as shown in Figure II-5. For the case of uniform distribution of birefringence it is shown that the fringes have the shape of the projection of the surface of the wedge onto the xy plane and are equally spaced along the x axis.

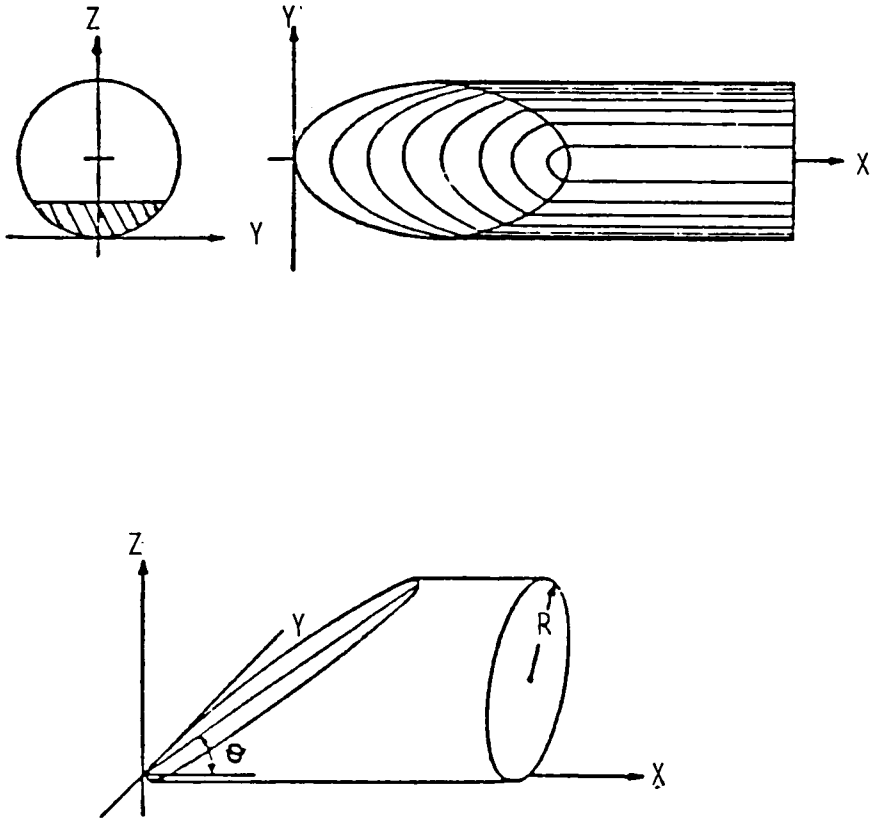


Figure II-5. Diagram of wedge on the end of a monofilament.

Since we only consider points within the wedge, the fringes obtained are only the portions of these equally spaced ellipses that are cut off by the wedge. If the birefringence is not uniform, we obtain Equation [2-25] in the manner similar to the derivation of Equation [2-24].

$$D(z) = \cot\theta \frac{d\Gamma_{x,0}}{dx} . \qquad [2\text{-}25]$$

In determining the birefringence by the wedge or cone method it is not necessary to know the order of the fringes; the only requirement is that the fringe order is continually increasing as the thickness through the wedge or cone increases. Figure II-6 is a typical curve of Δn versus the diameter of filament. This general form of curve—with higher birefringence at the edges than in the center—was explained in terms of cooling rate during the fabrication process.

More recently various investigators (49, 84) have suggested that the use of interference microscopy.

The interference microscopy is microscopy where the light paths are manipulated and phase changes introduced to increase the contrast to allow accurate determination of optical path difference, i.e., the product of the light "physical" path through the specimen, at a given point, and the difference between refractive indices in the sample and in the reference medium

$$(n - n_0)\ell = \frac{d}{D} \lambda \qquad [2\text{-}26]$$

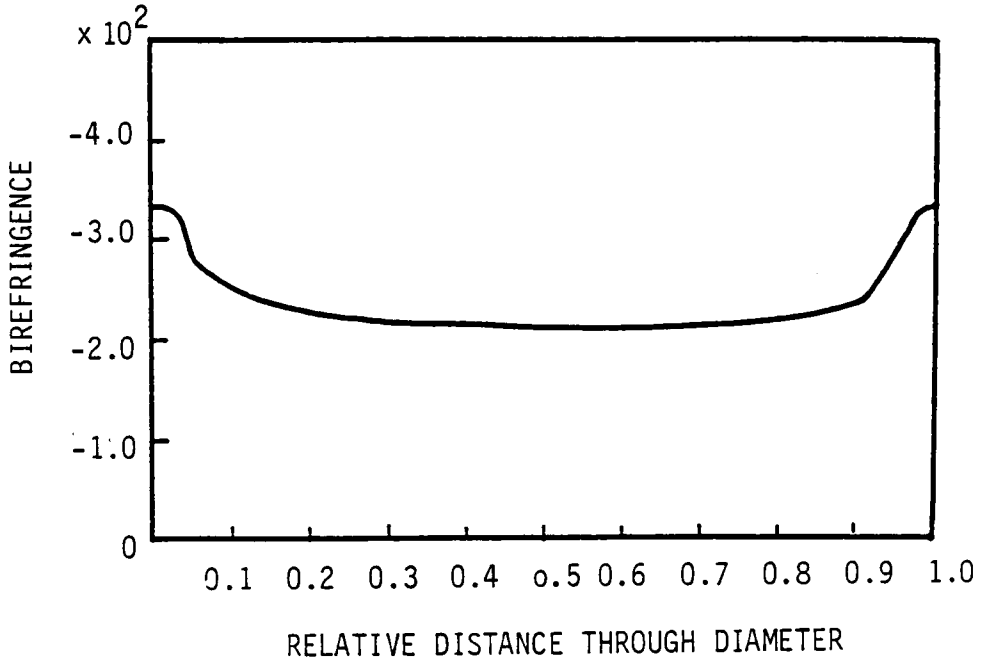


Figure II-6. Typical distribution of birefringence in a fiber.

where d is the fringe displacement due to the sample at a certain point, D is the inter-band distance due to the reference medium, ℓ is a light path through the sample and n_0 is a reflex index in the reference medium. This can be rewritten

$$n = n_0 + \frac{d}{D}\frac{\lambda}{\ell} . \qquad [2\text{-}27]$$

It is seen that n, λ are generally known and d, D are measured directly. In the case of fiber, ℓ can be calculated if one assumes the fiber to be cylindrical and r measures distance from center, then the chord ℓ is simply

$$\ell = 2(R^2 - r^2)^{1/2} . \qquad [2\text{-}28]$$

2.2.2. Wide Angle X-ray Scattering (6)

The most direct useful method of studying orientation in crystalline polymer is the x-ray diffraction technique. This technique can give us the complete orientation distribution function.

Hermans et al. (66) described how f_H could be determined for crystalline polymer through wide angle x-ray diffraction. More general treatment was offered which permits preferential orientation of all three of the crystallographic axes with respect to the stretching direction by Stein (151). If intense diffraction occurs from crystal planes perpendicular to a, b, c, crystal axes, the $\cos\phi$ value of Equation [2-5a,b,c] are given by

$$\overline{\cos^2\phi} = \frac{\int_0^{\pi} I_{hk\ell}(\phi)\cos^2\phi\sin\phi \, d\phi}{\int_0^{\pi} I_{hk\ell}(\phi) \sin\phi \, d\phi} \qquad [2\text{-}29]$$

where $I_{hk\ell}(\phi)$ is the intensity diffracted from an appropriate plane and ϕ is the angle between this plane normal and fiber axis. If there are no reflections available for planes perpendicular to chain axes, we must use a method due to Wilchinsky (162) and Sack (131). Wilchinsky has modified the treatment so as to make it applicable to nonorthogonal crystal systems and shown how a desired $(\overline{\cos^2\phi})$ function can be determined even in the absence of reflecting planes normal to the chosen crystallographic direction. Wilchinsky (161) and Sack (131) later used this method.

2.2.3. Infrared Dichroism (76)

Anisotropic absorption of radiation by oriented polymers provides method of determining independently the molecular orientation both in the crystalline and amorphous phases of polymers. The absorption of infrared radiation by a polymer can be given in terms of the absorbance A according to

$$A = \log_{10} I_0/I_{\alpha}(\underset{\sim}{M} \cdot \underset{\sim}{E})^2 \qquad [2\text{-}30]$$

where I_0 and I are the incident and transmitted intensities of the absorbing frequency, $\underset{\sim}{M}$ is the transition moment vector of normal mode and $\underset{\sim}{E}$ is the electric field.

If the structural units and their associated transition moments are nonrandomly oriented within the polymer, it follows the observed net absorbance will vary with the direction of $\underset{\sim}{E}$. The above effect is called dichroism and is represented by the ratio of sample absorbance measured with electric vectors.

$$R = A_{\parallel}/A_{\perp} \qquad [2\text{-}31]$$

The dichroic ratio R has been related to the orientation of molecular chains by various investigators (13, 46, 48, 171). Their results may be expressed

$$f = \frac{(R - 1)(R_0 + 2)}{(R_0 - 1)(R + 2)} \qquad [2\text{-}32]$$

where R_0 is the dichroic ratio for a completely oriented sample.

2.3. ORIENTATION DEVELOPMENT IN FLOW OF POLYMER MELT

Brewster (17) showed that birefringence was produced by application of stresses to a variety of materials including rubber and inorganic glass. The rheo-optical law which has the form:

$$\underset{\sim}{n} = \frac{1}{3}(\mathrm{tr}\underset{\sim}{n})\underset{\sim}{I} + C\underset{\sim}{P} \qquad [2\text{-}33a]$$

$$n_i - n_j = C(\sigma_i - \sigma_j) = C(P_i - P_j) \qquad [2\text{-}33b]$$

where $\underset{\sim}{n}$ is the refractive index tensor, $\underset{\sim}{I}$ is the unit tensor, $\underset{\sim}{P}$ is the deviatoric stress tensor, C is the stress-optical coefficient and

$\underset{\sim}{\sigma}$ is total stress tensor was developed quantitatively by Clerk Maxwell and applied to photoelastic stress analysis. This law was well established by researchers who developed photoelastic stress analysis using inorganic glasses and amorphous polymers. Lodge (94) was the first to suggest that the rheo-optical law could be applied to polymer solution and melts. Philippoff (110) showed the validity of the rheo-optical law for a range of polymer solutions. Equation [2-33] has been checked in steady shear flow by Wales (158) for many polymer melts over a wide range of shear rates. The first critical attempt to check this hypothesis under transient condition was made by Janeschitz-Kriegl and Gortemaker (73). This approach was used by Bogue and Peebles (14), Adams et al. (3), Janechitz-Kriegle (75), Han and Drexler (57), Gortemaker et al. (52), Wales (159), Han and his co-worker (58, 170), Brizitsky et al. (18) and Arai and his team (8) to determine the birefringence profiles in polymer melts flowing through two-dimensional dies of varying cross section. Matsumoto and Bogue (98) have provided experimental verification of the melt rheo-optical law in polystyrene under nonisothermal conditions and suggested its high stress level limitations.

When flowing and stressed melts are cooled and vitrified, the birefringence frozen in by vitrification during or following flow has been found to be related to the stress field at vitrification through the rheo-optical law. This idea was discussed by Ballman and Toor (10) and Wales et al. (160) for injection molded polystyrene. This concept was stated as a specific hypothesis and experimentally

verified by Oda, White and Clark (117) for uniaxial extension and shear flow of polystyrene. Various investigators studying polystyrene (57, 96, 116, 159) and high impact polystyrene (118) have shown that the "frozen in" birefringence is determined by the orientation present in the melt.

2.4. DYNAMICS AND HEAT TRANSFER OF FIBER SPINNING

2.4.1. Force Balance

Force balances on a spinline were first reported by Ziabicki (174, 175). Matovich and Pearson (121) developed a more sophisticated approach obtaining the force balance by integrating Cauchy's law of motion across the cross section. The analysis given is based on approximation which the gradient of the thread line diameter is small to make the problem one-dimensional. The forces acting on a spinline include the take-up tension, F_L; gravity, F_g; frictional drag, F_{drag}; surface tension, F_s. If we make balance between position "X_1" and "L" on the x direction, the rheological force and momentum fluxes are (see Figure II-7):

$$F_{rheo} = \frac{\pi}{4} d^2 \sigma_{11}(X_1) = F_L + F_{drag} - F_s - \rho Q(V_L - V_x) \qquad [2\text{-}34]$$

where

$$F_{grav} = \int_{X_1}^{L} \frac{\pi}{4} d^2 \rho g \, dx \qquad f = \frac{C_f \rho_a V_x^2}{2}$$

$$F_{drag} = \int_{X_1}^{L} \pi \alpha \sigma_f \, dx \qquad F_s = \frac{2\nu}{d}$$

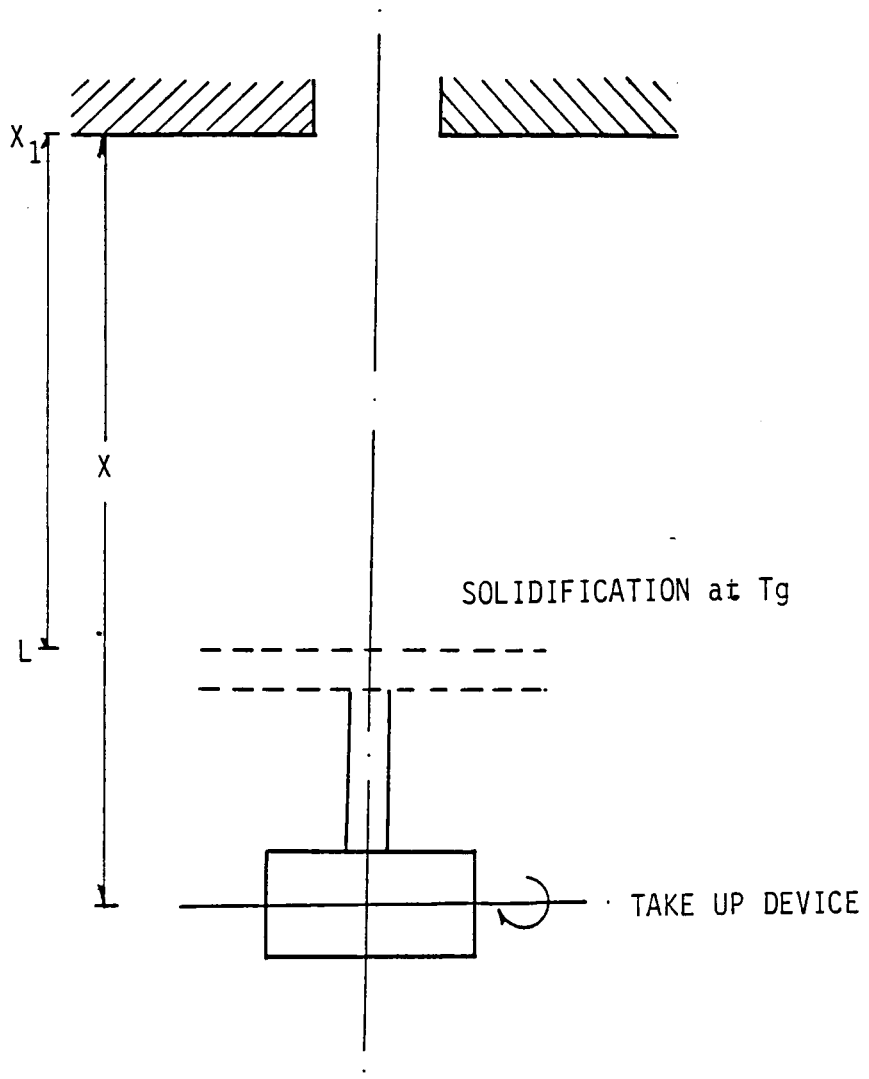


Figure II-7. Scheme of the melt spinning.

ρ_a is the density of air,

C_f is the air drag coefficient,

d is the diameter of the filament,

$\sigma_{11}(x_1)$ is the spinline stress,

V is the velocities at each position,

Q is the extrusion rate.

Some of the forces in Equation [2-34] can be neglected depending on spinning conditions. If no tension is applied to the fiber spinline, we can neglect F_L and consider only F_{grav}. This gravitational spinning was treated by Trouton (154). If tension is applied to the fiber, both F_L and F_{grav} must be considered. When the take-up velocity is increased, F_{grav} can be negligible. Ziabicki and Kedzierska (176) gave an isothermal solution for Newtonian melt.

$$F_{rheo} = F_L \qquad [2\text{-}35a]$$

$$A\sigma_{11} = A\chi \frac{dvi}{dxi} = F_L \qquad [2\text{-}35b]$$

$$V_1(x_1)/V_1(x_0) = \exp(F_L\, x_1/\chi Q) \qquad [2\text{-}35c]$$

$$A(x_1)/A(0) = \exp(-F_L\, x_1/\chi Q) \qquad [2\text{-}35d]$$

where χ is the elongational viscosity. In the case of non-Newtonian fluids, more complex rheological models must be used. Matovich and Pearson (121, 122) obtained a steady state solution for viscous power law fluids.

The earliest study of modelling for viscoelastic fluids is that of Matovich and Pearson (121). There have been more extensive investigations for viscoelastic fluids by Acierno et al. (2), Chen et al. (23), Zeichner (172), Denn, Petrie and Avenas (33), Fisher and Denn (43), White and Ide (163), Matsui and Bogue (97) and others.

2.4.2. Heat Transfer

2.4.2.1. Heat transfer coefficient. Experimental studies of convective heat transfer to moving filaments has been carried out by Muller (107), Sano and Nishikawa (134), Kase and Matsuo (79), Glickman (53), Acierno, Dalton, Rodiguez and White (2) and Shimizu, Troumi and Mitsui (140). Kase and Matsuo measured heat transfer coefficient experimentally by subjecting a heated wire to air flow, both parallel to the wire and at right angles to the wire, recording the cooling of wire, finally converting the cooling curve into Nu-Re relation as

$$Nu = 0.42\ Re^{0.334}(1 + k) \qquad [2\text{-}36]$$

where $(1 + k)$ is the correlative coefficient for perpendicular air flowing the cylinder they give

$$(1 + k) = [1 + (\frac{V_y}{V})^2]^{0.167} \qquad [2\text{-}37]$$

where V_y is the air speed to fiber axis and V is the filament velocity. Glickman also carried out experiments by using laminar and turbulent boundary layers in axial air flow over a stationary cylinder and got

$$Nu = 0.325\ Re^{0.3} \quad . \qquad [2\text{-}38]$$

Theoretical studies of the prediction of heat transfer coefficients in fiber spinning has been given by Vasudevan and Middleman (156) and Acierno et al. (2). They used the laminar boundary layer, and show that the Nusselt number in both these theories resulted as a function of a single variable β where

$$\beta = \beta(Re(D/x)^2, Pr) \qquad [2\text{-}39]$$

where Pr is the Prandtl number.

2.4.2.2. Theoretical modelling of spinline temperature profile. A one-dimensional heat balance on a moving threadline assumes a constant temperature across the fiber cross section leads to the balance (7, 79, 80):

$$Cp\rho\pi R^2\left(\frac{\partial T}{\partial t} + V\frac{\partial T}{\partial x}\right) - 2\pi R[h(T - T^*) + \sigma\varepsilon(T^4 - T^{*4})] = 0 \qquad [2\text{-}40]$$

where

R is the local radius of filament,

h is the coefficient of heat transfer at the filament surface,

T is the local temperature of the filament,

T* is the temperature of ambient air,

t is the time,

σ is the Stefan-Boltzmann constant,

ε is the emissivity,

Cp is the isobaric specific heat.

If the term for radiation heat loss can be neglected and a steady state is presumed, we obtain

$$\frac{dT}{dx} = \frac{2h\sqrt{\pi A}}{Cp \cdot \rho \cdot v \cdot A} (T^* - T \quad . \qquad [2\text{-}41]$$

Andrews (7) introduced the distribution of temperature along the spinline with known cross sectional area function. Kase and Matsuo (79, 80) generalized Andrews' analysis by simultaneously solving the heat balance with a force balance.

Kase and Matsuo (79) were the first to give a combined dynamic and heat transfer analysis of the spinline. They combined one-dimensional Newtonian fluid model for the spinline with applied tension and a one-dimensional heat balance.

$$A\chi(T) \frac{dv_1}{dx_1} = F_L \qquad [2\text{-}42a]$$

$$G C_p \frac{dT}{dx} = -h \pi d(T - T_s) \quad . \qquad [2\text{-}42b]$$

From these equations, they can predict the theoretical values such as temperature distribution along the spinline, tension, and cross sectional area:

$$\frac{dT}{dx} = -1.67 \times 10^4 \frac{(1 + k)(T - T_s)}{G^{2/3} \rho^{1/3} A^{1/6}} \qquad [2\text{-}43]$$

$$F = \frac{h\, G^{0.334}\, Cp^{-1}\, \rho^{-1.334} \int_{A_G}^{A_1} A^{-1.167}\,(1 + k)dA}{\int_{T_G}^{T_1} \frac{1}{\chi(T - T_c)}\, dT} \qquad [2\text{-}44]$$

$$A_N = (1000 \cdot F \cdot Cp \cdot \rho^{1.334}\, G^{-0.334} \int_{T_G}^{T_1} \frac{1}{\chi(T - T_s)(1 + K)} \times dA + A_1^{-0.167})^{-\frac{1}{0.167}} \qquad [2\text{-}45]$$

Hamana, Matsui and Kato (56) include the effect of air drag, gravitation and momentum flux forces. Lamonte and Han (89) considered the non-Newtonian effect on the spinline elongational viscosity in nonisothermal melt spinning. There have been the solutions of non-isothermal melt spinning type problems of viscoelastic fluid model. Fisher and Denn (44) and Matsui and Bogue (97) have reported alternate approaches to this problem.

The spinline temperature during crystallization is controlled by competition between heat generated by crystallization and heat loss as a result of continuous cooling. The effect of crystallization was first considered by Nakamura, Amano and Katayama (110, 111, 112). For the steady state

$$G\, Cp \frac{dT}{dx_1} = C[h(T - T_s) + \varepsilon k(T^4 - T_s^4)] + \rho \Delta H_f \frac{dx}{dt} \qquad [3\text{-}46]$$

where x is the fraction of crystallinity and ΔH_f is the heat of crystallization.

2.4.2.3. Temperature profiles across fiber cross section in spinline. The temperature profile within a melt spun filament is determined by Fourier's law of heat conduction if the velocity field may be neglected. This has the form

$$\rho Cpv\left(\frac{dT}{dx}\right) = \frac{1}{r}\frac{\partial}{\partial r}\left(kr\frac{\partial T}{\partial r}\right) \qquad [2\text{-}47]$$

with boundary and initial conditions

$$T(r, 0) = T_0, \quad \frac{\partial T}{\partial r}(0, t) = 0$$

$$-k\frac{\partial T}{\partial r}(R, T) = h(T(R, t) - T_s)$$

where k is the thermal conductivity. For the special case of constant fiber diameter Carslaw (22) and Andrews (7) computed the temperature profile analytically by using Bessel functions.

$$\frac{T - T_s}{T_0 - T_s} = \sum_n^{\infty} \frac{2 N_{nu} J_0(\beta_n \frac{r}{R})}{(\beta_n^2 + N_{nu}^2) J_0(\beta_n)} \exp(-\beta_n F_{fo}) \qquad [2\text{-}48]$$

where β_n are the roots of

$$\beta_n J_1(\beta_n) = N_{nu} J_0(\beta_n)$$

and

N_{fo} is the Fourier number which has the form $L^2/\alpha t$,

N_{nu} is the Nusselt number which has the form hL/k.

Various researchers have discussed the variations on this simulation of more complex heat conduction problems. Morrison (105) has also described numerical methods to evaluate the temperature profiles as a function of time with constant cross sectional area. He attempted to consider the advancement of the crystallization front across the diameter of the fiber with spinline position.

Shimizu et al. (141, 142) considered the effect of asymmetric cooling from the transverse air flow. The temperature distribution in the filament cross section was obtained by means of the finite-difference method. Kase and Matsuo (81) also numerically computed the temperature profile in melt spinning filament without assuming axisymmetry since in most industrial melt spinning operation cooling air is blown at right angles to the filament. They introduced the equations of continuity and energy in cylindrical coordinates as

$$\frac{1}{r}\frac{1}{\partial r}(r\, v_r) + \frac{dv}{dx} = 0 \qquad [2\text{-}49a]$$

$$\rho Cp\left(V_r \frac{dT}{dr} + v\frac{dT}{dx}\right) = k\left(\frac{1}{r}\frac{\partial}{\partial r}\left(r\frac{\partial T}{\partial r}\right) + \frac{1}{r^2}\frac{\partial^2 T}{\partial t^2}\right) \qquad [2\text{-}49b]$$

where v_r is the velocity in radial direction, v is the velocity in the x direction and t is the air blowing angle. Sugiyama et al. (169) included air drag, gravitational and momentum flux forces and computed radial variations in temperature across the fiber diameter.

2.5. ORIENTATION IN FABRICATED GLASSY POLYMERS

2.5.1. Fibers

It is well known that amorphous vitrifying polymer melts can attain significant levels of orientation through processing. This has been observed for melt-spun fibers, injection molded parts, film and blow molded parts. Our concern here will be with melt spun fibers.

Melt spinning consists of the preparation of spinnable polymer melt, extrusion of the melt through spinneret orifices, extension of the molten polymer leaving the orifice, and winding of solidified filaments of a bobbin.

Birefringence in filaments, indeed thick filaments, was first described in the work of Cleereman, Karam, and Williams (25). They obtained spun filament in a size range from 0.5 to 1.4 mm diameter. These diameters are much thicker than those of industrial fibers.

Oda et al. (117) have described an experimental study of the development of orientation in polystyrene melt spun fiber. They noted that the plot of birefringence versus spinline stress is a single nearly straight line with a slope equivalent to the melt phase stress optical constant. It is

$$\Delta n = C\sigma_{11} = C\left(\frac{F}{\pi R^2}\right) \qquad [2\text{-}50]$$

where C is an apparent stress optical constant and corresponds to a value of -4500 Brewster. They also showed that the relationship

between Hermans orientation factor and stress which has the form

$$\Delta n = f \Delta^0 = C\sigma_{11} \qquad [2\text{-}51a]$$

$$f = (C/\Delta^0) \cdot \sigma_{11} \ . \qquad [2\text{-}51b]$$

Hamana et al. (55, 56) and Dumbleton (41) have measured spinline orientation in polyethylene terephthalate fibers. They found a linear relationship between spinline stress and birefringence. Stress optical constant was evaluated as 7000-8000 Brewster.

Recently Sugiyama et al. (169) have investigated the orientation distribution of polyethylene terephthalate fibers across a filament using the steady state single filament melt spinning theory. They found that orientation of fiber depends mostly on the take-up speed and the orientation distribution becomes much more pronounced with increase of spinning speed.

2.5.2. Other Fabricated Operations

The birefringence in tubular film of vitrifying plastics was first discussed by White and Dietz (165). They concluded that birefringence in tubular film will be related to the stress of vitrification. Choi et al. (26) experimentally found this valid in polystyrene tubular film.

Orientation in injection molded parts of amorphous plastics has been studied since the work of Spencer and Gilmore (147). Ballman, Toor and Jackson (10, 11), Wales et al. (158, 159), Fleissner (45) and Dietz and White (38) have also investigated injection molded

polystyrene parts and determine the birefringence distribution across the thickness. Oda et al. (117) have shown that the "frozen in" birefringence is determined by the difference in principal stresses at vitrification. Dietz, White and Clark (38, 39, 165), Janeshitz and Kriegl (74) and Isayev (67, 68) have attempted theoretically to predict birefringence in injection molded parts.

White and Agarwal (166) modelled the development of orientation in blow molded polystyrene bottles. They compared their prediction with experimental measurements of birefringence distribution.

2.6. ORIENTATION AND MORPHOLOGY IN CRYSTALLIZED POLYMERS

The orientation and morphology of crystalline polymers differ from those of amorphous polymer because the morphology in crystalline polymers is related to the deformation history and the crystallization process.

2.6.1. Melt Spinning Fibers

The problem of structure development during melt spinning is the interaction of rheological factors, heat transfer from the running threadline and the crystallization kinetics of polymer. This was realized by Ziabicki (173). Katayama, Amano and Nakamura (83) have reported first important experimental studies. Kitao et al. (85), Abbott and White (1) and later investigators interpreted crystalline orientation development in terms of Hermans-Stein orientation factor. Katayama et al. (83), Dee and Spruiell (32),

Spruiell and White (164), Nadella et al. (109) and Ishizuka and Koyama (69) have followed crystallization in polyolefin fiber spinline using wide angle x-ray scattering.

Katayama et al. (83) made x-ray patterns and measured temperature, birefringence and diameter profiles on running spinlines of polyethylene and polypropylene. They have shown that crystallization kinetics may be greatly enhanced due to the molecular orientation caused by stretching and cooling of melt.

The variation of orientation functions with take-up velocity has been described by Abbott and White (1) and Dees and Spruiell (32). The latter authors measured spinline stress and found that orientation factors are a unique function of spinline stress.

Katayama et al. (83), Kitao et al. (85), Spruiell and White (164) and Nadella et al. (109) and Izhizuku and Koyama (69) have investigated polypropylene fibers. They considered the influence of applied stresses on the rate of crystallization and on the development of crystalline morphology. Nadella et al. reported that higher take-up velocity, low extrusion rate, low spinning temperature and higher molecular weight gives higher orientation. They found that crystalline orientation is a unique function of spinline stress independent of polymer molecular weight and probably molecular weight distribution. Katayama et al. (83), Nadella et al. (109) and Shimizu and Shimazaki (141, 142) measured the birefringence along a molten filament. They found the birefringence increases abruptly at crystallization. Based on such results, a simulation for polypropylene melt spinning was carried out by Shimizu and Shimazaki

(142) to predict the birefringence of the spun fiber. They also calculated the temperature distribution in cross section of filament by solving the thermal conduction equation and then estimated the birefringence distribution.

2.6.2. Other Fabrication Operations

Maddams and Preedy (95) and Choi et al. (27) presented an experimental study of orientation in HDPE blown film. Choi et al. found that the crystalline orientation and birefringence could be correlated with the stress field at solidification. Shimomura et al. (143) made a similar study of the development of the structure of polypropylene tubular film.

Injection molded crystalline parts have been investigated by optical microscopy (14, 60, 61) and by wide angle x-ray diffraction. Clark and Garber (24) and Heckmann and Johnson (61) have found a spherulitic core and outer layers which possess more oriented superstructures.

2.7. RESIDUAL STRESSES (THERMAL QUENCH STRESSES)

Products of amorphous polymers are usually made by shaping of material in the molten state and then fixing the final shape by cooling to below the glass transition temperature. Thus cooling gives rise to quench stresses.

The residual stresses arise in the following manner. In the initial cooling, the surface cools much more rapidly than the center regions. The material solidifies at a much larger perimeter than

would be expected of thermal equilibrium. The core solidifies at a late time. This produces tensile stresses in the core and compressive stress in the outer layer.

2.7.1. Theory of Transient Thermal Stresses

Clerk Maxwell (99) reported one of the first mathematical analyses of thermal stress development during cooling. These efforts were extended by Lord Rayleigh (127). They use linear elasticity which can be expressed

$$\underset{\sim}{\sigma} = \lambda(\mathrm{tr}\ \underset{\sim}{\nu})\underset{\sim}{I} + 2G\ \underset{\sim}{\nu} \qquad [2\text{-}52]$$

where

$$= \frac{r\ E}{(1 - \nu)(1 - 2\nu)}$$

$$G = \frac{E}{2(1 + \nu)}$$

ν is the Poisson's ratio,

E is the modulus of elasticity.

He predicted transient stress in both thin plate and cylinder.

Dinnik (37) and Lees (91) have calculated the thermal transient stress from temperature profile in a cylinder. This work was extended by Jaeger (72) who gave more extensive numerical results. The transient thermal stress can be shown to be

$$\sigma_{rr} = \frac{2\alpha E\theta_0}{1 - \nu} \sum_{n=1}^{\infty} \frac{e^{-P_n t}}{\beta_n^{\,2}}\left(1 - \frac{b}{r}\,\frac{J_1(\beta_n \frac{r}{b})\ J_1(\beta_n)}{J_0^{\,2}(\beta_n) + J_1^{\,2}(\beta_n)}\right) \qquad [2\text{-}53a]$$

$$\sigma_{\theta\theta} = \frac{2\alpha E\theta_0}{1-\nu} \sum_{n=1}^{\infty} \frac{e^{-P_n t}}{\beta_n^2} \left(1 - \frac{b}{r} \frac{J_1(\beta_n \frac{r}{b}) + J_1(\beta_n)}{J_0^2(\beta_n) + J_1^2(\beta_n)} - \frac{J_0(\beta_n \frac{r}{b})\, J_1(\beta_n)}{J_0^2(\beta_n) + J_1^2(\beta_n)}\right) \quad [2\text{-}53b]$$

$$\sigma_{zz} = \frac{2\alpha E\theta_0}{1-\nu} \sum_{n=1}^{\infty} \frac{e^{-P_n t}}{\beta_n^2} \left(2 - \frac{J_0(\beta_n \frac{r}{b})\, J_1(\beta_n)}{J_0^2(\beta_n) + J_1^2(\beta_n)}\right) \quad [2\text{-}53c]$$

where $\beta_n = N_{nu}\, J_0(\beta_n)/J_1(\beta_n)$.

Muki and Sternberg (106) introduced the quasi-static analysis of transient thermal stresses in the linear theory of viscoelastic solid with temperature dependent properties. By using a time and temperature dependent relaxation modulus they generated the thermal stresses in a slab. They were also concerned with the stresses produced in a sphere by an arbitrary time-dependent radially symmetric temperature distribution. The transient thermal stresses in a viscoelastic slab derived

$$\sigma(x_1, t) = -3\alpha_0 \int_0^t R[\xi(x_1, t) - \xi(x_1, t')] \frac{\partial}{\partial t} \theta(x_1, t')dt' \quad [2\text{-}54]$$

where θ is a reduced temperature which has the form

$$\theta(x_1, t) = \frac{1}{\alpha_0} \int_{T_0}^{T} \alpha(T')dT'$$

ξ is the reduced time given by

$$\xi(x_1, t) = \int_0^t a_T[T(x_1, t')]dt'$$

α is the volume coefficient of thermal expansion

α_0 is its value at temperature T_0,

R is an auxiliary function.

2.7.2. Theory of Thermal Quenched Stresses

The first attempt to calculate the tempering stresses in glass plate was made by Adams and Williamson (4). Bartenev (12) considered that above the T_g, the glass behaves as a liquid with internal stresses being absent but below T_g it behaves like a perfect elastic solid. Bartenev's theory can be stated as

$$\sigma(x_1) = \frac{\beta E}{1 - \nu} (\overline{\Phi} - \phi(x_1)) \qquad [2\text{-}55]$$

where

$$\overline{\Phi} = \frac{1}{b} \int_0^b \phi(x_1', t/T_{x1} - T_y) dx_1',$$

β is the linear coefficient of thermal expansion,

b is the half thickness of the slab,

ϕ is a specific temperature defined by

$$\frac{d\theta(x_1, t)}{dx_1} = \frac{dT(x_1, t/T_{x1} = T_g)}{dx_1}$$

where $T(x_1, t/T_{x1} = T_g)$ is the temperature distribution at the time the point x_1 passes through T_g. Bartenev predicted a parabolic law of residual stress distribution in tempered glass.

Indendom (70, 71) suggested a similar theory. He considered the compatibility of the strains which Bartenev ignored.

O'Rourke and Saenz (120) developed a simple theory of residual stress using Bartenev's proposal. They argue that when material cools

down from T_1 to T_0 if T_1 is less than T_g (softening temperature), the stresses are transient but if T_1 is much larger than T_g, the stresses remain permanently. Therefore, if one calculates the solidification time (t*), residual stresses can be estimated by taking negative value of transient stresses at $t = t^*$.

$$\sigma_{rr}{}^{R} = -\sigma_{rr}{}^{t} \quad , \quad \sigma_{\theta\theta}{}^{R} = -\sigma_{\theta\theta}{}^{t} \qquad [2\text{-}56]$$

where $\sigma_{rr}{}^{R}$ is the residual stresses and $\sigma_{rr}{}^{t}$ is the transient stresses. Bartenev's model has been expanded or better reformulated by Aggarwala and Saibel (5) who use a Maxwell model applying the calculation of residual stresses. They assumed that the viscosity is zero in the molten state and infinity in the solid states, i.e.,

$$\begin{aligned} \eta &= 0 \qquad & 0 < x_1 < \bar{x}_1 \qquad & \qquad 0 < t < \bar{t} \\ \eta &= \infty \qquad & \bar{x}_1 < x_1 < b \qquad & \qquad \bar{t} < t < \infty \end{aligned} \qquad [2\text{-}57]$$

where $\bar{x}_1$ is the freeze point for a given time and $\bar{t}$ is the freeze time for a given point. Their formulation is limited to slabs. Theory can be shown as

$$\sigma(x_1, t) = \frac{1}{3} \int_0^t 2G\left[\frac{1}{h - x_1} \int_{x_1}^{h} \frac{\varepsilon(x_1', t')}{\partial t'} dx_1' - \frac{d\varepsilon(\alpha_1, t')}{dt'}\right] dt' \exp\left(-\int_0^t \frac{G}{\eta} dt\right) \qquad [2\text{-}58]$$

where

$$\varepsilon = \int_{T_0}^{T} \alpha \, dT,$$

α is the volume coefficient of thermal expansion,

$\bar{x}_1$ is the freeze point for a given time.

So they can predict the residual stresses as a function of both time and space.

Lee, Rogers and Woo (92, 93) generalize the theory of Aggarwala and Saibel by introducing the effect of nonisothermal linear viscoelasticity and the temperature dependence of physical properties. Their theory was developed from Muki and Sternberg (98) for the condition of free lateral expansion during the quenching of a slab. In recent years Woo et al. (168) expanded these theories to compute the residual stress in a viscoelastic cylinder.

2.7.3. Residual Stresses Effect on Polymer Properties

The residual stresses from rapid cooling is generally harmful to properties of materials. Tensile surface residual stresses result in fracture while compressive stresses counteract it. In some cases a product fails without additional stressing because of high residual stresses. An extensive literature exists for glass and metals.

It seems that Spencer and Gilmore (147) first investigated residual strain effect on injection molded parts. They discussed the three types of residual strains due to quenching, frozen-in molecular orientation and configurational volume. They found these residual strain results in cracking in injection molded parts.

Thermal quenching experiments were performed to produce residual stress in polycarbonate, ABS, PVC, polysulfon and PMMA plate by Broutman and Krishnakumar (20). They found that these residual stresses have a great effect on impact strength.

Broutman and Soul (19) investigated the effect of residual stresses on the impact and deformation behavior of bisphenol-A polycarbonate and PMMA. It was shown that the notched Izod impact strengths are increased by these residual stresses and compressive residual stresses can cause plastic yielding.

Siegmann, Narkis and Rosenzweig (144) found that the softening behavior of glassy polymers is affected by the state by residual stresses.

Thakkar and Broutman (153) have studied the effect of cold rolling on impact strength PVC, ABS, PC. They have proposed that the influence of residual stresses on impact strength will be great only for polymer whose deformation or failure initiation event is highly localized such as polycarbonate.

Residual stresses in injection molded bars of polypropylene have been examined by Coxon and White (31). They have found that stress level was reduced by aging at room temperature.

Siegmann, Buchman and Kenig (145) have investigated the density and tensile properties in quenched modified polyphenylene oxide. They have determined the tensile modulus increases significantly from the surface to inner layers due to the residual stresses.

CHAPTER III

EXPERIMENTAL

3.1. MATERIAL

Polystyrene, polycarbonate, and polypropylene have been selected in this study. Polystyrene and polycarbonate are amorphous polymers. These polymers have been studied in similar experiments by earlier investigators (116, 117, 119, 94, 95, 109). Their nature and properties are well established. For polystyrene we chose Dow STYRON 678D and for polycarbonate a General Electric Lexan 141 was used. Polypropylene selected was Hercules Profax 6523.

3.2. FIBER PROCESSING

Melt spun fibers were prepared using an Instron capillary rheometer. The barrel of the rheometer was filled with polymers and the polymers were then extruded at different cross head speeds. They were taken up on 8.1 cm diameter roll using a speed controlled B-B motor. The take-up speeds varied from 22.8 meters/min to 5.5 meters/min. The polymer melt temperature was controlled in the capillary rheometer to allow an error range 1°C. Table III-1 shows the processing conditions which were used in this study including melt temperature, extrusion rate, take-up velocity and die diameter. The initial velocity can be calculated using Equation [3-1].

Table III-1. Processing conditions which were used in this study.

	Unit	PS	PC	PP
Die Diameter		0.127	0.127	0.127
		0.254	0.254	0.254
Extrusion Rate	cm^3/sec	1.53×10^{-3}	1.53×10^{-3}	1.53×10^{-3}
		2.92×10^{-3}	2.92×10^{-3}	2.92×10^{-3}
		4.57×10^{-3}	4.57×10^{-3}	4.57×10^{-3}
		1.5×10^{-2}	1.5×10^{-2}	1.5×10^{-2}
		3.0×10^{-2}	3.0×10^{-2}	3.0×10^{-2}
Take-Up Velocity	m/min	5.5 - 22.8	5.5 - 22.8	5.5 - 22.8
Drawdown Ratio	-	25 - 316	25 - 316	25 - 316
Melt Temperature	°C	160	210	180
		180	220	200
		200	240	
			260	

$$V_0 = V_c \times (D_c/D_0)^2 \qquad [3\text{-}1]$$

where V_c is the cross head speed of the capillary rheometer, D_c is the barrel diameter, and D_0 is the die diameter. The extrusion rates were calculated using

$$Q = V_0 \times A_0 \qquad [3\text{-}2]$$

where A_0 is the die cross sectional area.

Melt spinning was carried out with three different cooling systems. These included air cooling and use of a cooling bath with two teflon rod rollers. This cooling bath was located 5 cm below the die to produce sudden changes in temperature. Ice water and isopropanol with dry ice were used as a cooling medium. The temperature of the quenching medium was kept the same temperature during the experiments: 20-25°C for air, 0°C for ice water, -45°C for isopropanol with dry ice. Table III-2 shows some of the physical constants for each cooling medium. These values were applied to predict heat transfer coefficients which were used in a computer simulation of the melt spinning dynamics.

Figure III-1 shows the melt spinning scheme with different cooling conditions. As shown in this figure, the tension was measured below the die and after the cooling bath by using a Rothshild Electronic Tensiometer with a micro-recorder from Texas Instruments. The readings obtained are not the real tension which is applied at the fiber spinline. This is because of the effect of

Table III-2. Physical constants for cooling media.

	Unit	Air	Water	Isopropanol
Thermal Conductivity	cal/sec cm °K	5.6×10^{-5}	1.63×10^{-3}	3.8×10^{-3}
Heat Capacity	cal/g °C	0.25	0.44	0.4
Viscosity	Poise	1.8×10^{-4}	1.79×10^{-2}	2×10^{-1}
Density	g/cm^3	1.2×10^{-3}	1.0	0.899

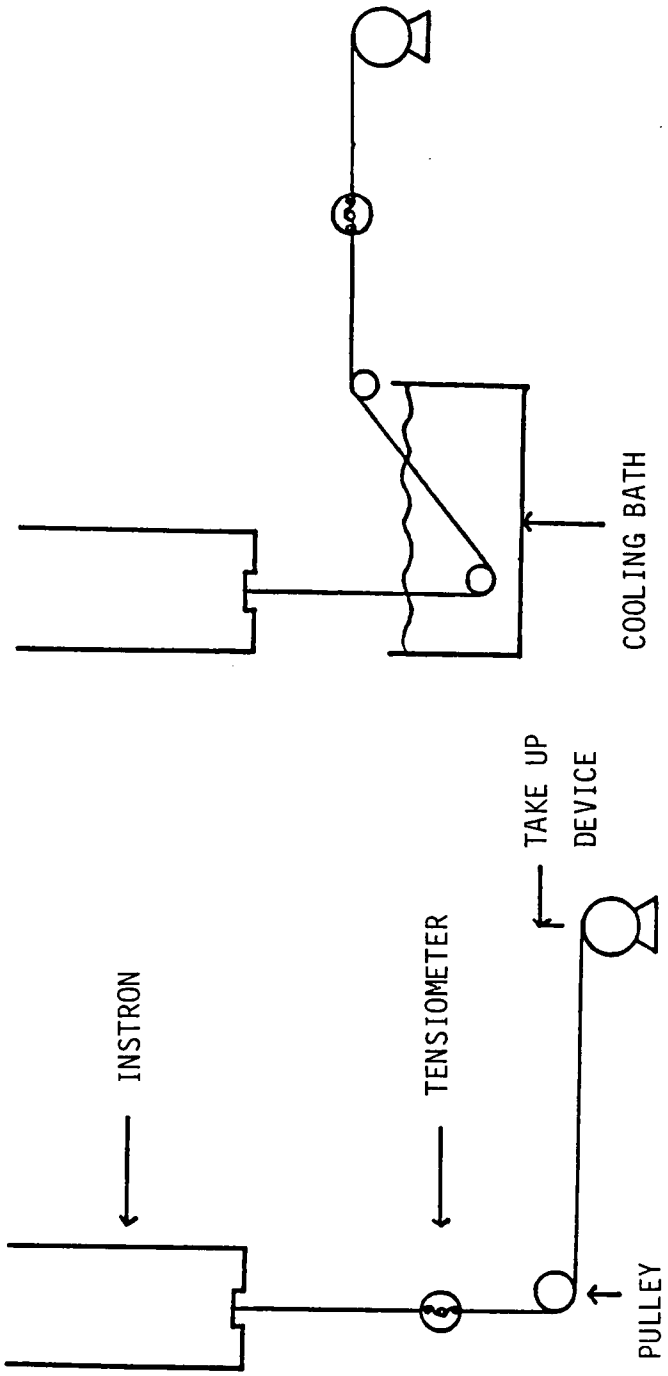


Figure III-1. Melt spinning scheme with different quench conditions.

friction between the thread and the two teflon rods in the cooling bath and the bending moment of the tensiometer (Figure III-2). There seemed to be a special problem of errors for thick polystyrene filaments. Minoshima (103) presented a theoretical calibration procedure. However, we have had to develop a new experimental calibration procedure different from Minoshima's because of the large bending moment of the thick fibers. The calibration was carried out by the following procedure.

a. The arrangement shown in Figure III-3 was designed. It uses an extra pulley (beyond that of Minoshima) which has has a special bearing to minimize the friction.

b. Hang a weight and move the filament with the same velocity used in a spinning experiment.

c. Repeat procedure b at least three times changing the weight near the actual experimental tension values.

d. The real tension can be calculated from the calibration values with the known actual weight using least-square curve fitting.

In order to check the calibration method, we plot in Figure III-4 birefringence versus calibrated stress for both air cooling with cooling bath and without cooling bath. Reasonable agreement is found.

3.3. PREPARATION OF CRYSTALLIZED POLYCARBONATE SAMPLES

Polycarbonate films were prepared with a Wabash compression molding machine. In order to crystallize polycarbonate film, two

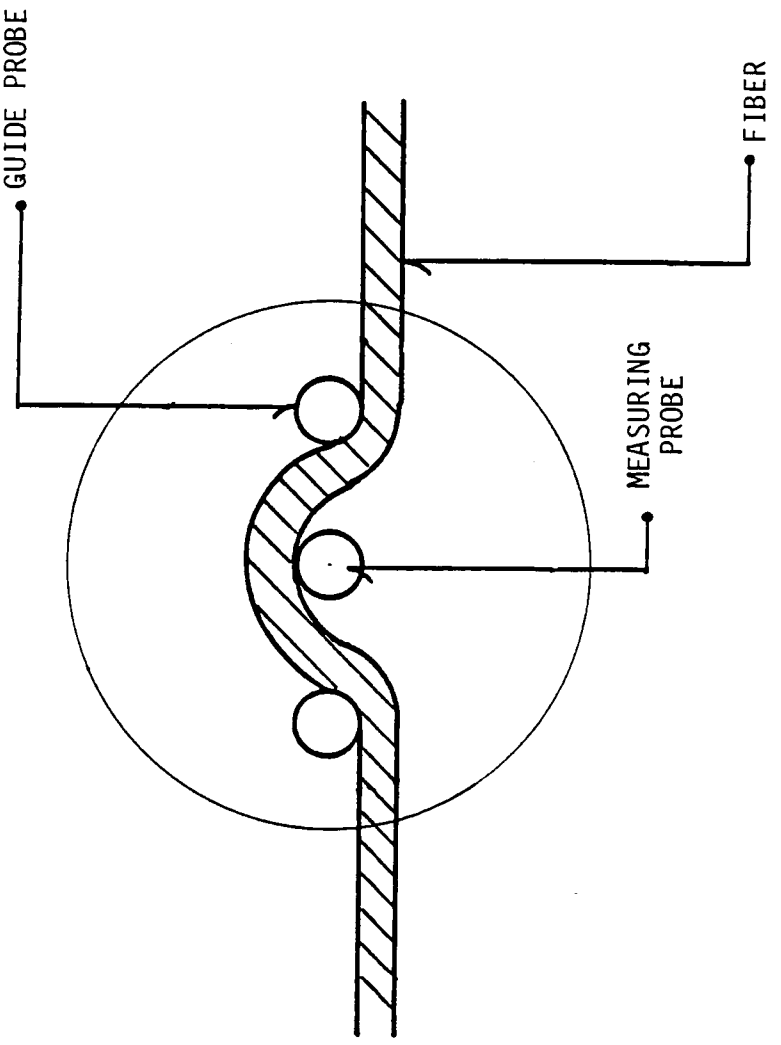
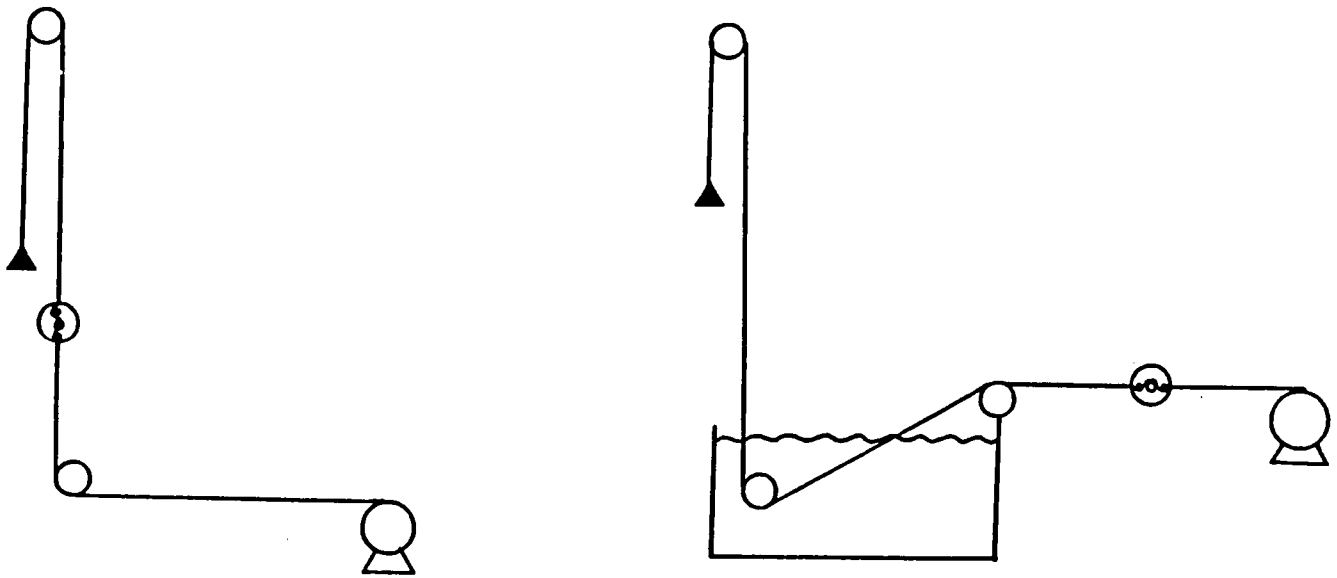


Figure III-2. Bending moment at the tensiometer.



a) AIR COOLING

b) ICE WATER COOLING

Figure III-3. Equipment setup for fiber calibration.

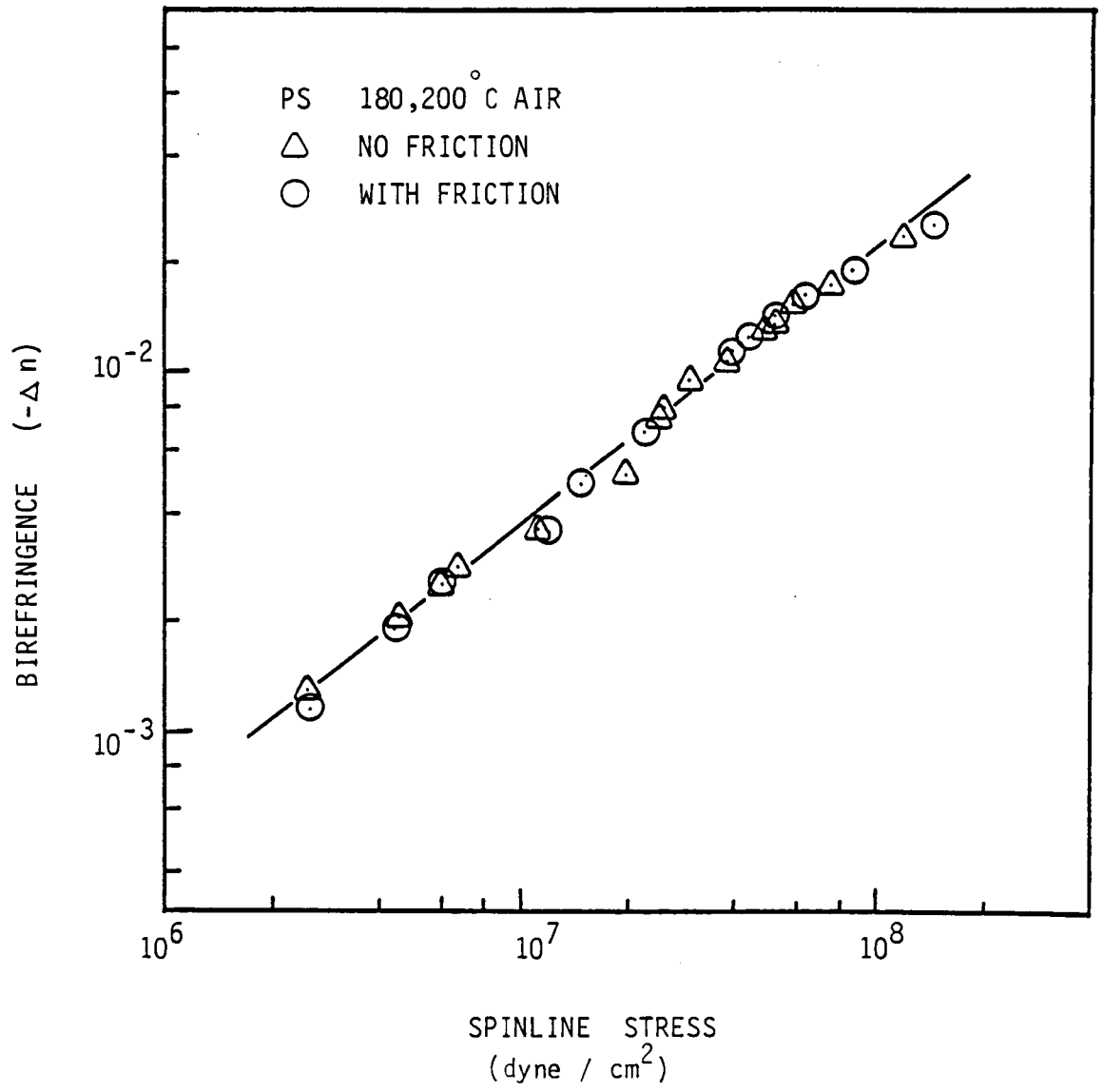


Figure III-4. Relationship between calibrated stress and birefringence at air cooling with water bath and without water bath.

different methods were used. Polycarbonate film (1 x 1 x 0.1 cm) was immersed for three days in acetone 25°C. It was then removed and vacuum-dried at 60°C for seven days to remove most of the imbibed acetone.

Another procedure was carried out with amorphous polycarbonate films to get thermally crystallized polycarbonate films. Samples were placed in a vacuum oven at 175°C for 1 to 5 days to be crystallized with the different crystallinity.

3.4. MEAN BIREFRINGENCE MEASUREMENT

A Leitz microscope equipped with mutually perpendicular polarizer and analyzer were used with a Berek type compensator. The fiber samples were placed on a glass slide with silicone oil to get good contrast. Figure III-5 shows the sample position on a microscope stage and the direction of compensation which is the same as the direction of the compensator. The samples were always placed in a subtraction position. Thus polystyrene fiber could be distinguished from polycarbonate and polypropylene because it has a negative birefringence. Reading values were taken from the compensator after rotation until a dark band which is the zero order band appears. To get accurate values, we repeated this procedure at least three times. The retardation was calculated from these rotation angles using a Leitz calibration chart. Finally, the birefringence was calculated from the measured retardation and diameter as follows:

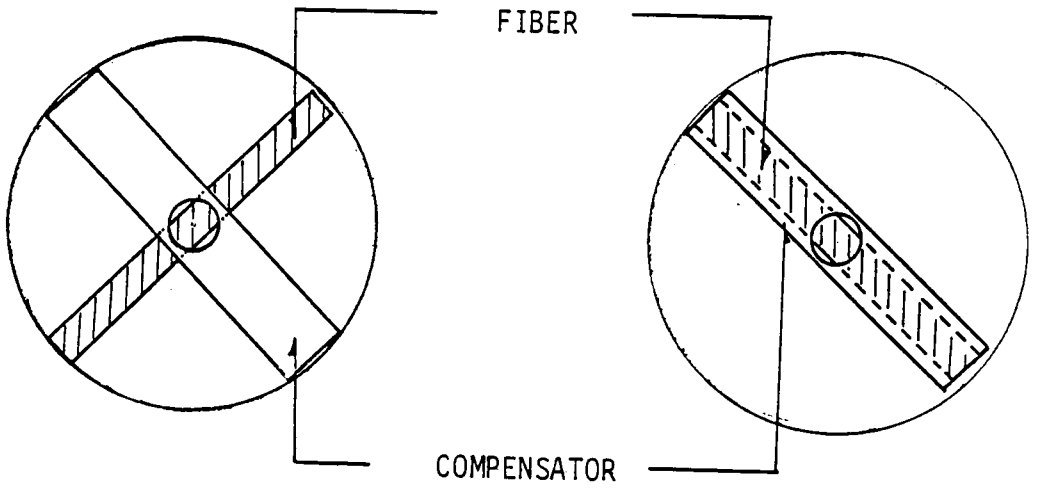


Figure III-5. Sample positions on a microscopy stage for PS, PC and PP.

$$\Delta n = \frac{\Gamma}{d} \qquad [3\text{-}3]$$

where d is the fiber diameter and Γ is the measured retardation.

3.5. BIREFRINGENCE DISTRIBUTION MEASUREMENT

The wedge method (50) mentioned in Chapter II was used in this study. In order to cut a fiber with a desired angle as shown in Figure III-6 fibers were embedded with epoxy in a mold (Figure III-7) shaped like a 1/8" x 3/8" x 3/4" rectangular slab. It was then cured in a vacuum oven for 24 hours at 50°C. The fiber-containing epoxy slabs were cut by a diamond saw from Buehler Ltd. at very low speed to obtain a good surface.

Both crossed polarizer and parallel polarizer-analyzer systems were used to obtain the fringe patterns which are shown in Figure III-8. Using crossed polarizers, dark bands were seen where the retardation is equal to integral number of wavelength. When polarizers are parallel, dark bands were observed on the filament where the retardation is halfway between integral number of wavelengths. The cutting angle was obtained from

$$\theta = \tan^{-1} \frac{D}{x} \qquad [3\text{-}4]$$

where D is the fiber diameter and x is the projection of the oval principal diameter specified in Figure III-6.

We measured the distance between each fringe along the projected oval diameter which has a different retardation

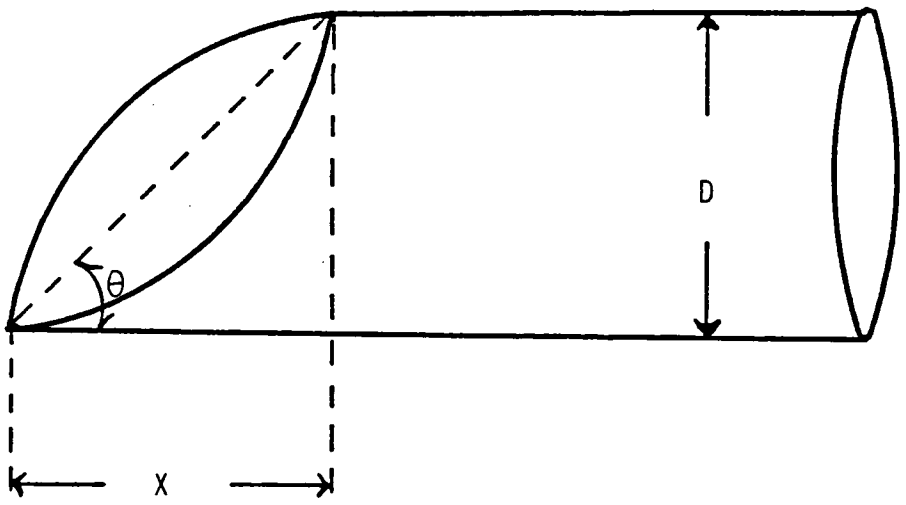


Figure III-6. Cut fiber with a desired angle to measure a birefringence distribution.

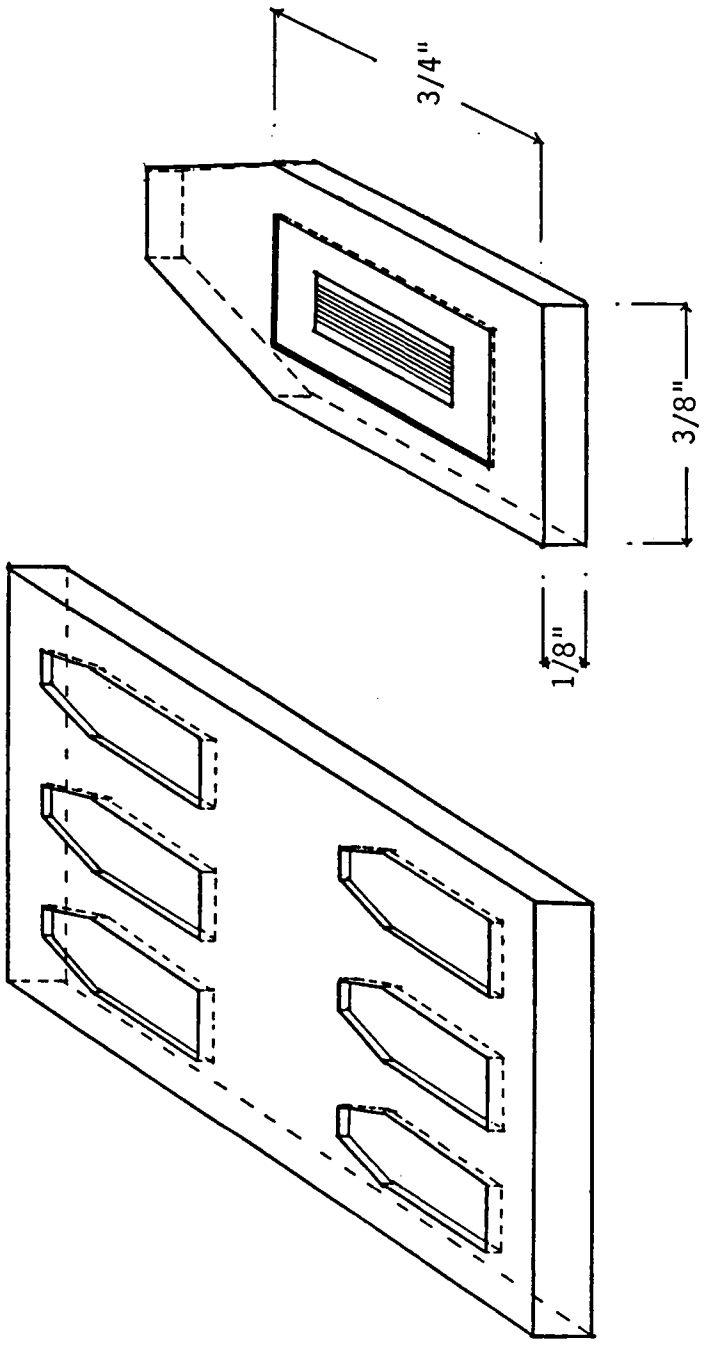


Figure III-7. Mold and fiber containing epoxy slab.

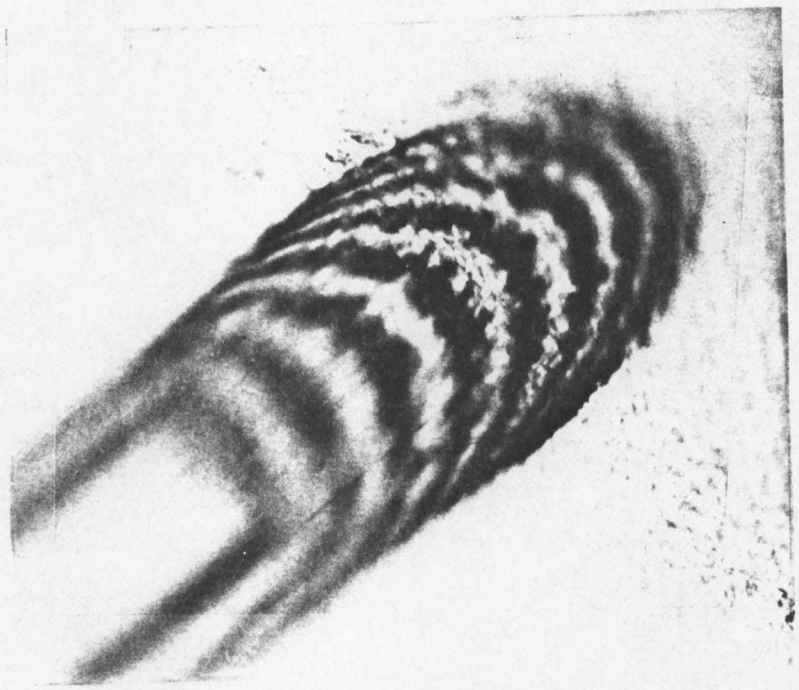


Figure III-8. Typical fringe pattern on the wedge.

(see Figure III-9). The retardation distribution can be plotted as in Figure III-10. The birefringence distribution is predicted from

$$\Delta n_i = \frac{\sum_{i=1}^{n} \Gamma_i}{\sum_{i=1}^{n} D_i} . \qquad [3\text{-}5]$$

3.6. EXPERIMENTS FOR STRUCTURAL CHANGES IN FIBERS

3.6.1. Measurements of Crystallinity

Calorimetry experiments were performed using Dupont 9900 Differential Scanning Calorimeter unit.

The fibers were chopped as small as possible to give good heat conduction in the DSC pan. The chopped fibers were put in the DSC pan and packed well. Because the fiber samples usually have very low crystallinity, the amount of samples prepared were more than 20 mg. These samples were heated at 20°C per minute. This same procedure was also performed with the crystallized polycarbonate films as well as the chopped fibers. The amount of samples prepared were about 10 mg. The crystallinity can be calculated as follows:

$$x = \frac{\Delta H}{\Delta H_f} \qquad [3\text{-}6]$$

where ΔH is the heat of fusion in the sample, and ΔH_f is the heat of fusion in perfect polycarbonate crystal. We used 52.3 J/g (29) for ΔH_f.

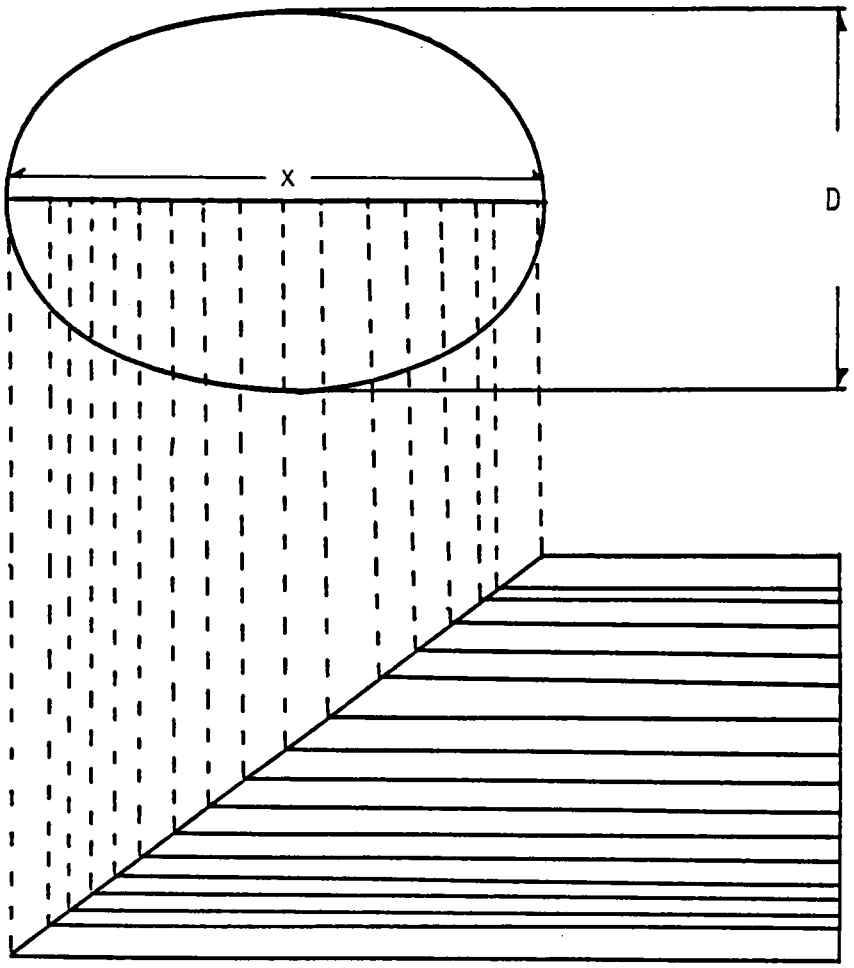


Figure III-9. Calculation of retardation from fringe patterns.

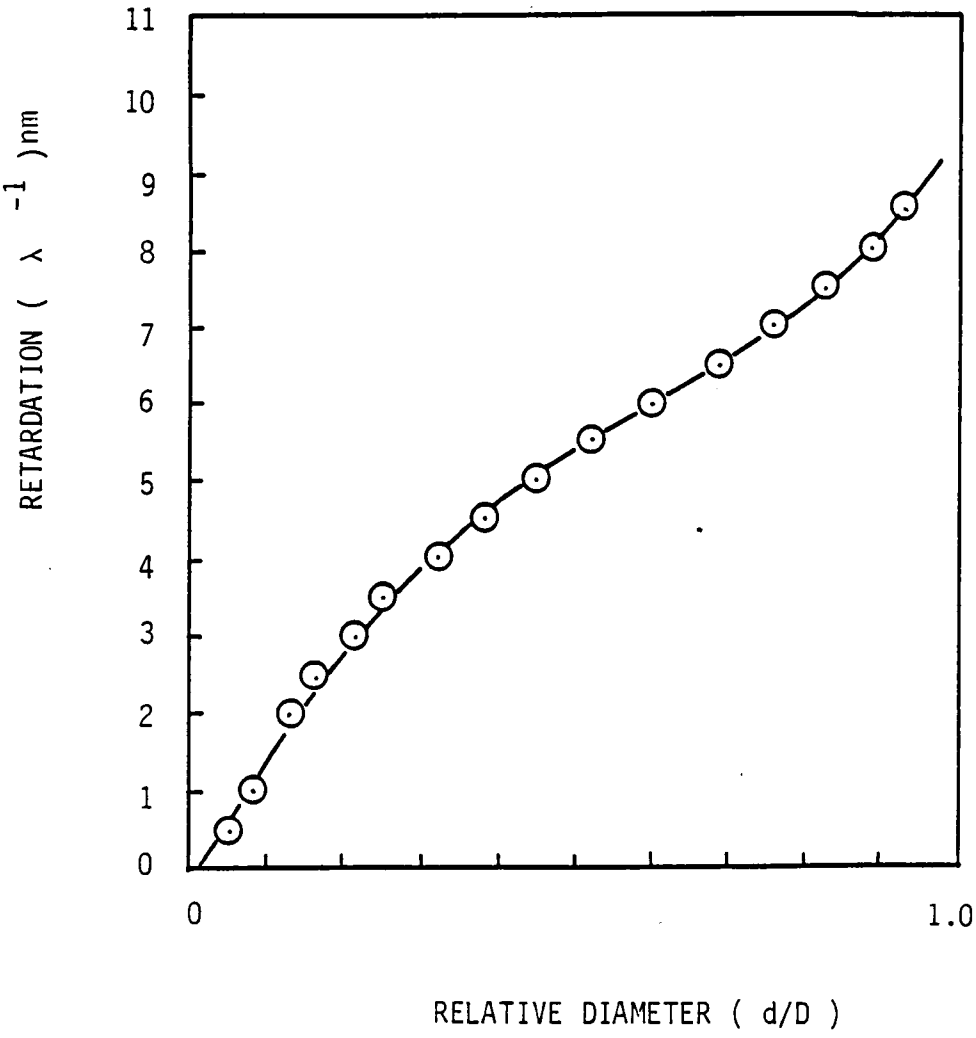


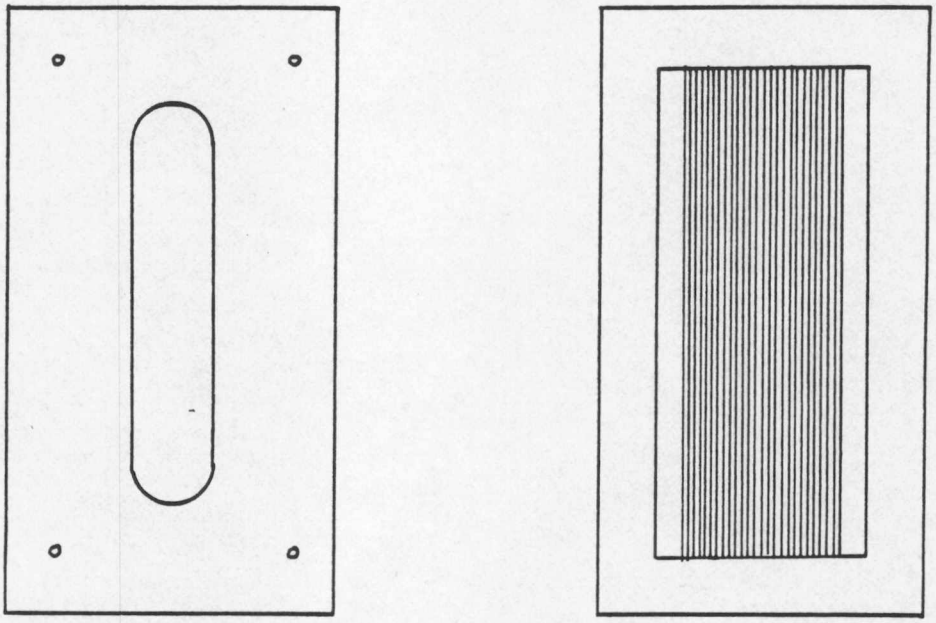
Figure III-10. Typical retardation distribution along the diameter direction.

3.6.2. Fibrillation Experiments

Fibrillar structures were investigated for various fibers. The fibers were peeled with a razor blade. These were studied using scanning electron microscopy and small angle x-ray scattering.

3.6.2.1. SEM experiments. The SEM studies were carried out using a JEOL Model JSM-U3 high resolution scanning electron microscope. The internal structure of fibers can be viewed by studying razor blade peeled fibers. After peeling, the fibers were mounted at sample holder and then a gold-palladium alloy coating was used on the fibers to eliminate charging in the electron beam.

3.6.2.2. SAXS experiments. To see a smaller scale structure level range of tens to hundreds of angstroms, small angle x-ray technique was introduced. The thickness of the sample was about 1 mm-1.1 mm. Figure III-11 shows the sample holder and samples which were mounted on the sample holder. A Rigaku x-ray machine made available by the Goodyear Tire and Rubber Company with a one-dimensional detector was used. The scanning angle was from 0.3° to 1.48° and 45 min was needed to scan each sample.



(a) (b)

Figure III-11. Sample preparation for SAXS. (a) Sample holder; (b) mounted sample.

CHAPTER IV

STRUCTURE DEVELOPMENT IN SPUN FILAMENTS

4.1. MEAN BIREFRINGENCE

4.1.1. Results

Mean birefringence of thin fibers drawn under different processing and cooling conditions were measured. These fibers have diameters from 24 μm to 71 μm. Figures IV-1, IV-2, and IV-3 summarize experimental results for Δn and drawdown ratio V_L/V_0. The birefringence of polystyrene fibers is negative and its magnitude increased with drawdown ratio. Positive birefringences were obtained for polycarbonate and polypropylene fibers. A linear relation between Δn and V_L/V_0 was observed in polycarbonate and polystyrene when logarithmic coordinates were used. The small variation of birefringence with V_L/V_0 was found in polypropylene fibers while large variation in polystyrene and polycarbonate fibers.

Several processing temperatures were used. Generally each polymer exhibits a distinctly different behavior dependent upon temperature. The temperature dependency on Δn in polypropylene is less sensitive than that of the others.

The influence of quenching conditions on the dependence of Δn on V_L/V_0 are shown in Figures IV-4 and IV-5.

Little difference in the functionality was found for the various cooling conditions.

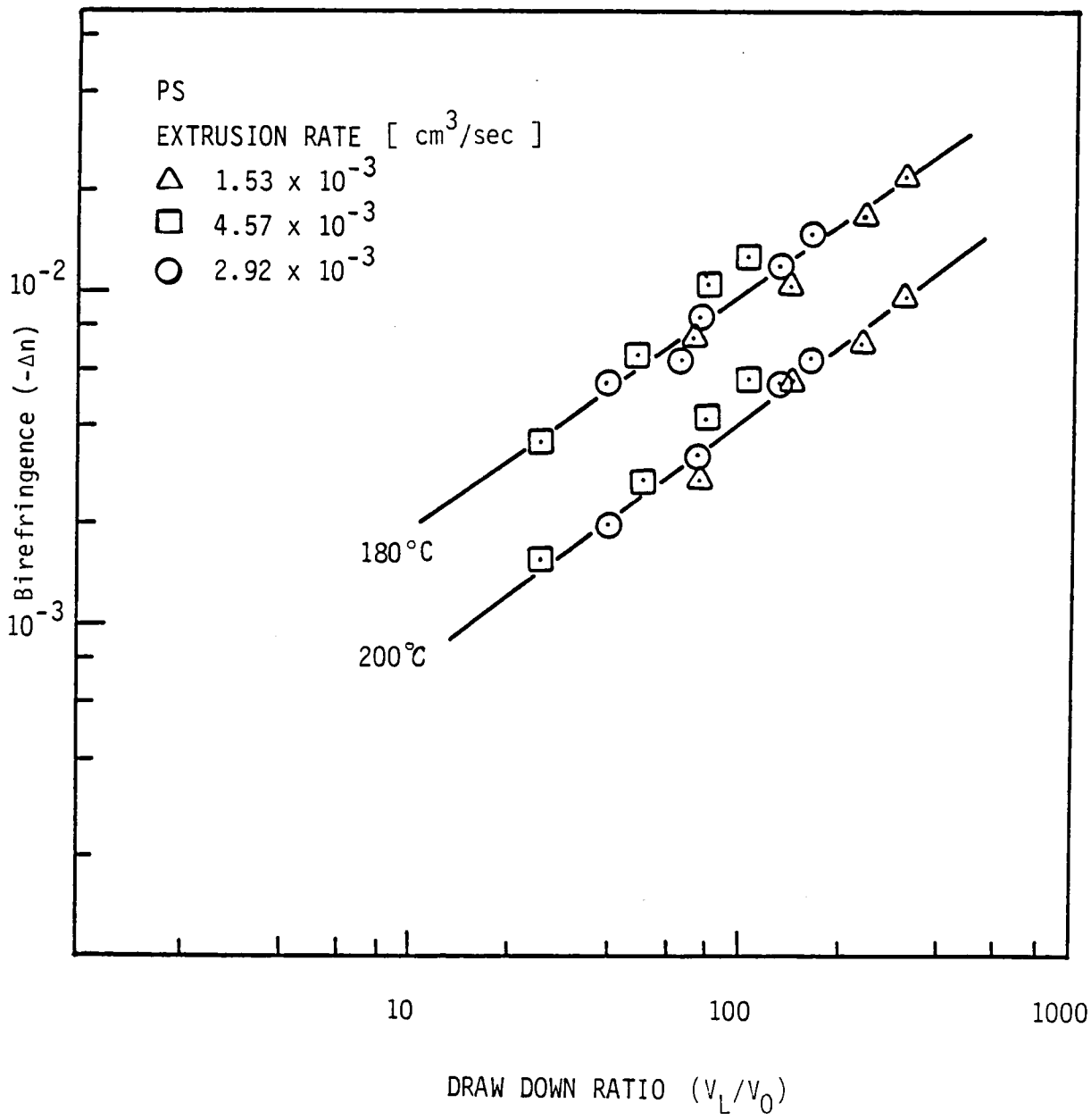


Figure IV-1. Birefringence versus drawdown ratio at different processing conditions for polystyrene fibers.

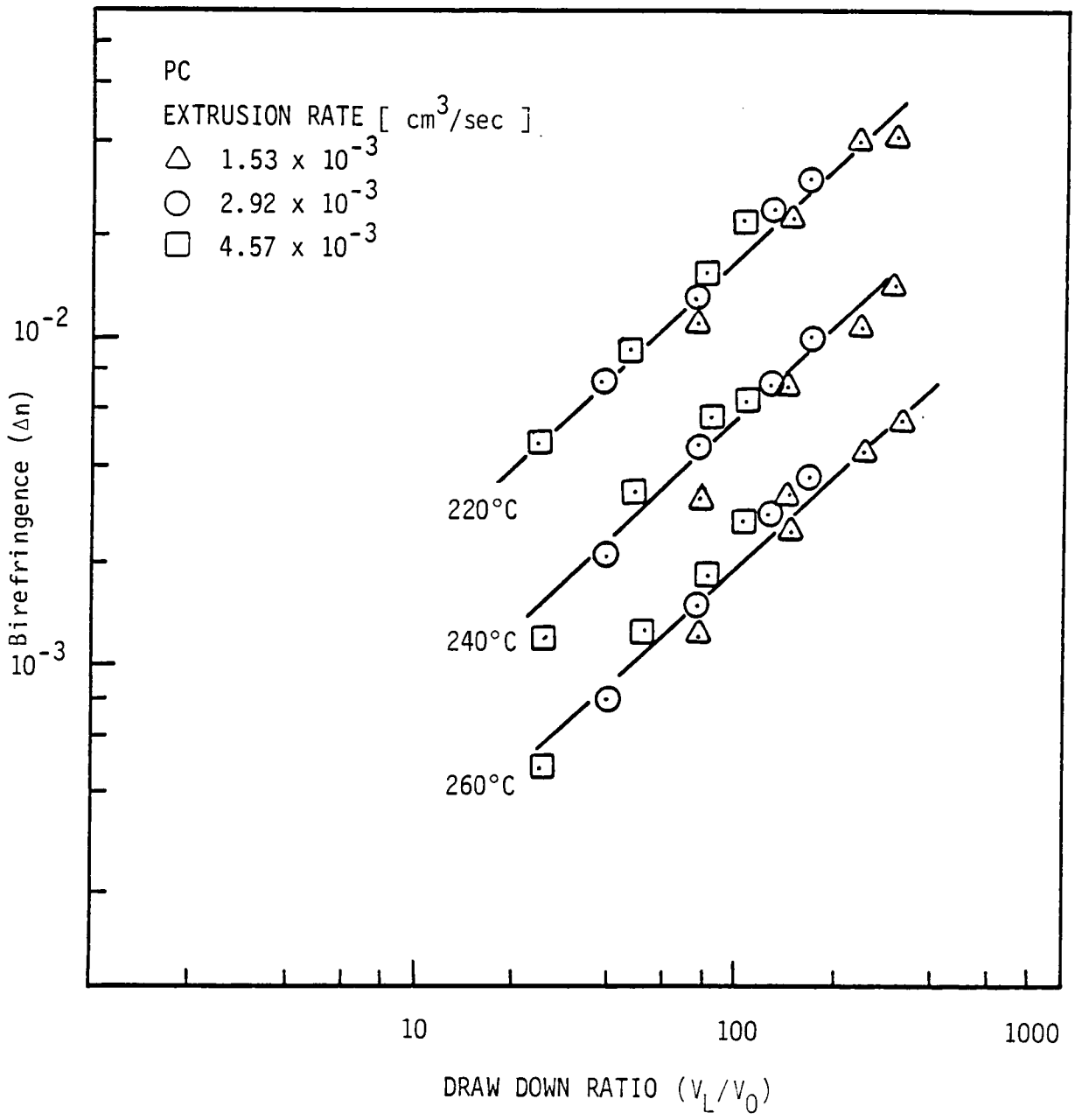


Figure IV-2. Birefringence versus drawdown ratio at different processing conditions for polycarbonate fibers.

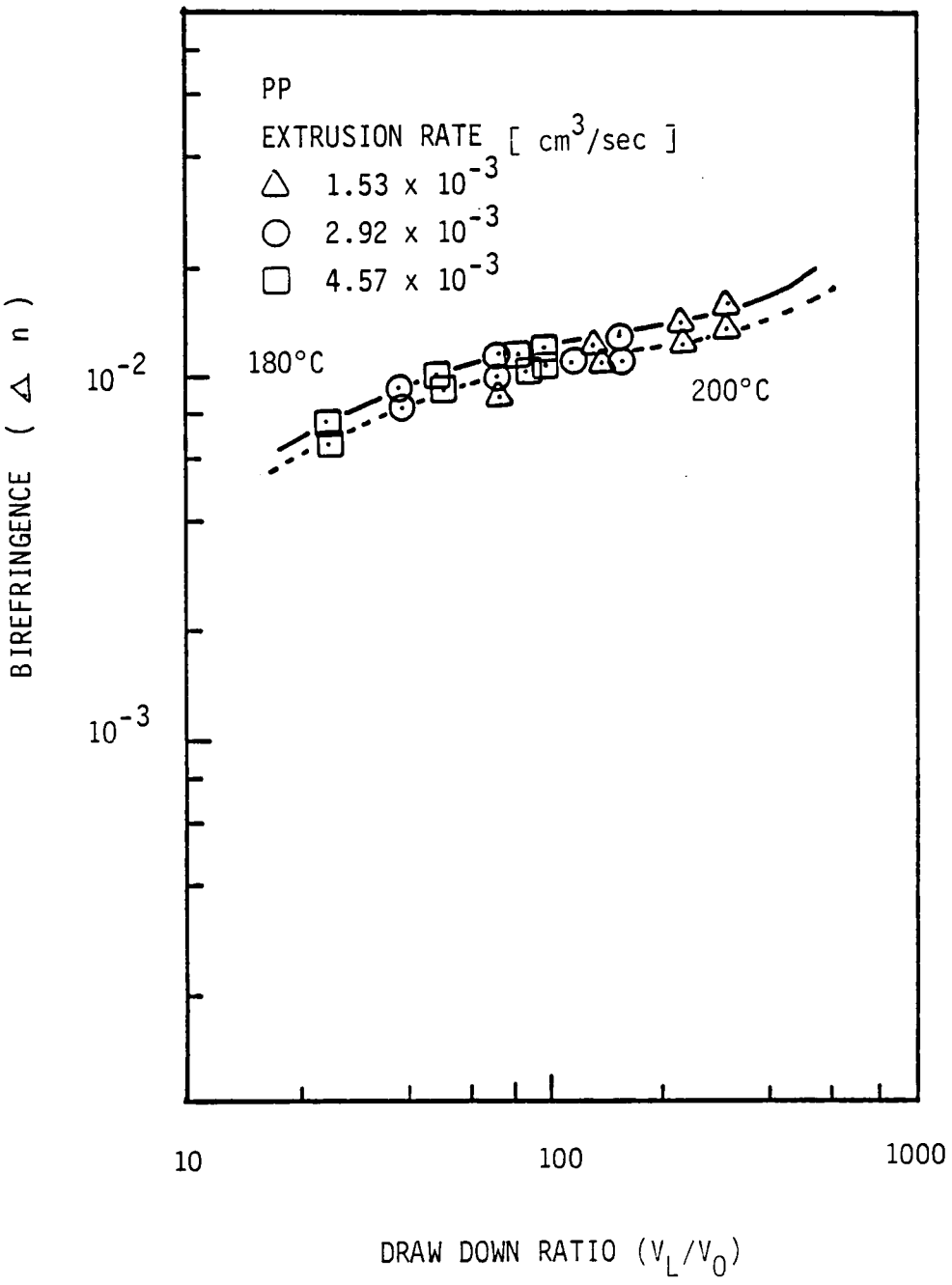


Figure IV-3. Birefringence versus drawdown ratio at different processing conditions for polypropylene fibers.

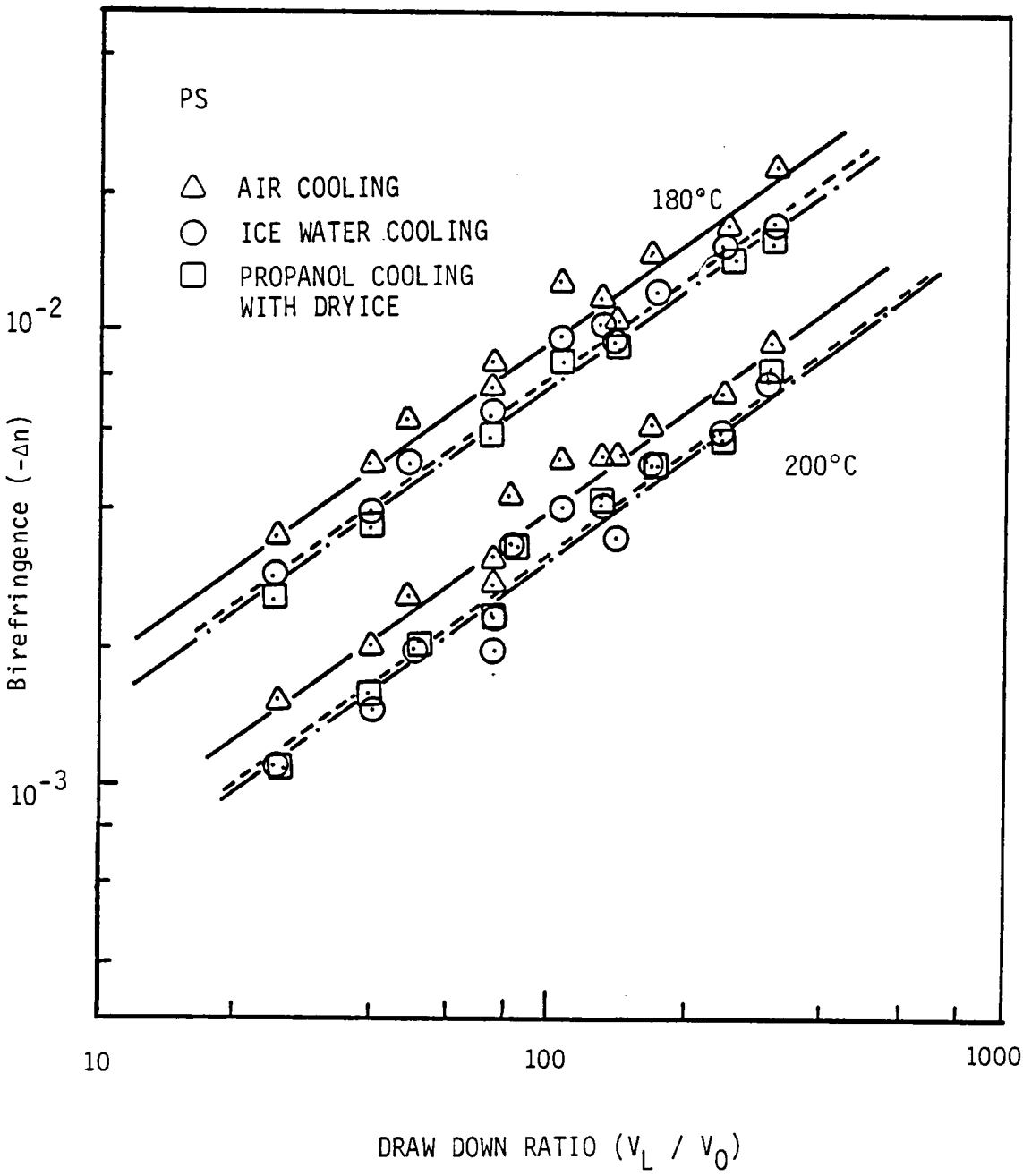


Figure IV-4. Cooling condition effects on birefringence (PS).

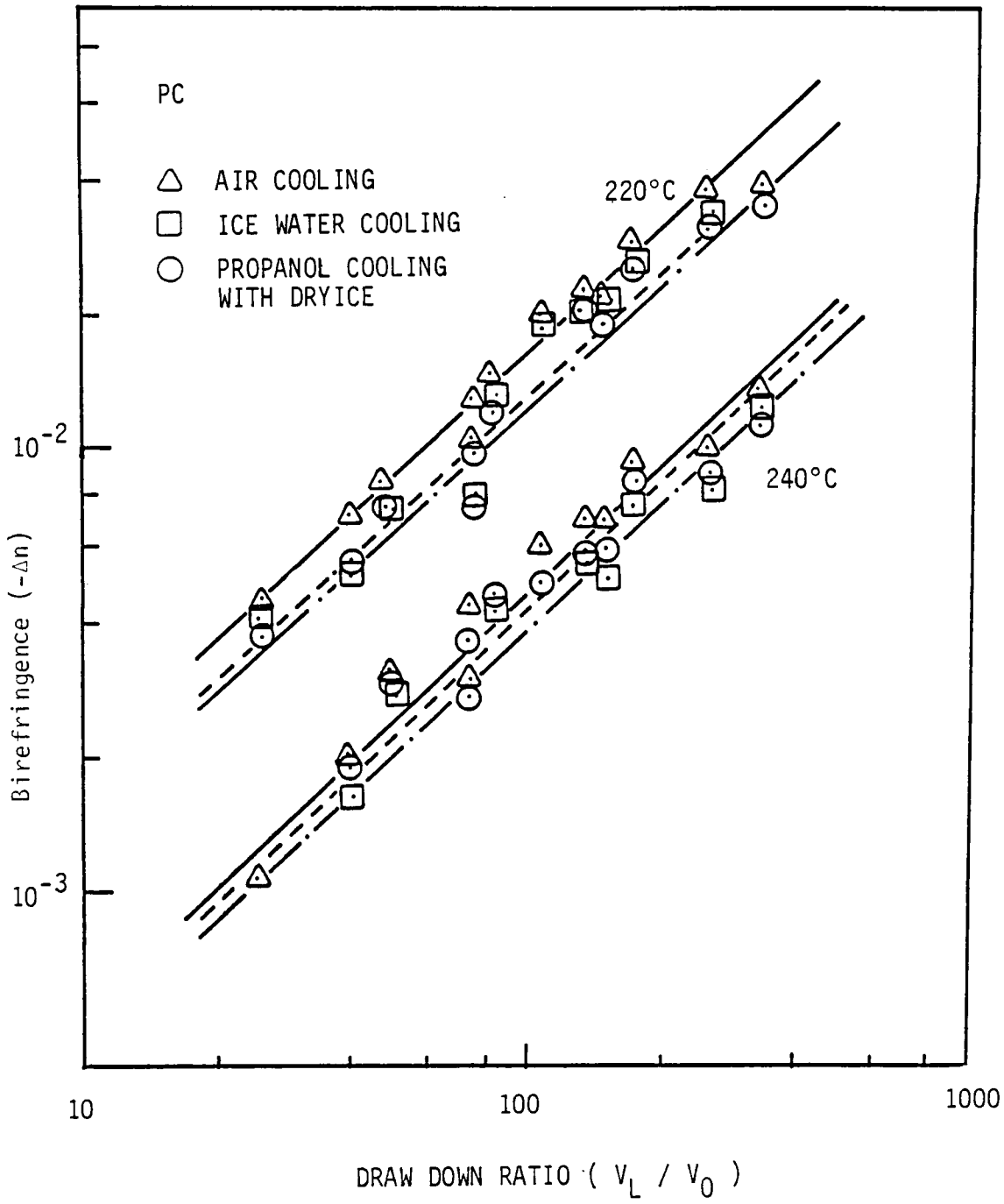


Figure IV-5. Cooling condition effects on birefringence (PC).

We replot the birefringence Δn in Figures IV-6, IV-7 and IV-8 as a function of spinline stress. In the case of polystyrene and polycarbonate fibers, the birefringence is linearly related to the spinline stress. There is a tendency for Δn to increase less rapidly and linearly at the higher stresses. The behavior is independent of quenching conditions. Stress optical coefficient of -3500 Brewster we obtained for polystyrene, and 5500 for polycarbonate. The behavior of polypropylene is different. The behavior is not linear and the birefringence of the quenched samples are lower at small spinline stress.

4.1.2. Discussion

Polystyrene fibers have negative birefringence due to the dependent phenyl rings as first clearly discussed by Gurnee (54). Our quantitative results are quite similar to Oda et al. (117) results (see Figure IV-6). From the viewpoint of cooling effects on Δn, our data show some deviation from linear line with different cooling conditions. The longer the distance from the die to the bath, the more linear dependence of Δn vs. stress relationship. Our fibers did not appear to exhibit draw resonance type nonuniformities.

Oda et al. determined a stress optical coefficient of 4500 Brewster based on a spinline stress is 5×10^6 dyne/cm^2. Our value is smaller than that of Oda et al. because we chose the average value over all range of stresses.

Oda et al. (117) hypothesize that flow birefringence of the melt is frozen in during vitrification. Our experimental results

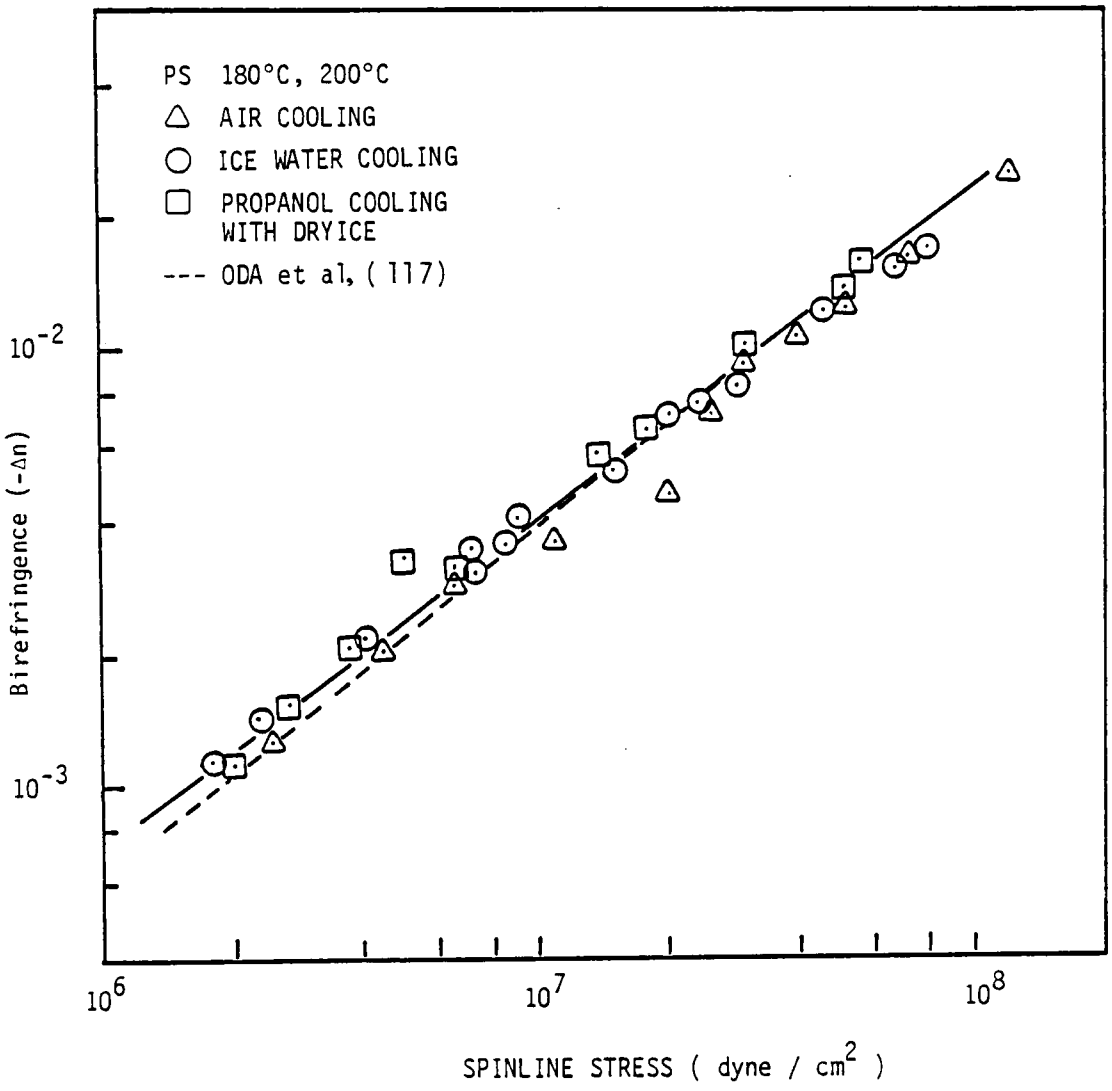


Figure IV-6. Relationship between applied stress and birefringence for polystyrene fibers.

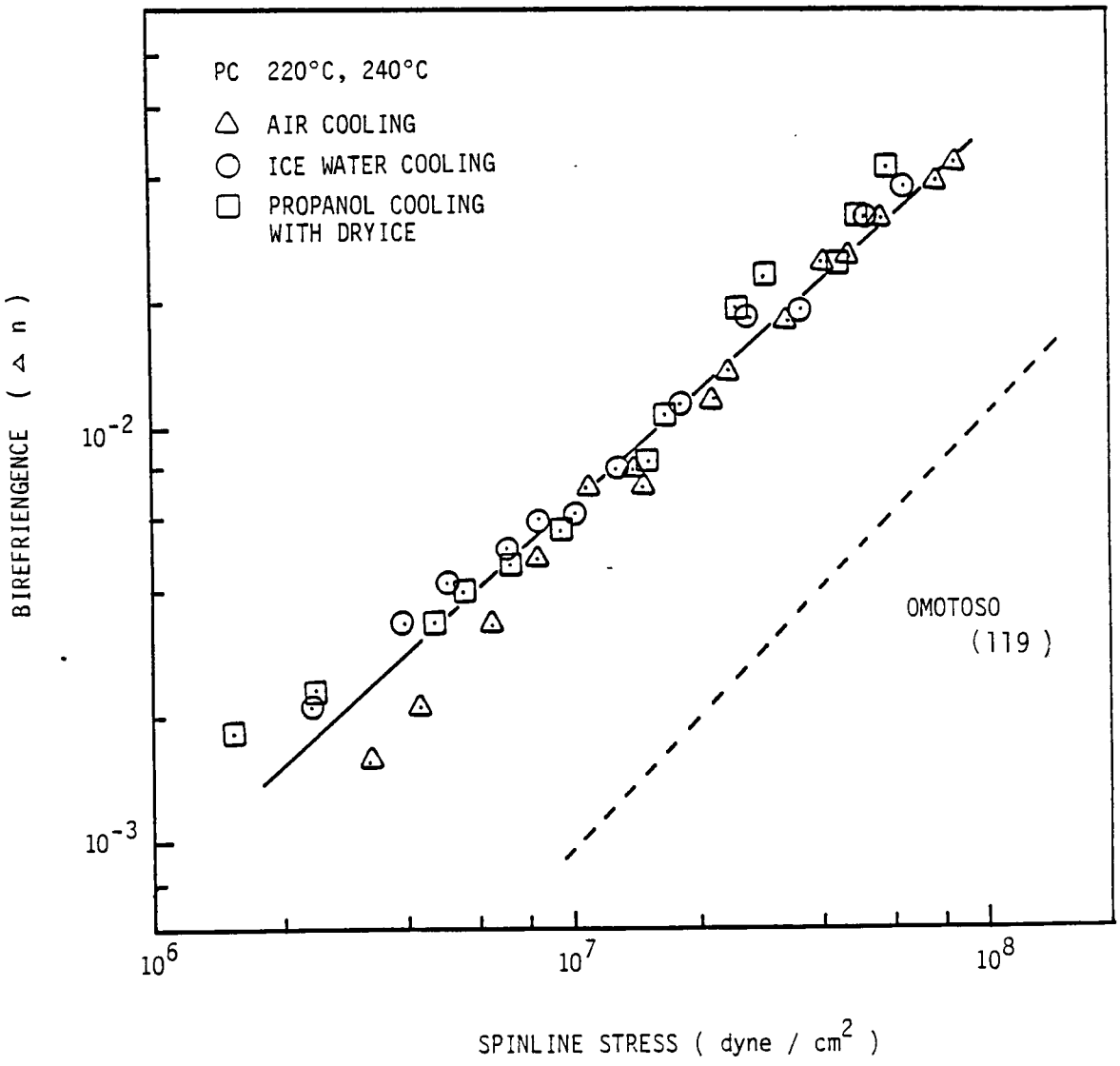


Figure IV-7. Relationship between applied stress and birefringence for polycarbonate fibers.

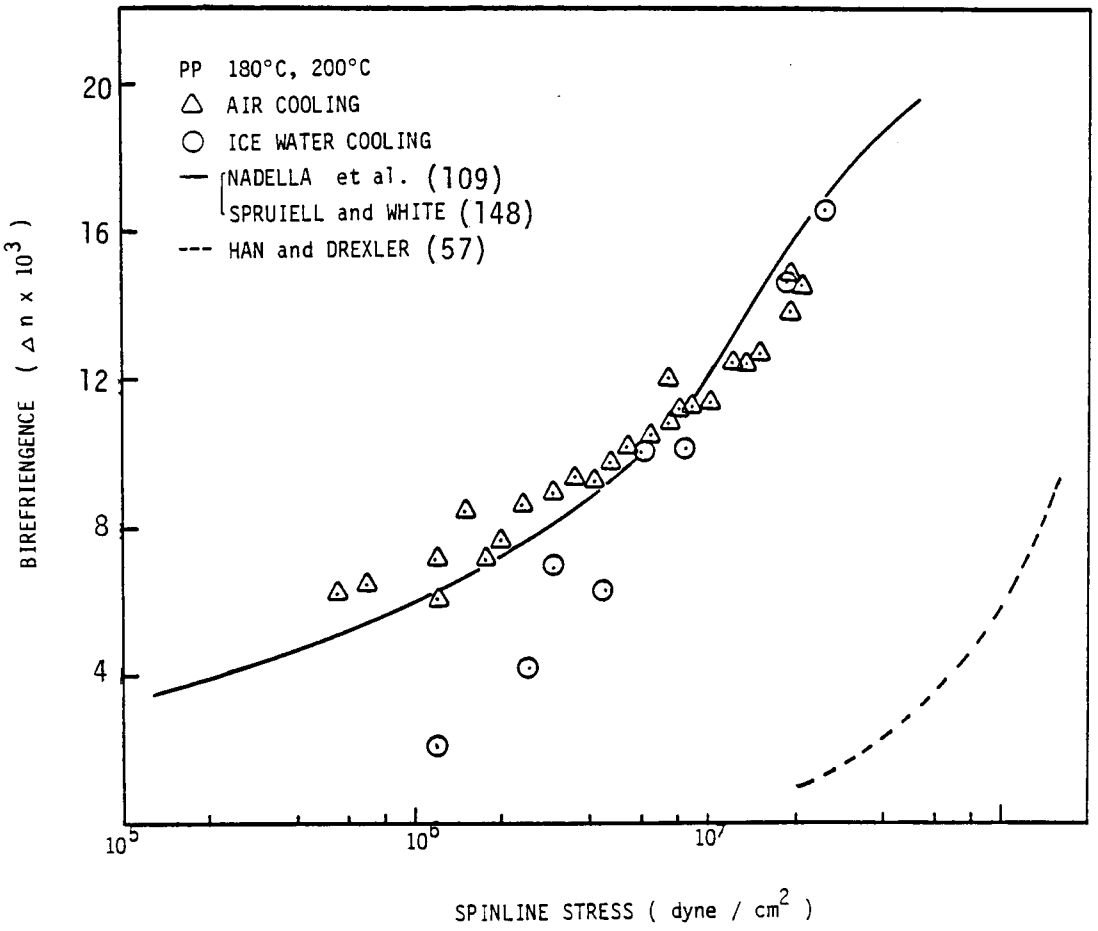


Figure IV-8. Relationship between applied stress and birefringence for polypropylene fibers.

reconfirm that behavior. The values of 4500-5000 Brewsters is very close to that determined for isothermal and nonisothermal melts (159).

The results for polycarbonate fibers are very different from those reported earlier by Omotoso (119) (see Figure IV-7). She found the stress optical coefficient as 1030 Brewster. Omotoso's value seems very low. It is comparable to the stress-optical constants of polyethylene (57) as aliphatic hydrocarbon. The value should be expected to be much higher as found here.

Polypropylene fibers have quite different behavior compared to polystyrene and polycarbonate fibers. Our birefringence stress data agrees well with previous experimental studies in the literature. The behavior is not linear and must be associated with crystallization in the spinline. We plot Han and Drexler (57) data of Δn vs. stress for polypropylene melts in Figure IV-8 together with our experimental results. These data predict much lower Δn at any stress. The higher value of Δn in the spun fiber is associated with crystallinity. Figure IV-8 shows that birefringence of air cooled fibers is much higher than that of ice water cooling at low stress regions. The lower values of Δn for the cold bath quenched fibers may be associated with the formation of a smectic rather than monoclinic crystalline phase as described by Nadella et al. (109). The smectic structure seems associated with rapid quenches and low spinline stresses.

The general behavior of the plot of Δn vs. stress is similar in amorphous fibers such as polycarbonate, polystyrene and polyethylene terephthalate (see Figure IV-9). The result of polyethylene terephthalate is taken from Hamana et al.'s work (56). They found that the stress optical coefficient of polyethylene terephthalate is 7000-8000 Brewsters. From Figure IV-9 we found the slopes of polycarbonate and polyethylene terephthalate are a little higher than those of polystyrene fibers. These results might be associated with crystallinity. We follow up this question in Chapter VI. We also observe that the data point in high stress regions seems to deviate from the linear line. Matsumoto and Bogue (98) have suggested that this deviation starts at 10^8 dyne/cm^2. Our results show similar tendencies.

We now extend the previous discussion by introducing the Hermans orientation factor. Figure IV-10 shows a unique relationship between Hermans orientation factor defined by

$$f = \Delta n/\Delta^0 \qquad [4\text{-}1]$$

and stress for amorphous polymers including polystyrene, polycarbonate and PET. From Equation [2-3] we may write

$$f = C/\Delta^0 \, \sigma_{11} \, . \qquad [4\text{-}2]$$

Stress optical coefficient C has been proposed by Kuhn and Grun (88) to have the form:

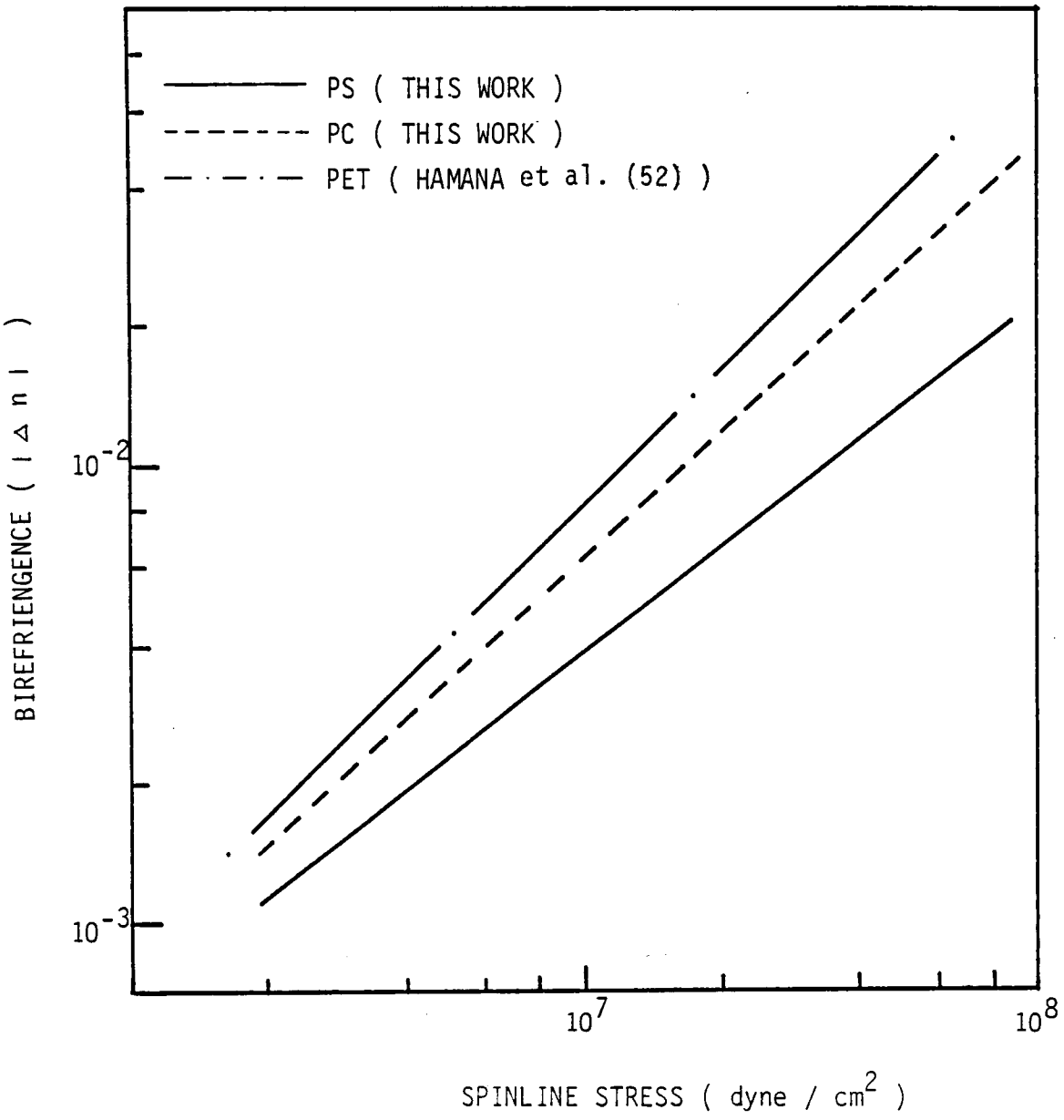


Figure IV-9. Comparison about the relationship Δn and stress for PC, PS and PET fibers.

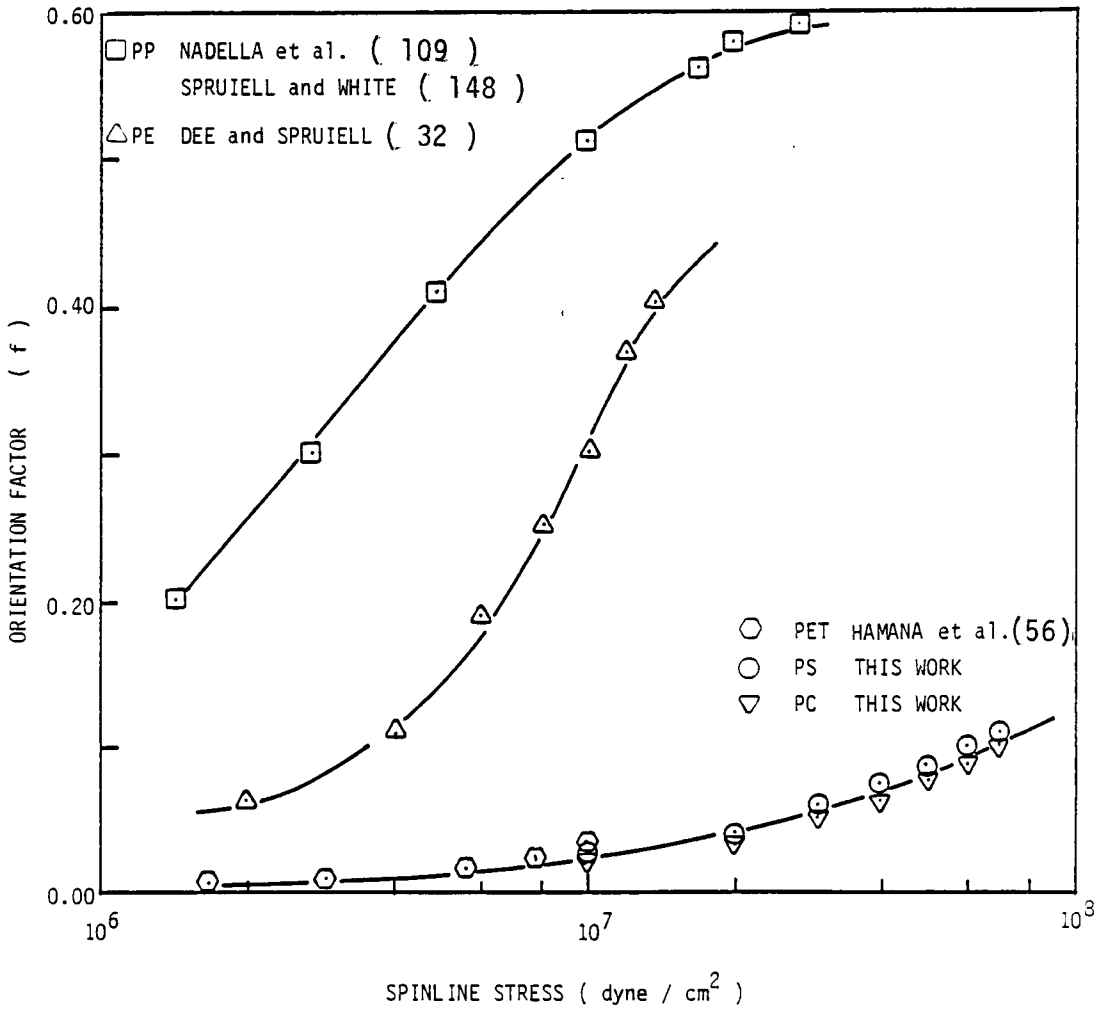


Figure IV-10. Orientation factors as a function of stress for amorphous polymer and crystallized melt spun fiber.

$$C = \frac{2\pi}{45\ kT} \frac{(\bar{n}^2 + 2)^2}{\bar{n}} (\alpha_1 - \alpha_2) \ . \qquad [4\text{-}3]$$

This leads to

$$\frac{C}{\Delta^0} = \frac{1}{5\ kT} \frac{M}{N\rho} \qquad [4\text{-}4]$$

which is essentially independent of all material characteristics and varies weakly with temperature. We take Δ^0 for polystyrene, polycarbonate, polypropylene, and polyethylene to be -0.16, 0.35, 0.033 and 0.055, respectively. Table IV-1 shows the value of C/Δ^0 as a universal constant. In Figure IV-10 we plot f vs. stress for amorphous fibers and crystallized polyethylene and polypropylene fibers. The value of f for crystalline fibers are much higher than those for the amorphous fibers. Crystallization in the spinline increases chain orientation. Generally amorphous materials, polystyrene, polycarbonate, and PET have low value of f.

4.2. BIREFRINGENCE DISTRIBUTION ACROSS THE THICKNESS DIRECTION

4.2.1. Results

Birefringence distributions in thick filaments with diameter from 200 μm to 400 μm were investigated using the wedge method as described in Chapter III. Figures IV-11 and IV-12 show typical fringe patterns on wedges for polycarbonate fibers and polystyrene fibers. These were taken in a polarized light microscope with crossed and

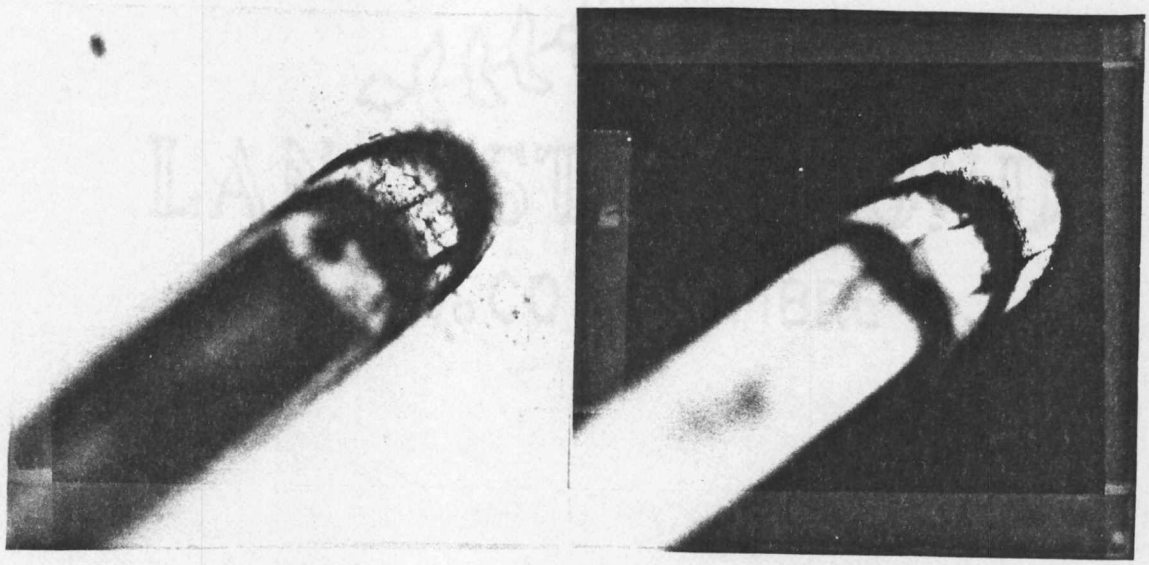
Table IV-1. Ratio of stress-optical coefficient to intrinsic birefringence (PS, PC, PET, PP, PE).

Material	Δ°	C (Brewster)	C/Δ° (Brewster)
PS	-0.16; Stein (152)	4500; Oda et al. (117)	28000
		3500; this study	15600
PC	0.35; Omotoso (119)	5500; this study	15700
PET	0.275; Dumbleton (40)	7000; Hamana et al. (56)	25400
PP	0.033; Samuels (133)	750	22700
PE	0.058; Stein et al. (150)	1550	26700

A] drawdown ratio = 127

parallel polarizer

cross polarizer



B] drawdown ratio = 30

parallel polarizer

cross polarizer

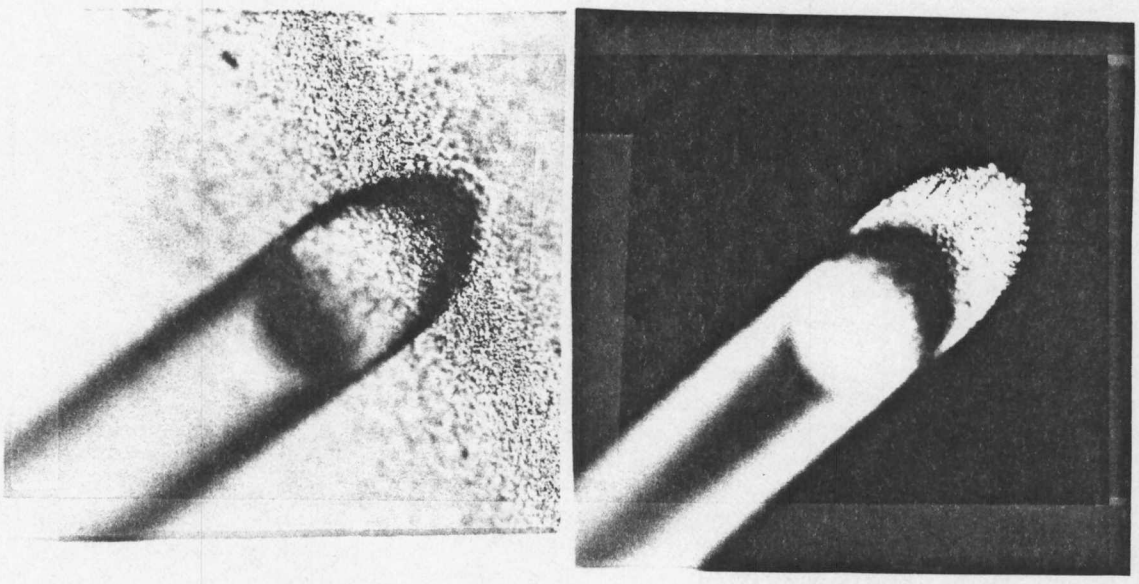
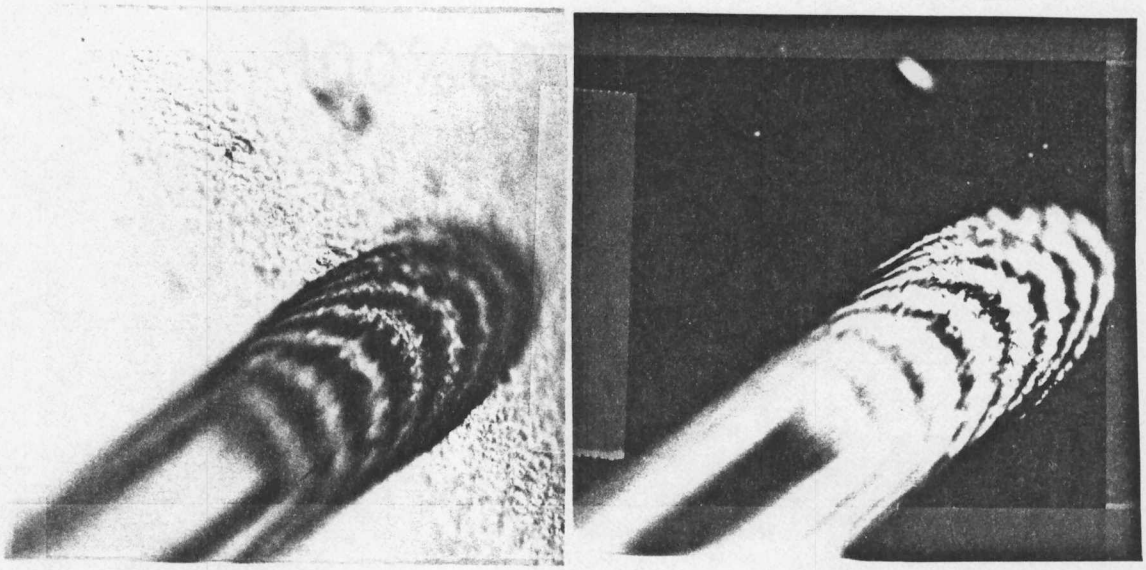


Figure IV-11. Typical fringe patterns on wedge for polystyrene fibers.

A] drawdown ratio = 127

parallel polarizer cross polarizer



B] drawdown ratio = 30

parallel polarizer cross polarizer

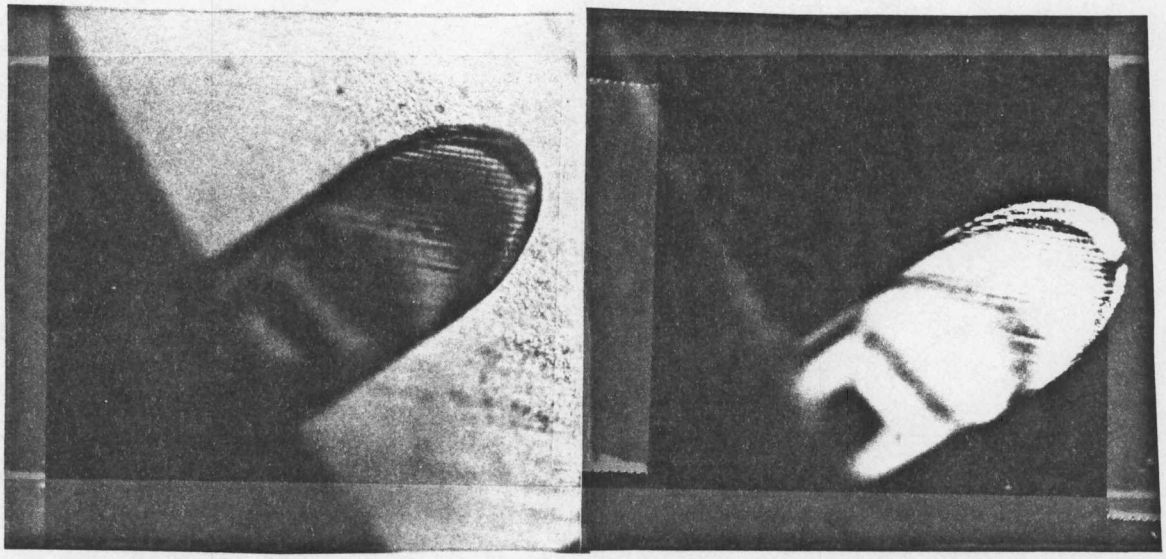


Figure IV-12. Typical fringe patterns on wedge for polycarbonate fibers.

parallel polarizer. High mean birefringence insures many fringe lines. Each fringe line indicated the local birefringence at that position. It was found that the distance between fringes is not uniform along the oval diameter. Measuring the distance between fringes allows determination of the birefringence distribution.

Our major interest is determining how the birefringence distribution is related to cooling and processing conditions. Three different quenching conditions were involved. Fibers with drawdown ratios: 30, 60, 127, were chosen to examine processing condition effect. It was found that ice water and isopropanol cooling gave a more pronounced reduction of birefringence in the fiber core compared to air cooling. Thicker fibers have much larger birefringence reduction in the center of the fiber. Generally a symmetrical distribution profile was found. Reductions of surface birefringence of 75% and 80% are common. The computed birefringences of different quenching and drawdown conditions are summarized in Figures IV-12 through IV-17.

4.2.2. Discussion

The wedge method is one of the most powerful methods to determine the orientation distribution in fibers. Gurnee (54) has determined birefringence distribution on PS monofilaments by means of the wedge method. His samples were made using special equipment which has several baths to cool down and stretch the filament. Diameters of his polystyrene monofilament were 504 μm and 1339 μm as compared to our 200-400 μm. The mean birefringences were

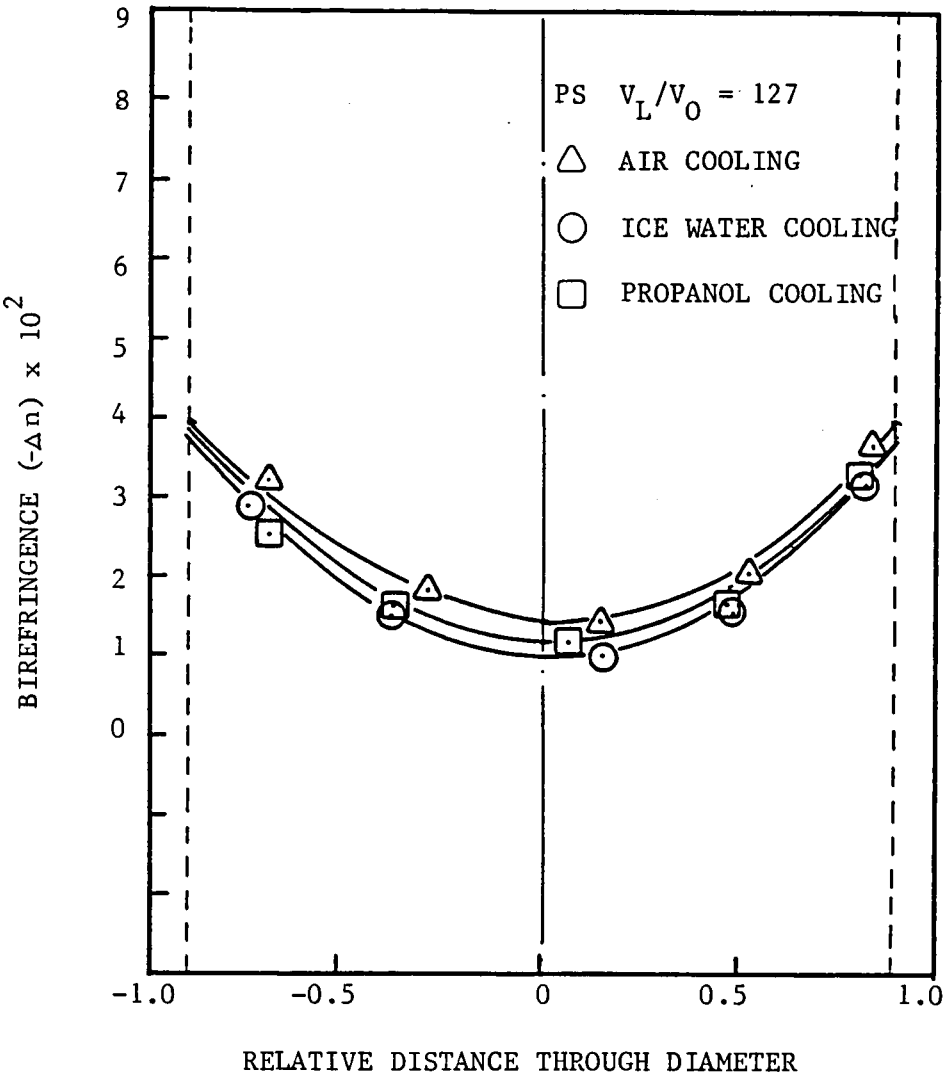


Figure IV-13. Birefringence distributions for polystyrene fibers. (Drawdown ratio = 127.)

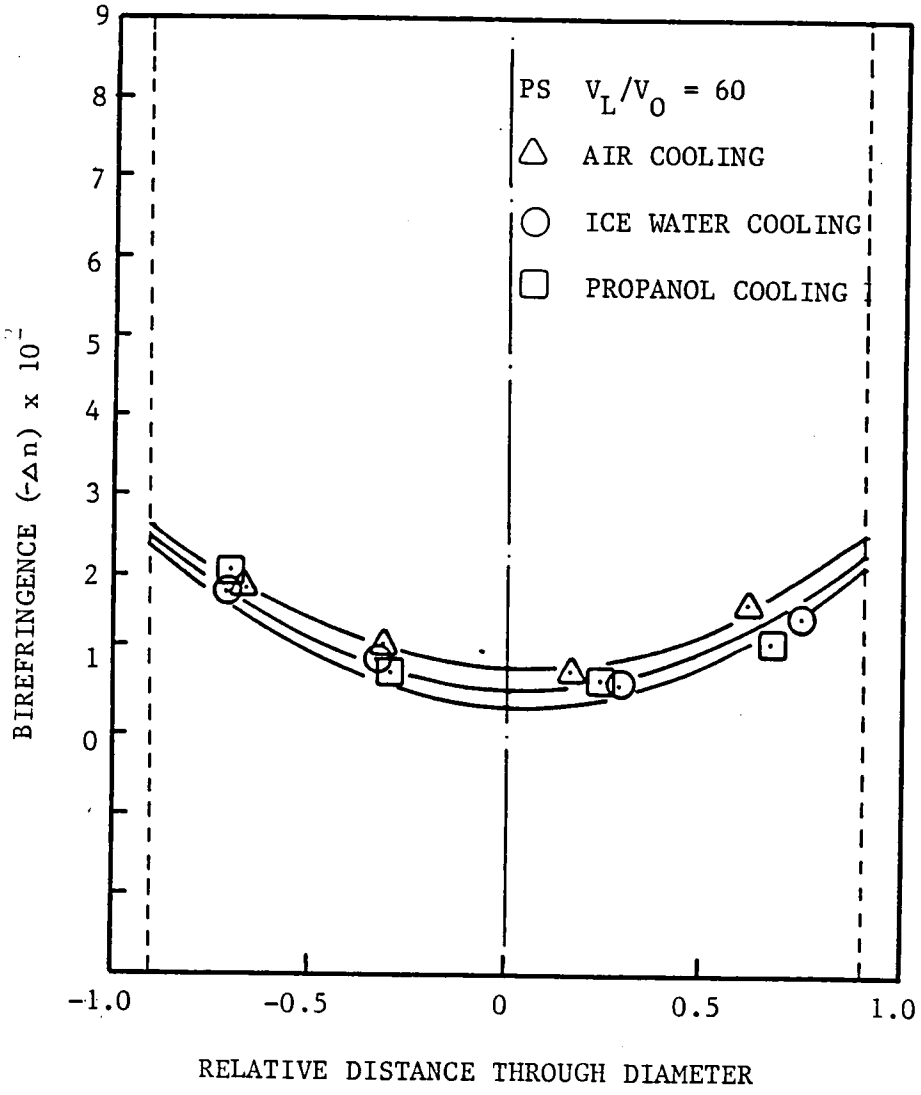


Figure IV-14. Birefringence distributions for polystyrene fibers. (Drawdown ratio = 60.)

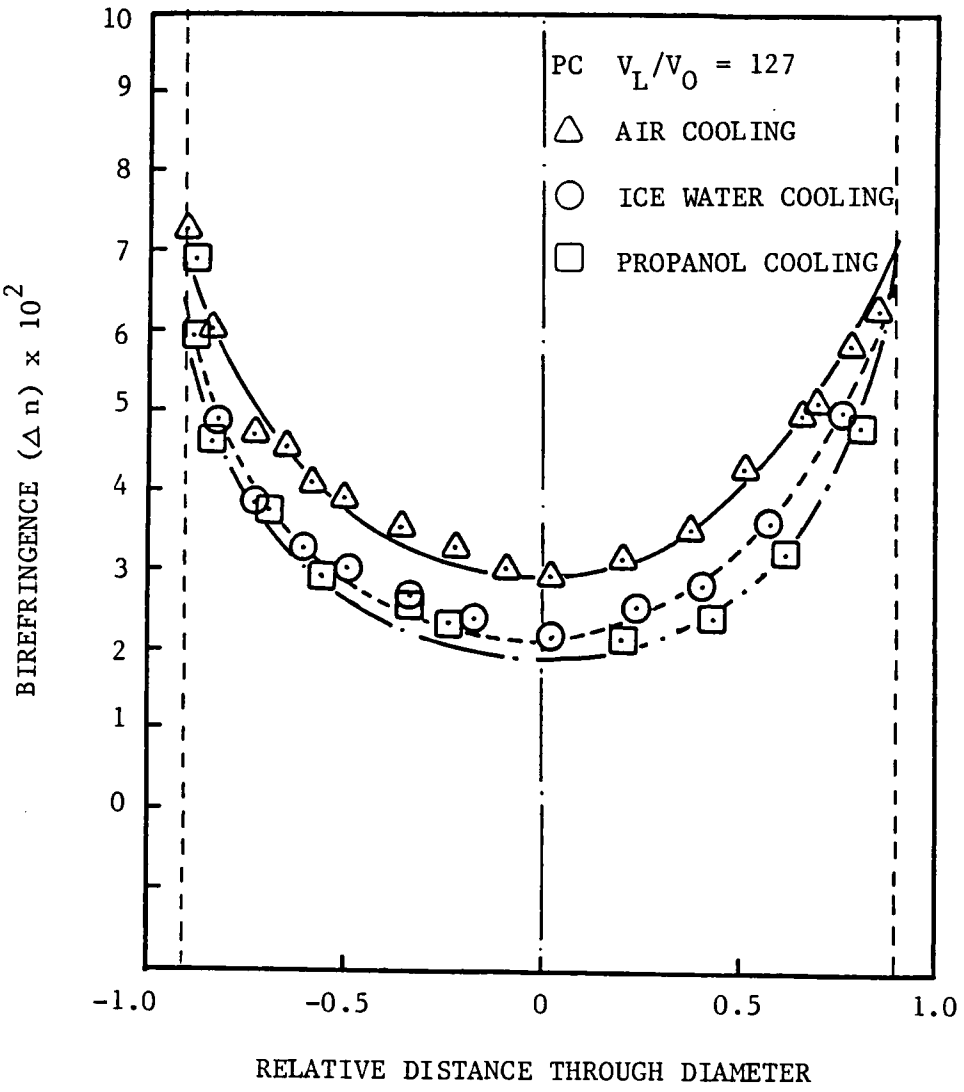


Figure IV-15. Birefringence distributions for polycarbonate fibers. (Drawdown ratio = 127.)

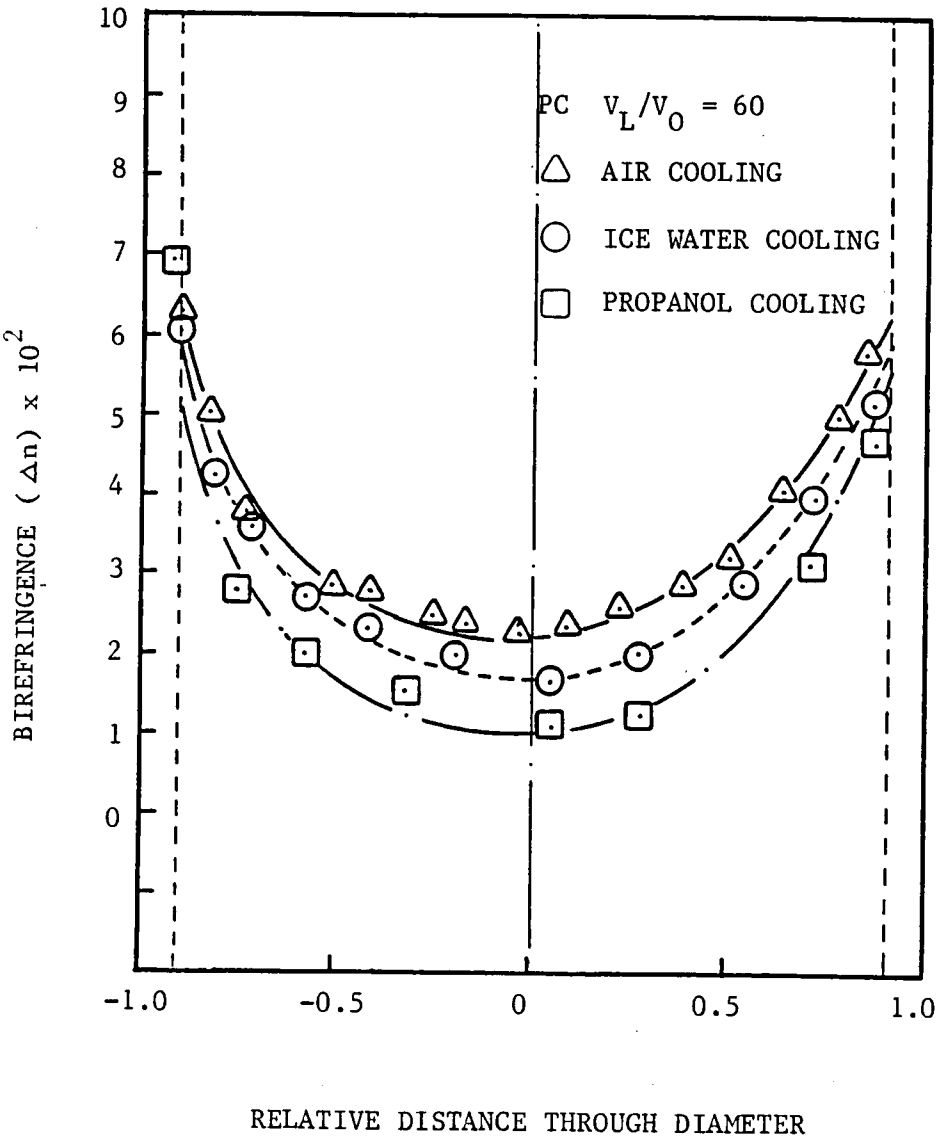


Figure IV-16. Birefringence distributions for polycarbonate fibers. (Drawdown ratio = 60.)

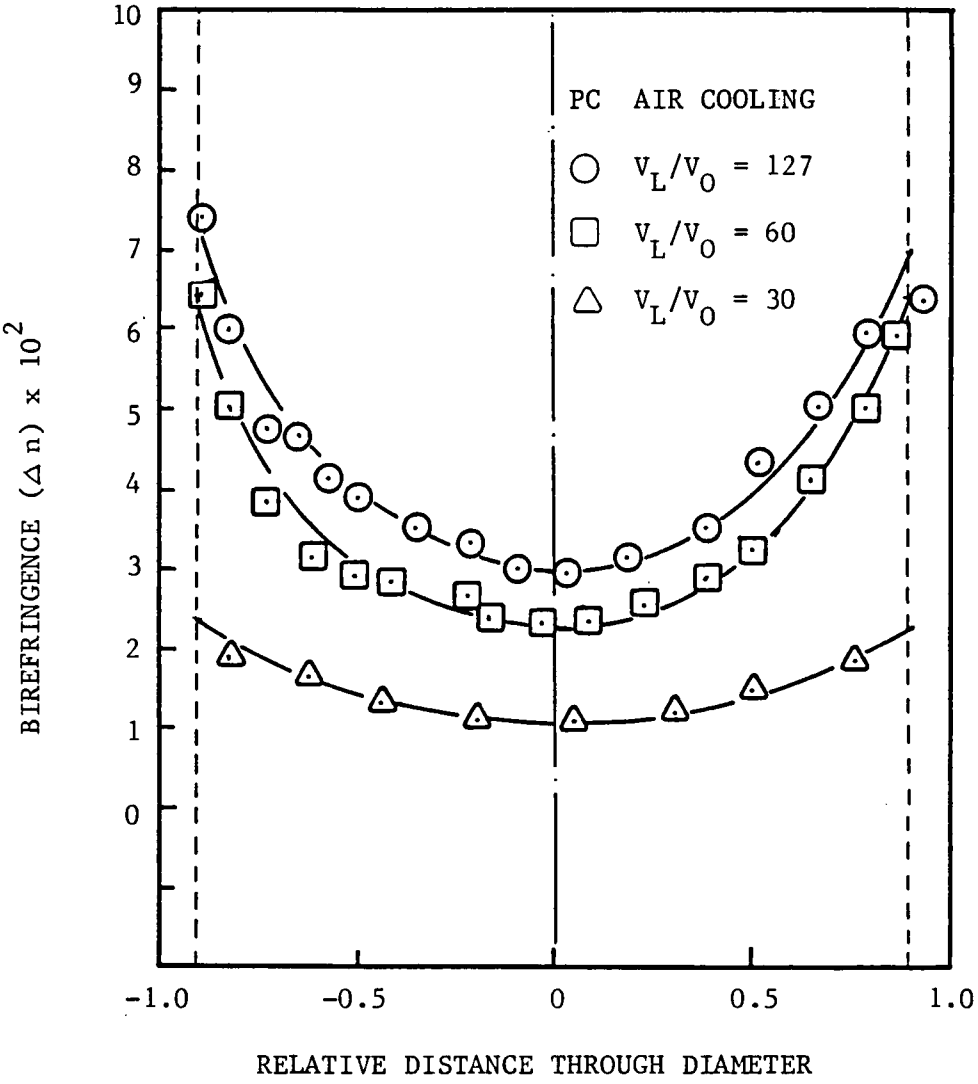


Figure IV-17. Birefringence distributions for polycarbonate fibers. (Air cooling.)

were -2.37×10^{-2} and -1.02×10^{-2}, respectively. He obtained quantitative fringe patterns which consisted of 21 fringe lines. It allowed him to determine the birefringence distribution accurately. He has found that distance between fringes was not uniform - long distance in core, short distance in center. Generally high orientation on a surface, low orientation on a core were obtained. He also observed that thicker fiber had more pronounced orientation distribution. Similar results were found in our study. However, our accuracy is not the same as the results of Gurnee because we did not obtain as many as in his case. In the case of polycarbonate fibers we obtained more fringe lines on wedge compared to polystyrene fibers. It allows us to have better accuracy.

The orientation distribution across the diameter direction may be explained by the temperature distribution between the core and the surface. Thick fibers should have larger temperature distribution compared to thin fibers because of the form of solutions of the heat conduction equation.

Different cooling conditions allow different temperature distribution because of heat transfer coefficient change and quenching temperature. Thus ice water and isopropanol cooling created more pronounced orientation reduction in the core. However, little difference seems to be found between ice water cooling and isopropanol although the quenching temperature in isopropanol (-45°C) is lower than that of ice water.

CHAPTER V

ANALYSIS OF SPINNING DYNAMICS AND ORIENTATION IN THE THICK FILAMENT

5.1. PREDICTION OF SPINNING DYNAMICS

5.1.1. Approach

In this chapter we will attempt to predict the mean birefringence and the birefringence distribution across the diameter direction and then compare these predicted values with our experimental values which were described in Chapter IV. To do so, the prediction of spinning dynamics along the spinline must be carried out.

The spinning dynamics were analyzed using the procedure of Kase and Matuso's (79) modelling. They gave a combined dynamic and heat transfer analysis of the spinline. It allows us to predict the filament diameter, temperature, velocity and heat transfer coefficient as functions of distance x from the spinneret.

By solving a set of two partial differential equations simultaneously (force balance equation and heat balance equation), they obtained three basic equations which have forms:

$$\frac{dT}{dx} = - 1.67 \times 10^4 \frac{(T - T_s)}{G^{2/3} \rho^{1/3} A^{1/6}} \qquad [5\text{-}1a]$$

$$F = \frac{h\, G^{0.334}\, C_p^{-1}\, \rho^{-1.334} \int_{A_G}^{A_1} A^{-1.167}\, dA}{\int_{T_G}^{T_1} \frac{1}{\beta(T - T_s)}\, dT} \qquad [5\text{-}1b]$$

$$A_N = (1000\, F \cdot C_p\, \rho^{1.334}\, G^{-0.334} \int_{T_G}^{T_1} \frac{1}{\beta(T - T_s)} \times dA + A_1^{-0.167})^{-\frac{1}{0.167}} \qquad [5\text{-}1c]$$

Those three equations were derived by several assumptions as listed below: (a) polymers are Newtonian; (b) the molten polymer filament is circular in cross section; (c) heat conduction in the longitudinal direction is negligible; (d) temperature is uniform across cross sectional area; (e) the component of spinning tension due to acceleration, gravity and resistance action on filament is neglected; (f) the term for radiant heat loss is neglected; (h) there is no air cooling flow during the processing.

In Equation [5-1a], heat transfer coefficients were evaluated by Kase and Matsuo's (79) empirical Nu-Re relation which has a form

$$h_{air} = 4.73 \times 10^{-5}\, A^{-0.344}\, v^{0.334} \,. \qquad [5\text{-}2]$$

In our study we neglect air cooling flow. Thus the factor (1 + K) does not appear in Equation [5-2]. We also apply this equation to ice water cooling by introducing the Pr number as

$$Nu_{water} = 0.37 \quad Re_{water}^{0.334} \quad Pr_{water}^{0.334} \qquad [5\text{-}3]$$

where the constant 0.37 was obtained by writing

$$0.42 = C \times (Pr_{air})^{0.334} \quad C = 0.37 \ .$$

Equation [5-3] can be rewritten in the form

$$h_{water} = 76.3 \quad h_{air} \ . \qquad [5\text{-}4]$$

Calculation of tensions based on Equation [5-1b] have been carried out on an IBM computer with the computer program CALTEN as attached in the Appendix. This involves the numerical integration by Simpson's method.

Physical constants which were used in this study are presented in Table V-1. The constants are independent of temperature. Elongational viscosities were taken as three times the zero shear viscosity. The Arrhenious equation was applied to predict the shear viscosities at various temperatures.

The glass transition temperature was taken for polystyrene as 100°C and for polycarbonate as 150°C. These were used as solidification temperatures.

The area A, temperature T and velocity V were simultaneously obtained based on integration of Equations [5-1a] and [5-1c]. The integration was carried out by Simpson's method. The program SPIN was prepared for this purpose.

Table V-1. Physical constants for PS and PC.

	Unit	PS	PC
Density	g/cm^3	1.04	1.2
Specific Heat Coefficient	cal/g°K	0.32-0.38	0.3
Transient Temperature	°C	105-110	140-155
Conductivity	cal/sec cm °K	2.4×10^{-4} - 3.4×10^{-4}	4.64×10^{-4}

In the case of ice water cooling two heat transfer coefficients were used. Equation [5-2] was applied from the die to water surface (5 cm) and then Equation [5-3] was used to calculate the heat transfer coefficient in the water.

5.1.2. Results and Discussion

Figures V-1 and V-2 show the computed radius profile along the spinline for polystyrene and polycarbonate fibers with different drawdown ratios. It was found that the radius of fiber was fixed when fiber was solidified. Thicker fiber needs a longer spinline to solidify compared to thin fiber. Thicker fiber has more mass for the heat to penetrate and also possesses smaller heat transfer coefficients. Generally the radius decreases immediately below the die since polystyrene and polycarbonate have higher activation energy. A high activation energy results in greater elongational viscosity which is related to the spinning tensions. Thus polystyrene and polycarbonate fibers should have larger spinning tensions than polyolefin melts. This explanation can be confirmed by comparison with polypropylene and PET fibers' radius profile from Kase and Matuso (79). Since polypropylene and PET have smaller activation energy, their radius profile decreases slowly along the spinline.

Radius profiles along the spinline for ice water quenching were also described in Figures V-1 and V-2. These results are obtained by assuming that fiber surfaces solidify at water surface since the heat transfer coefficient changes dramatically in ice water. Consequently, the elongation ceased at the water

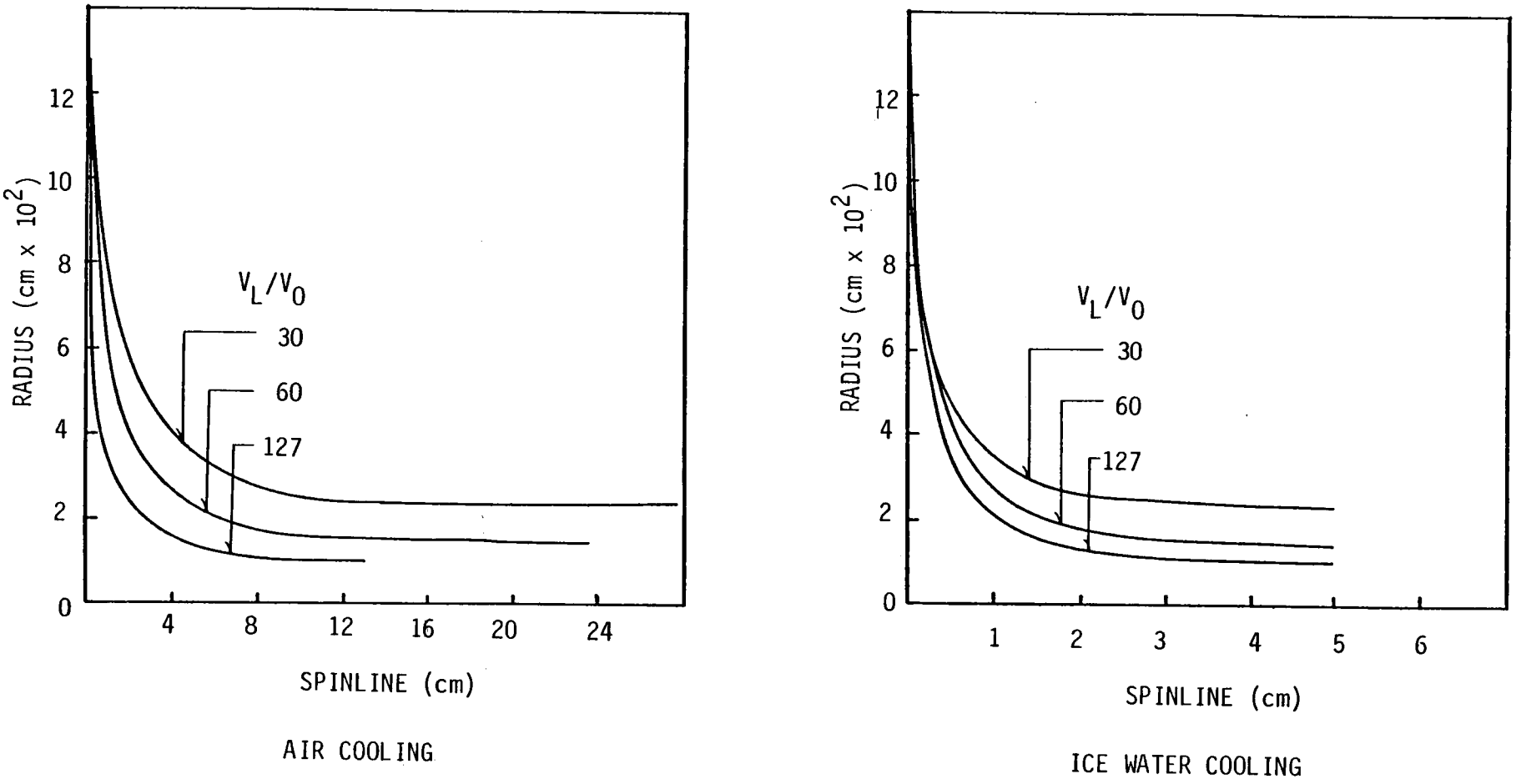


Figure V-1. Predicted radius profile along the spinline for PS fibers.

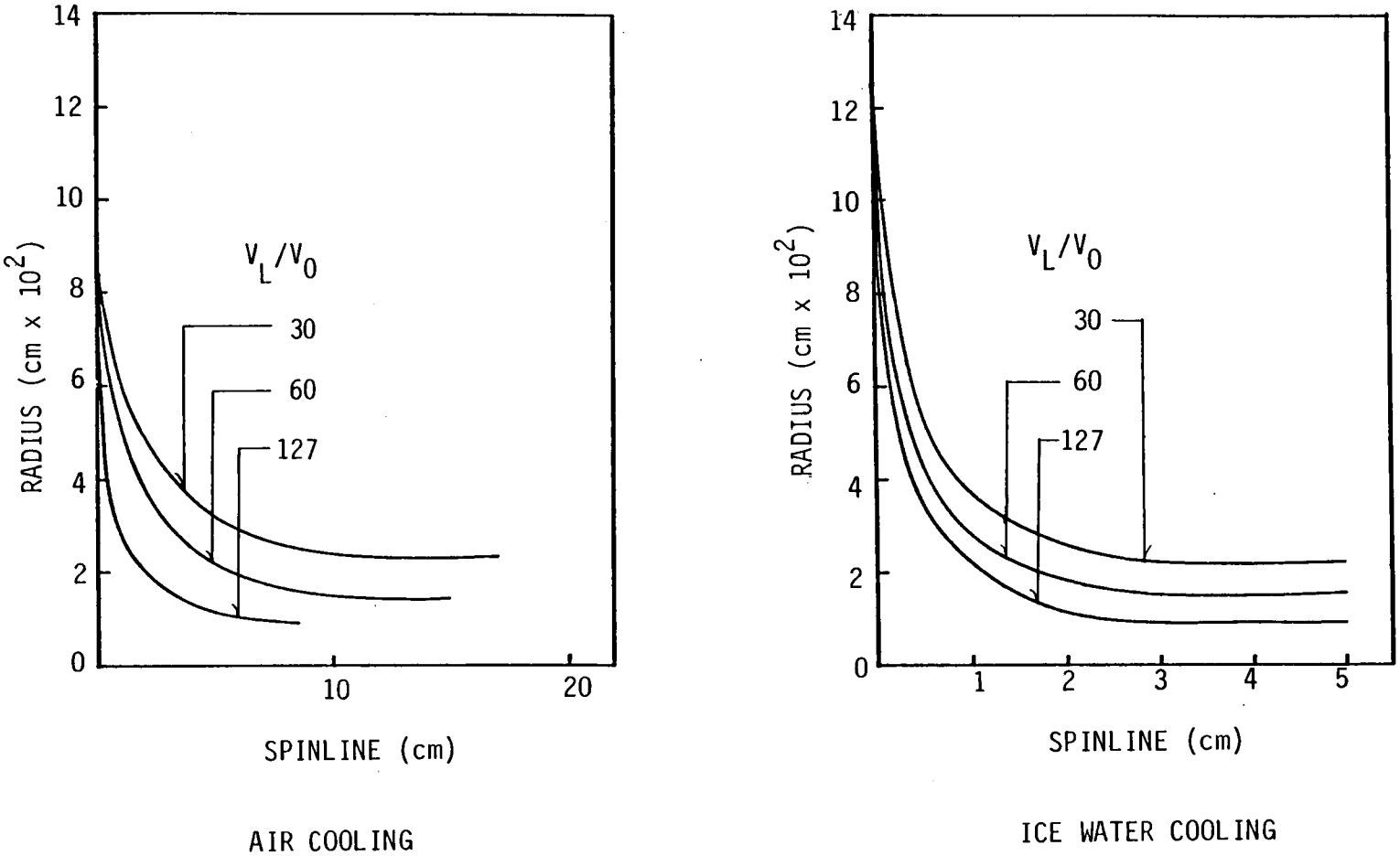


Figure V-2. Predicted radius profile along the spinline for PC fibers.

surface. It means that the final velocity (take-up velocity) occurred at the water surface. Final diameters were also calculated from the continuity equation.

In Figures V-3 and V-4, velocity profiles along the spinline were illustrated. It was found that velocity profile has more dependence on take-up speed than initial speed.

Temperature profiles were calculated with different diameter fibers. Figures V-5 and V-6 show that a thicker diameter fiber cooled down more slowly. In the case of ice water cooling, high spinline temperature was maintained until the fiber contacted the ice water and then it reached the transition temperature immediately. This result can be seen in Figures V-7 and V-8. The heat transfer coefficient along the spinline has a discontinuity at the ice water surface. We obtained the heat transfer coefficient in ice water cooling which is 76.3 times higher than that in air cooling.

5.2. PREDICTION OF MEAN ORIENTATION AND ORIENTATION DISTRIBUTION

5.2.1. Approach

Mean birefringence can be predicted from the calculated spinline tensions and stress optical coefficients. It can be written

$$\Delta\bar{n} = C\,\sigma_{11} \quad . \qquad [5\text{-}5]$$

In order to calculate birefringence distributions across the fiber diameter, it is necessary to know the temperature distribution.

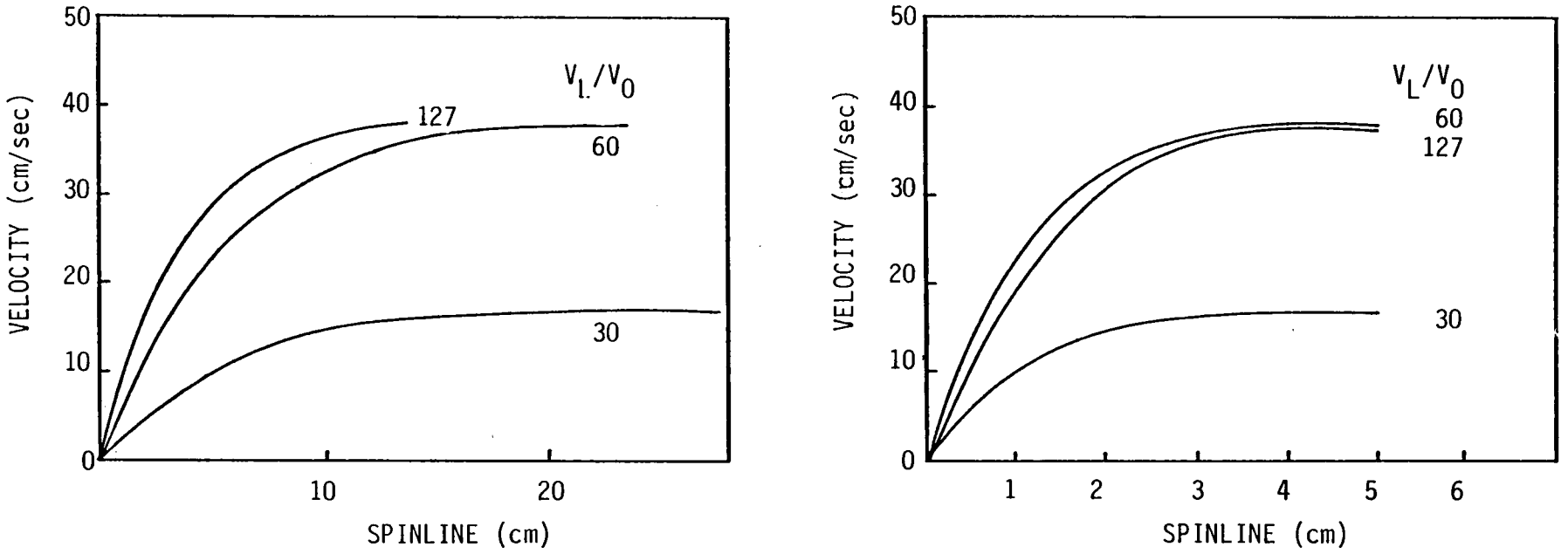


Figure V-3. Predicted velocity profile along the spinline for PS fibers.

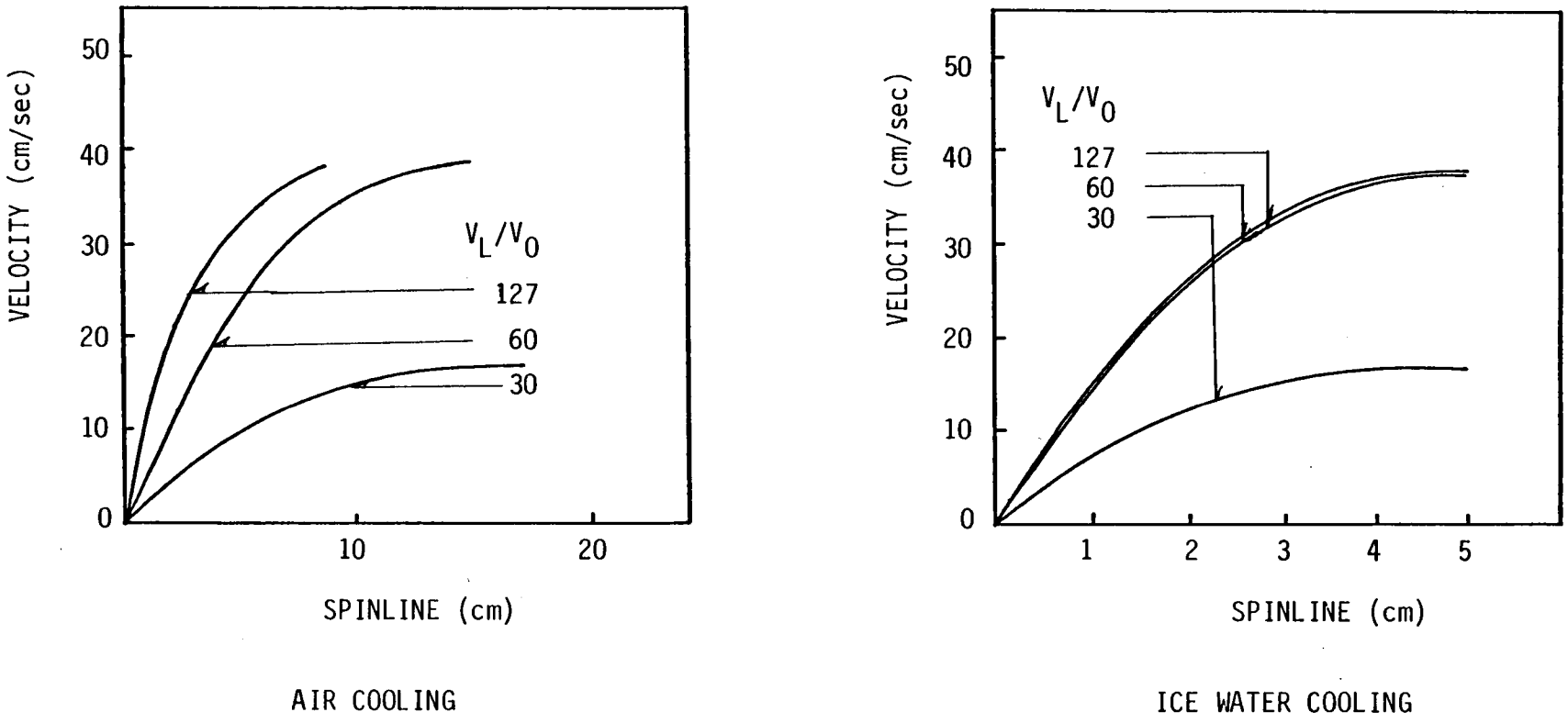


Figure V-4. Predicted velocity profile along the spinline for PC fibers.

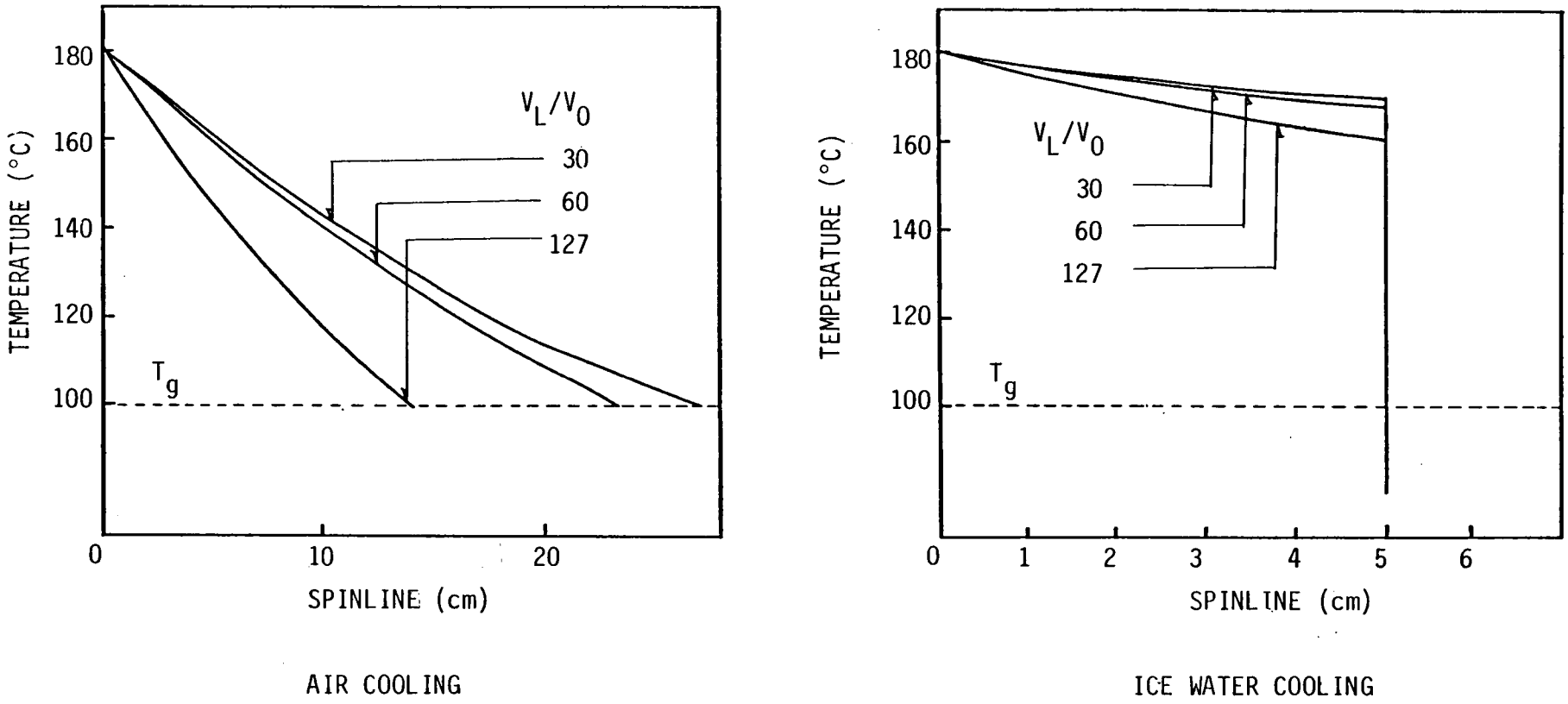


Figure V-5. Predicted temperature profile along the spinline for PS fibers.

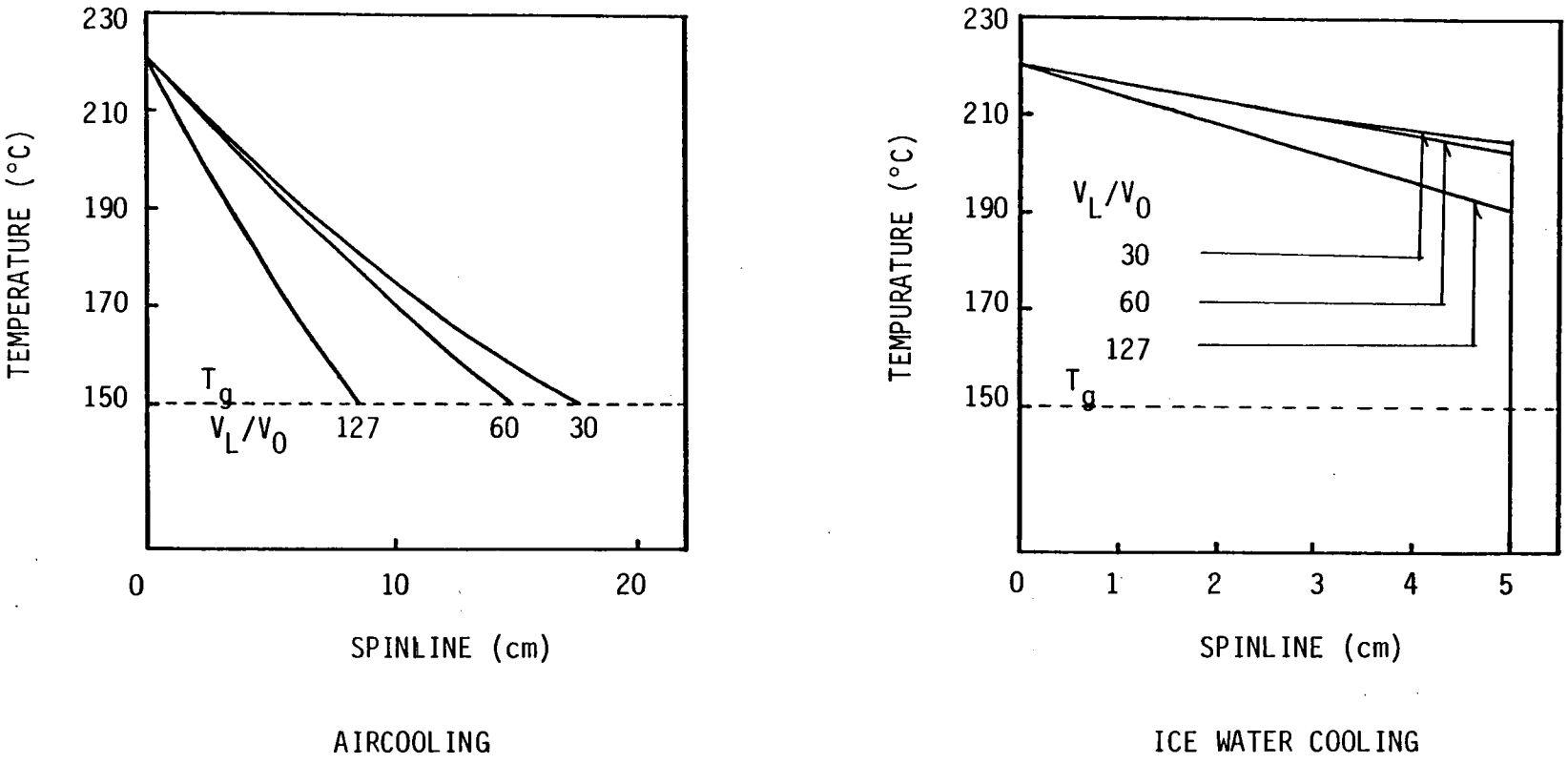


Figure V-6. Predicted temperature Profile Along the Spinline for PC Fibers.

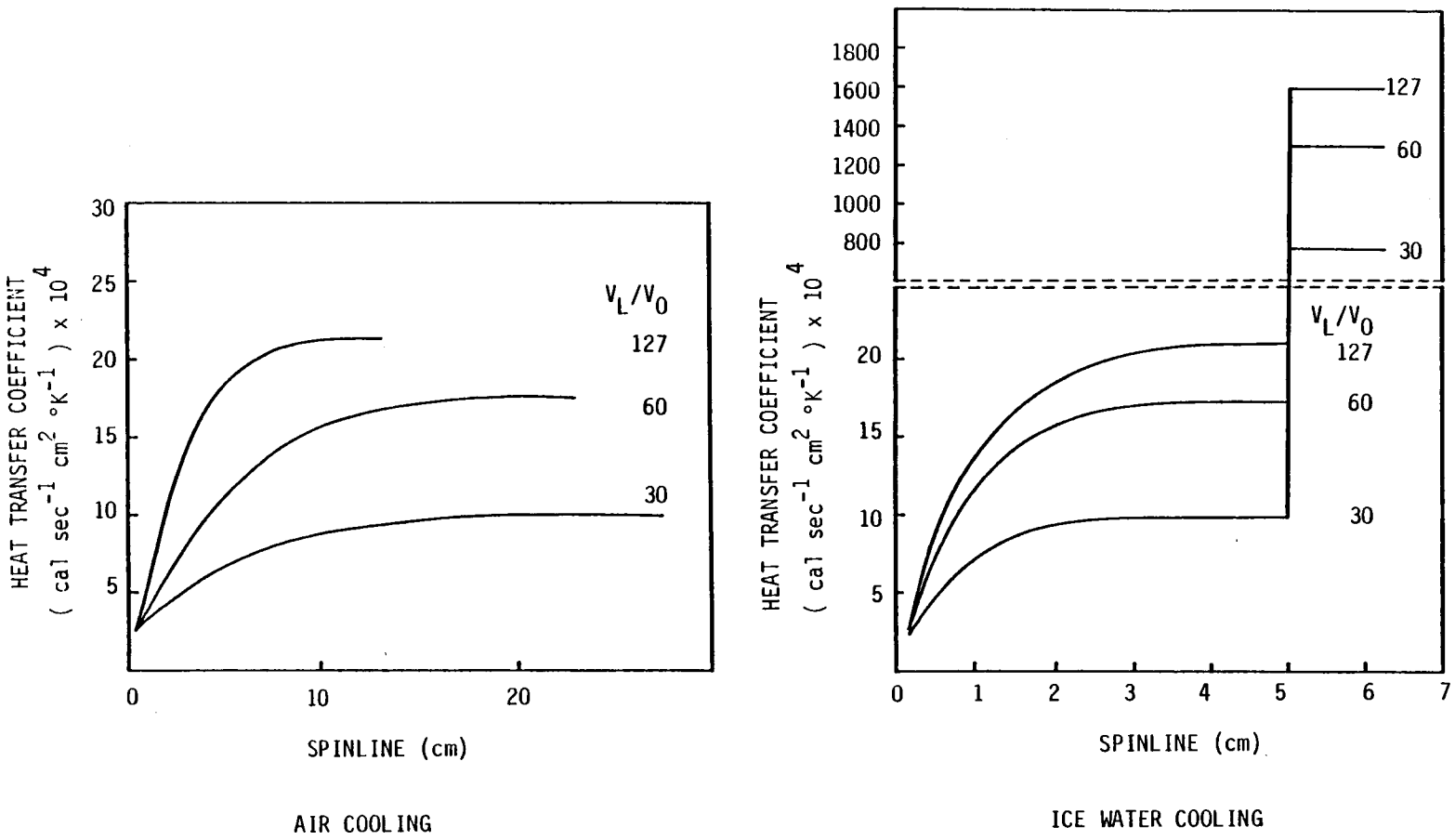


Figure V-7. Predicted heat transfer coefficient profile along the spinline for PS fibers.

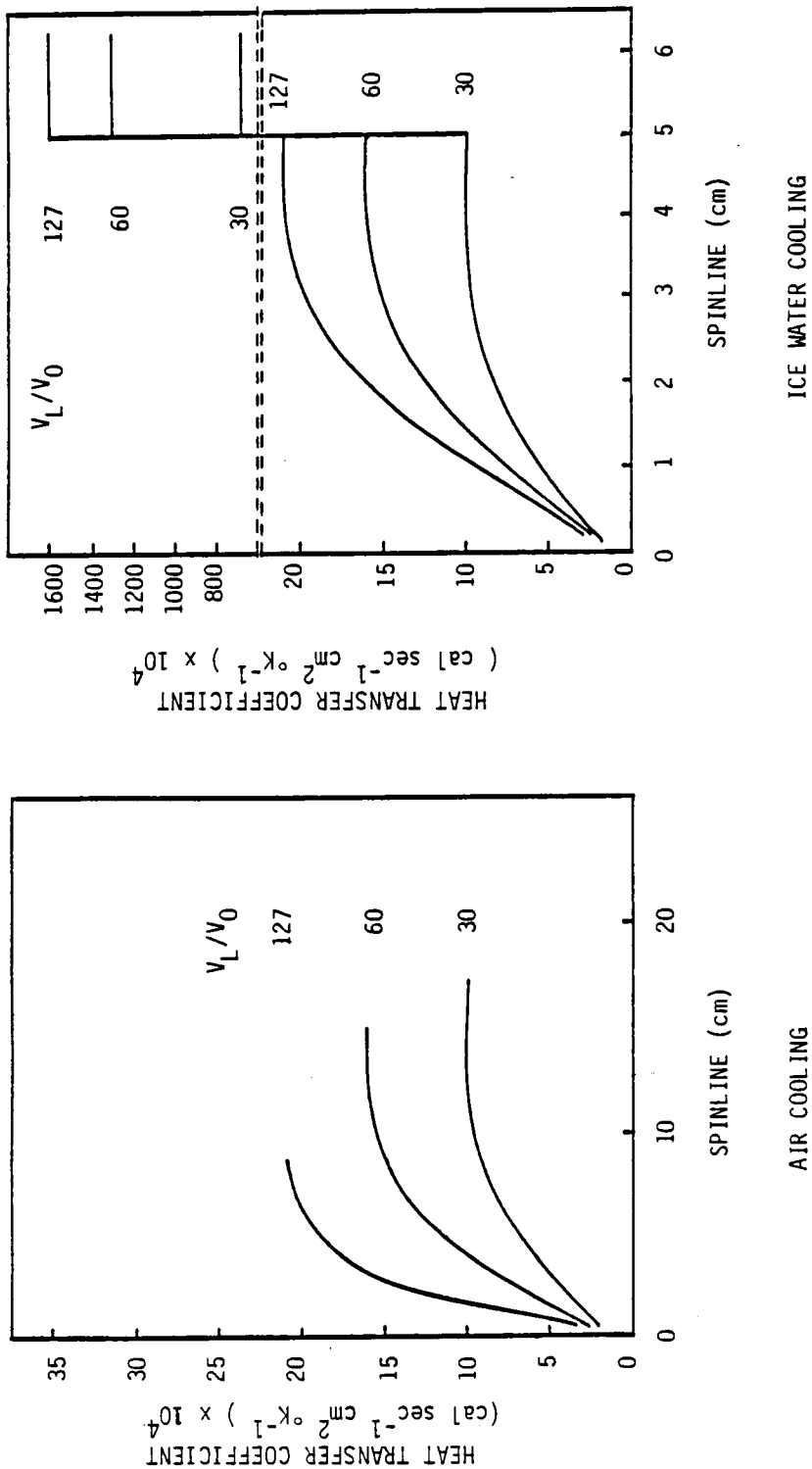


Figure V-8. Predicted heat transfer coefficient profile along the spinline for PC fibers.

Fourier's law of heat conduction allows us to predict the temperature distribution. This has the form

$$\rho C_p v\left(\frac{\partial T}{\partial x}\right) = \frac{1}{r}\frac{\partial}{\partial r}\left(K \frac{\partial T}{\partial r}\right) \qquad [5\text{-}6]$$

with boundary and initial conditions

$$T(r, 0) - T_0 \quad , \quad \frac{\partial T(0, t)}{\partial r} = 0$$

$$-K \frac{\partial T}{\partial r}(R, T) = h(T(R, t) - T_s) \ .$$

Carslaw (7) and Andrews (22) computed the temperature profile analytically by using Bessel functions.

$$\frac{T - T_s}{T_0 - T_s} = \sum_n^{\infty} \frac{2 N_{nu} J_0(\beta_n \frac{r}{R})}{(\beta_n{}^2 + N_{nu}{}^2) T_0(\beta_n)} \exp(\beta_b F_{fo} \qquad [5\text{-}7]$$

Constant diameter was used in their calculation. We attempt to calculate temperature distribution using their approach with predicted diameter and heat transfer coefficient profiles along the spinline. This temperature distribution leads to a stress distribution since the elongational viscosity varies with temperature across the fiber diameter. Finally we obtained the birefringence distribution across the diameter direction which has the form

$$\Delta n(r) = C \sigma_{11}(r) \ . \qquad [5\text{-}8]$$

Calculation was provided from the CALTEM program which was made based on Equation [5-7]. By using variable separation method with boundary conditions Equation [5-7] was obtained from partial differential Equation [5-6]. To solve Equation [5-7] Bessel functions must be known. We used the approximated functions which have forms

$$J_0(x) = 1 - \frac{x^2}{2^2(1!)^1} + \frac{x^4}{2^4(2!)^2} - \frac{x^6}{2^6(3!)^2} + \ldots \qquad [5\text{-}9a]$$

$$J_1(x) = \frac{x}{2} - \frac{x^3)}{2^3\ 1!\ 2!} + \frac{x^5}{2^5\ 2!\ 3!} - \ldots \qquad [5\text{-}9b]$$

to calculate Bessel functions of the first kind. The β_n in Equation [5-7] which are the roots of

$$\beta_n \frac{J_1(\beta_n)}{J_0(\beta_n)} = N_{nu} = \frac{hR}{k} \qquad [5\text{-}10]$$

were obtained from the program CALRO with different Nusselt's number along the spinline. Nusselt's number profiles were obtained from the SPIN program which can provide the radius profiles and heat transfer profile.

5.2.2. Results and Discussion

Calculated tension and experimental stress optical coefficient were used in the calculation of mean birefringence. Experimental results, theoretical results and a best fit ($C^* = \frac{\Delta\bar{n}}{\sigma}$) were plotted

in Figures V-9 and V-10 for polycarbonate and polystyrene fibers. The calculated tension was obtained from the spinning dynamics analysis. Stress optical coefficient was chosen as 3500 Brewster for polystyrene and 5500 Brewster for polycarbonate.

Results show a quite linear relationship between V_L/V_0 and Δn. However in the high stress region, some deviations were found when we used experimental stress optical coefficient. It seems that our experimental values are lower than the prediction. A best fit of the experimental birefringence data are obtained by taking C as 4700 for polystyrene and 6200 for polycarbonate. These results are not unreasonable.

In our analysis we again use Oda et al.'s hypothesis. We proceeded by using Equations [5-11] and [5-12].

$$\Delta n(r) = C\,\sigma_{11}(r) = C\quad \chi(r)\,\frac{dv_1}{dx_1} \qquad [5\text{-}11a]$$

$$= C\,A\,e^{E/RT(r)}\,\frac{dv_1}{dx_1} \qquad [5\text{-}11b]$$

$$\overline{\Delta n} = \frac{C}{\pi R^2}\int_0^R 2\pi\, r\,\sigma_{11}\,d\gamma\ . \qquad [5\text{-}12]$$

These may be combined to yield Equations [5-13] and [5-14] with Equation [5-7].

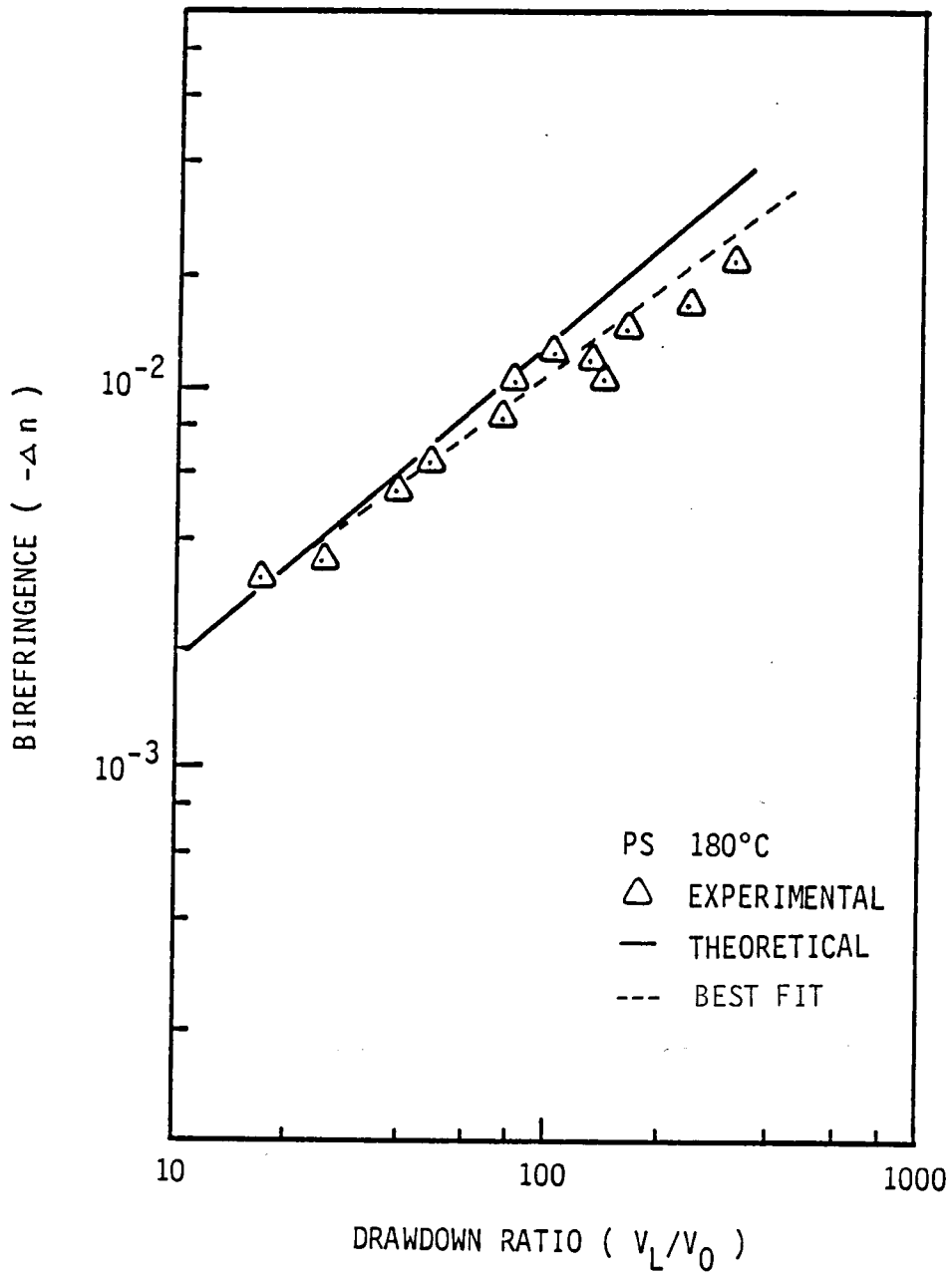


Figure V-9. Mean birefringence versus drawdown ratio for polystyrene fibers.

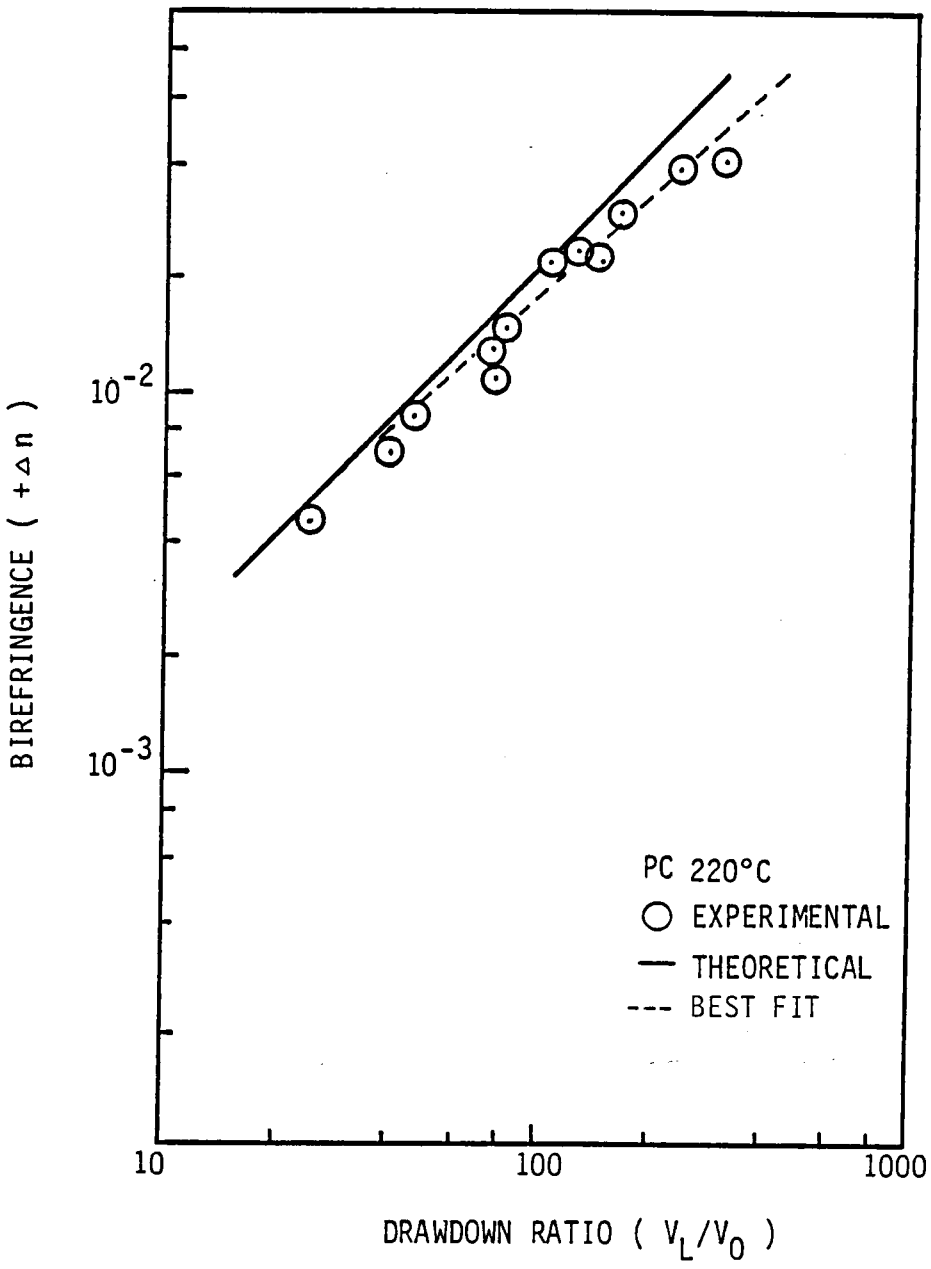


Figure V-10. Mean birefringence versus drawdown ratio for polycarbonate fibers.

$$\frac{\Delta n(r)}{\Delta \bar{n}} = \pi R^2 \frac{\sigma_{11}(r)}{\int_0^R 2\pi r \sigma_{11} d\gamma} = \frac{\pi R^2 \chi(r) \frac{dv_1}{dx_1}}{\left[\int_0^R 2\pi r \chi d\gamma\right] \frac{dv_1}{dx_1}} \qquad [5\text{-}13]$$

$$= \frac{\chi(r)}{\bar{\chi}}$$

$$= \frac{e^{E/RT(r)}}{e^{E/R\bar{T}}} \qquad [5\text{-}14]$$

We have based the calculation on using these two equations.

Figures V-11 and V-12 show the comparison between experimental value and predicted values and reasonable agreement was obtained. Pronounced profiles are predicted in severe cooling because of high heat transfer coefficients. Generally experimental data indicated more pronounced profiles than the predicted values. The reasons for this are not clear. They may indicate either experimental error which exists in the wedge method or problems in the theoretical solution equation errors in heat transfer coefficients.

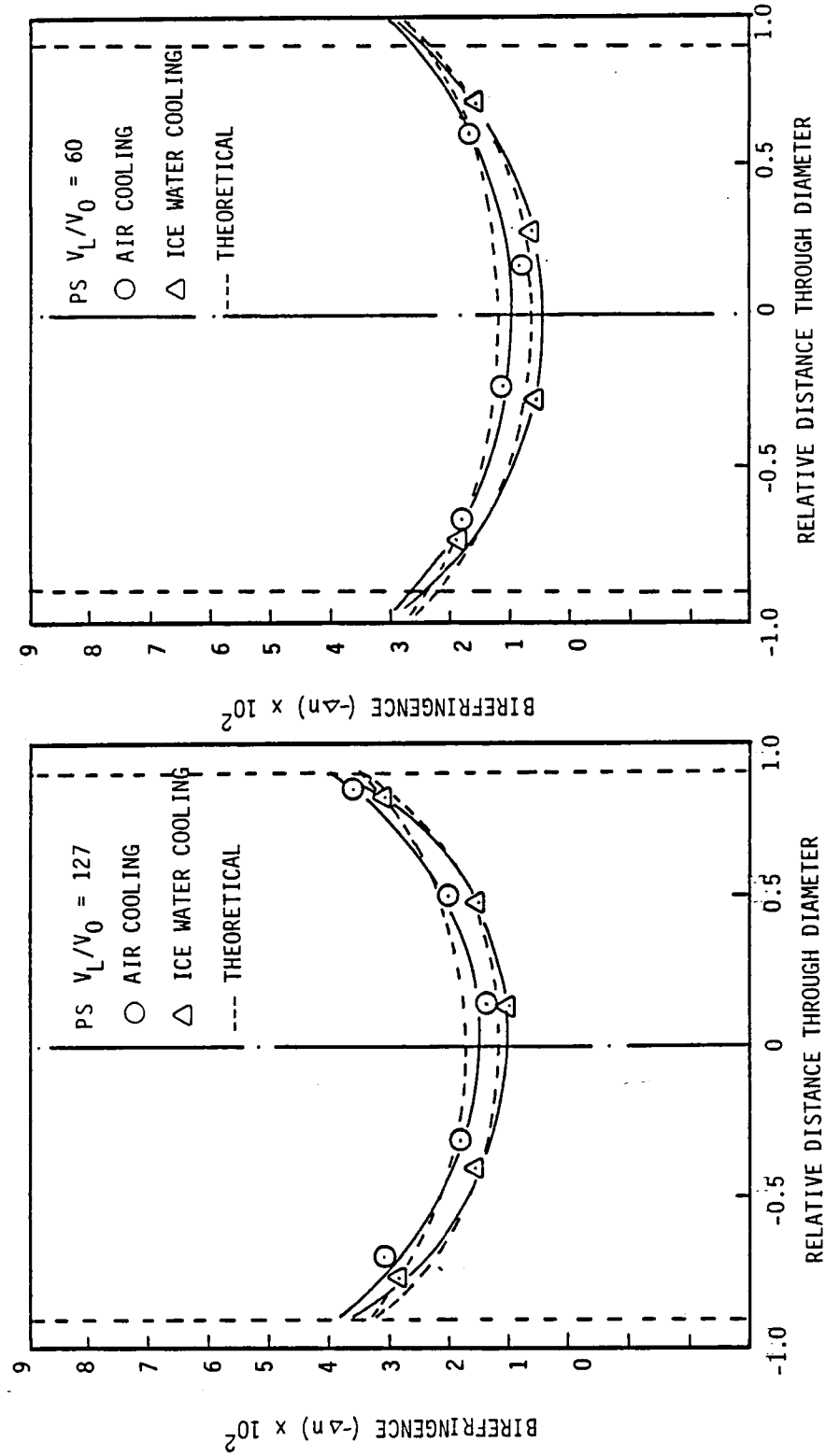


Figure V-11. Orientation distribution for polystyrene fibers.

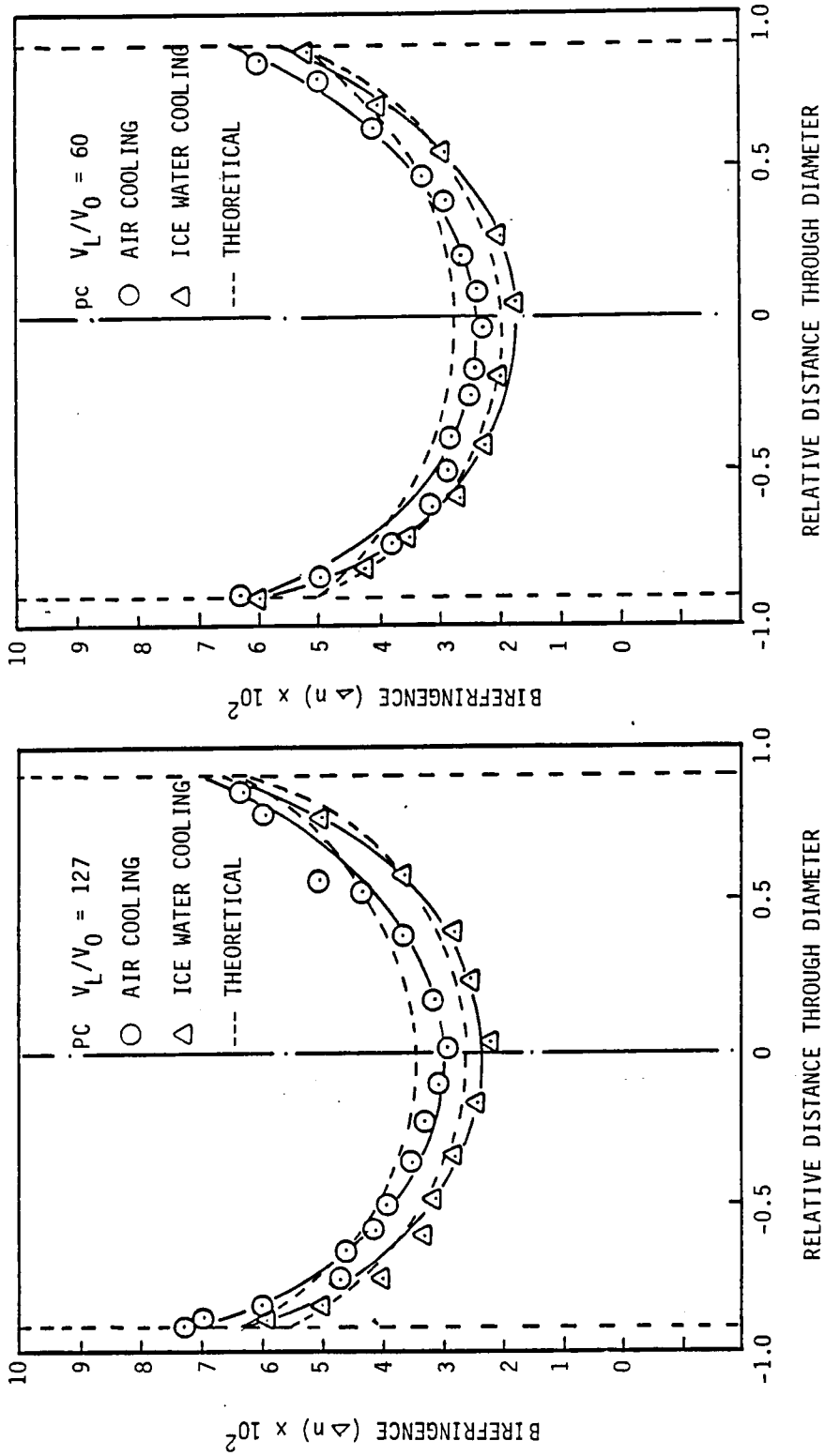


Figure V-12. Orientation distribution for polycarbonate fibers.

CHAPTER VI

CRYSTALLIZATION OF A POLYCARBONATE

6.1. INTRODUCTION

In our study of orientation polycarbonate fibers, we have found that the birefringence behavior of polycarbonate fibers is not the same as that of polystyrene fibers (see Figure IV-9, p. 75). The slopes of the two materials in Figure IV-9 should be the same. However, some deviation was found between the two materials. This is examined in Figure VI-1. In this chapter we examine the problem by crystallization of polycarbonate fibers. We also investigate crystallization of polycarbonate films which were made by two different techniques.

It has been known that polycarbonate is not a complete amorphous material since Prietzschk (126) examined the bisophenol A polycarbonate using x-ray. Most intensive studies on the thermal behavior of polycarbonate have been made by Peilstocker (123). He has stated that it is possible to cause crystallization in polycarbonate in the temperature range between 150°C and about 220°C. The crystallization proceeds most quickly at 190°C. However, a day is necessary for the first crystallites to develop and a week or more to obtain a crystalline material which has a well developed spherulitic structure. Since it takes a long time to crystallize material, degradation can occur during heating.

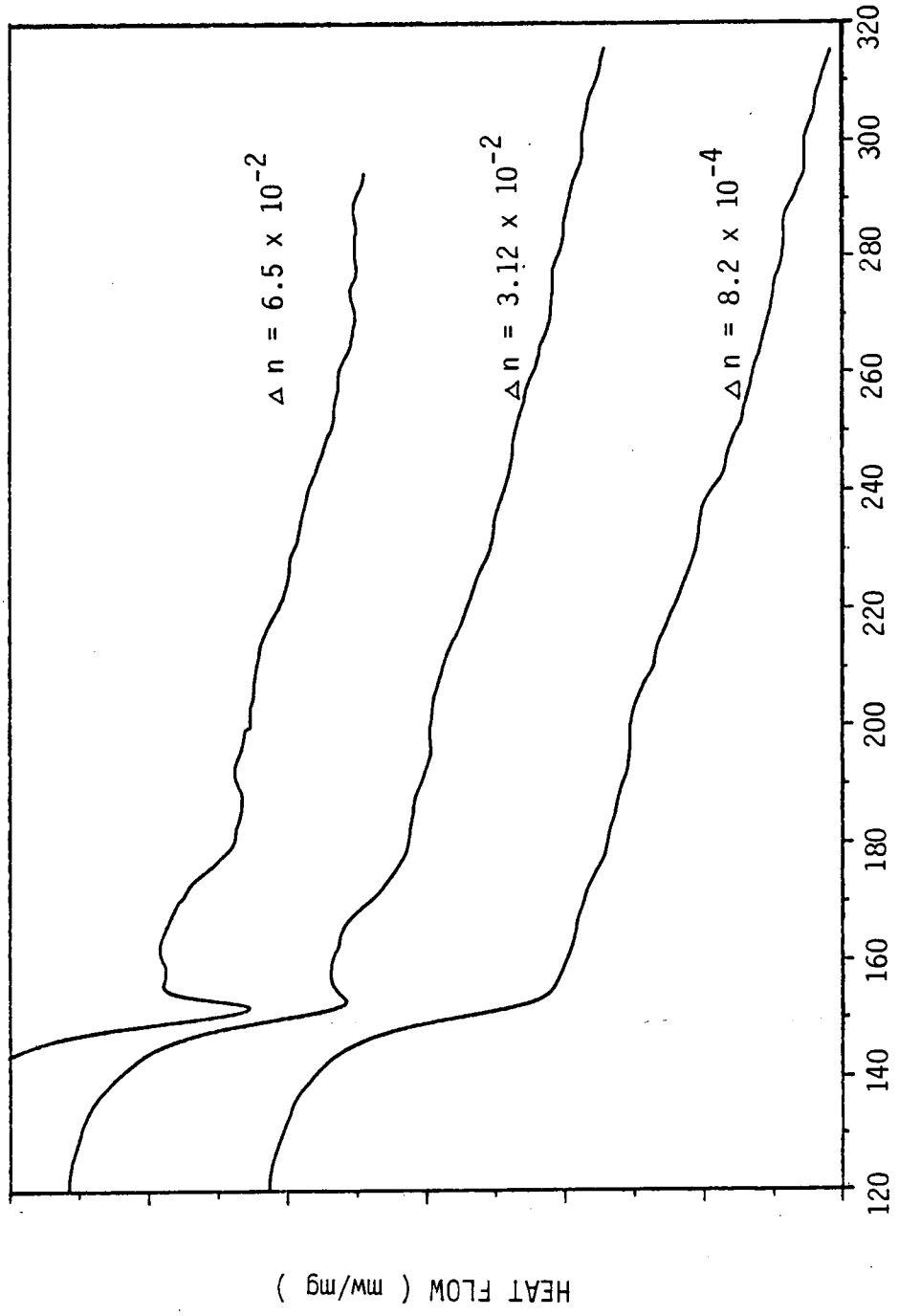


Figure VI-1. DSC results for polycarbonate fibers.

In order to avoid this degradation problem, solvent induced crystallization was introduced by Sheldon and Blakey (139). They found acetone increased the rate of crystallization. Several investigators (82, 101, 62) have since studied the crystallization of polycarbonate by means of partial solvent swelling. They found this method is effective for polycarbonate.

Recently Conix and Jeurissen (28) proposed the use of plasticizers. Gallez, Legaras and Mercier (50) investigated the action of plasticizers on the crystallization of bisophenol A polycarbonate. They found the plasticizers such as trimellitic acid and tridecyloctyl ester can promote crystallization rates.

Few investigators have studied stress induced crystallization. Considerably higher drawdown ratio and a greater degree of orientation may induce crystallization. Reichle and Wilsing (128) and Falkai and Hinrichsen (42) have found hot drawn polycarbonate fibers in a temperature range above the second order transition temperature and below the melting point have a high tenacity and elastic modulus. It is not known if this is associated.

6.2. RESULTS

It was found that polycarbonate films which have different thermal histories have quite different crystallinity. Figure VI-2 shows the DSC scanning for those films. It seems that crystallinity increases with increasing heat treated time.

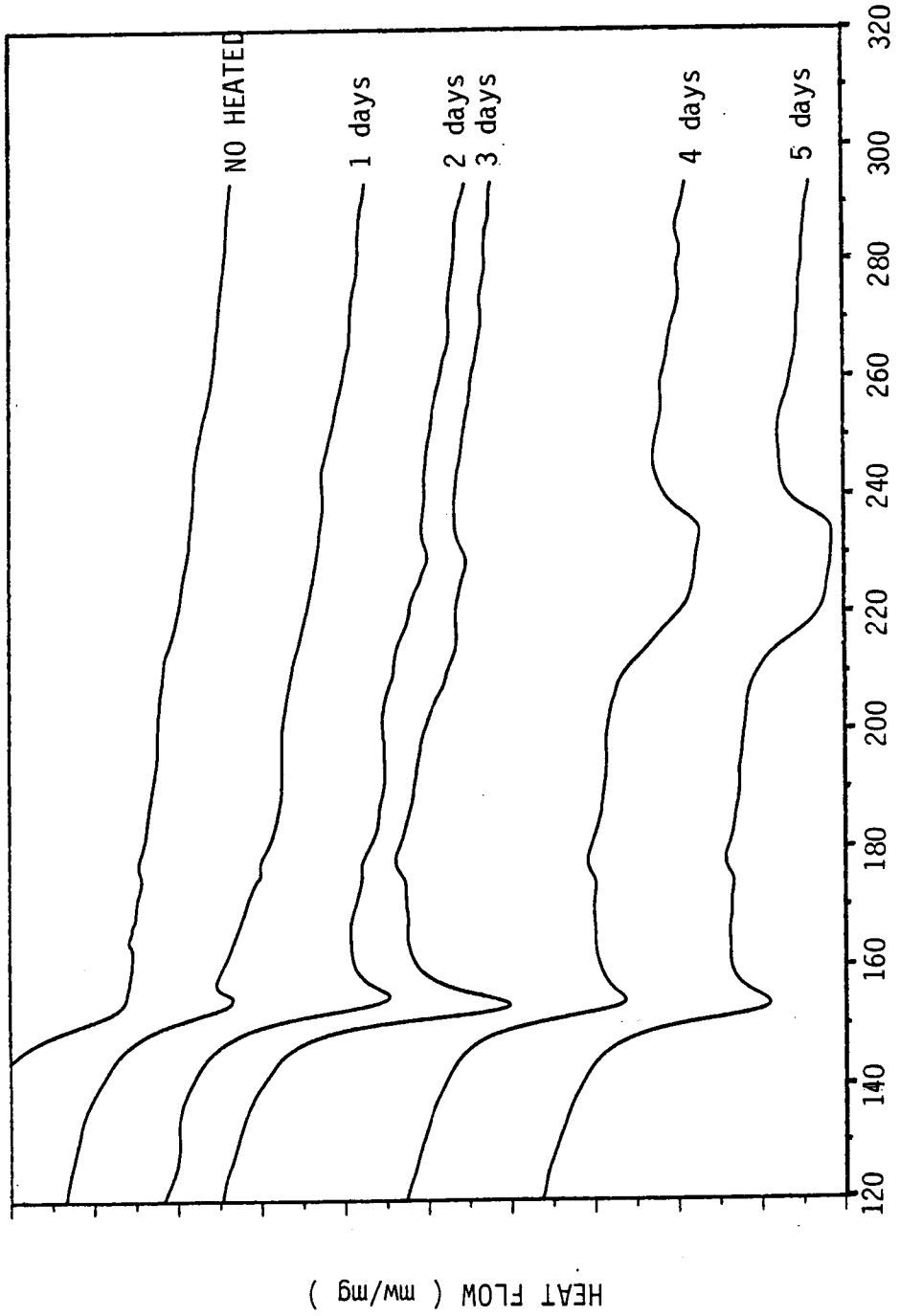


Figure VI-2. DSC results for heat treated polycarbonate films at 175°C.

Figure VI-3 shows a DSC scanning for partially swollen polycarbonate in acetone. The crystallinity increased significantly compared to thermally crystallized polycarbonate film. It also found that crystallinity continuously increased by heat treatment after crystallization due to partial swelling.

Three different fibers which have different orientation were examined (see Figure VI-1). Small amounts of crystallinity were noted compared to crystallized polycarbonate films. However, it is clear that each fiber has different crystallinity depending on the degree of orientation.

The results obtained from three different crystallizations were summarized in Table VI-1. It shows the changes of transient temperature, melting range, heat of fusion and crystallinity in each sample.

6.3. DISCUSSION

Our main concern in this chapter is why the relationship between birefringence and stresses in polycarbonate fibers is different from that of amorphous material. It is well known that birefringence is not only the function of orientation but also the function of crystallinity. According to our results (see Figure VI-1) the highly oriented fibers have some crystallinity even though the amount is small. On the other hand, there is no crystallinity in low oriented fibers. Thus it is concluded that the deviation of the slope in high stress level is due to the crystallinity in fibers.

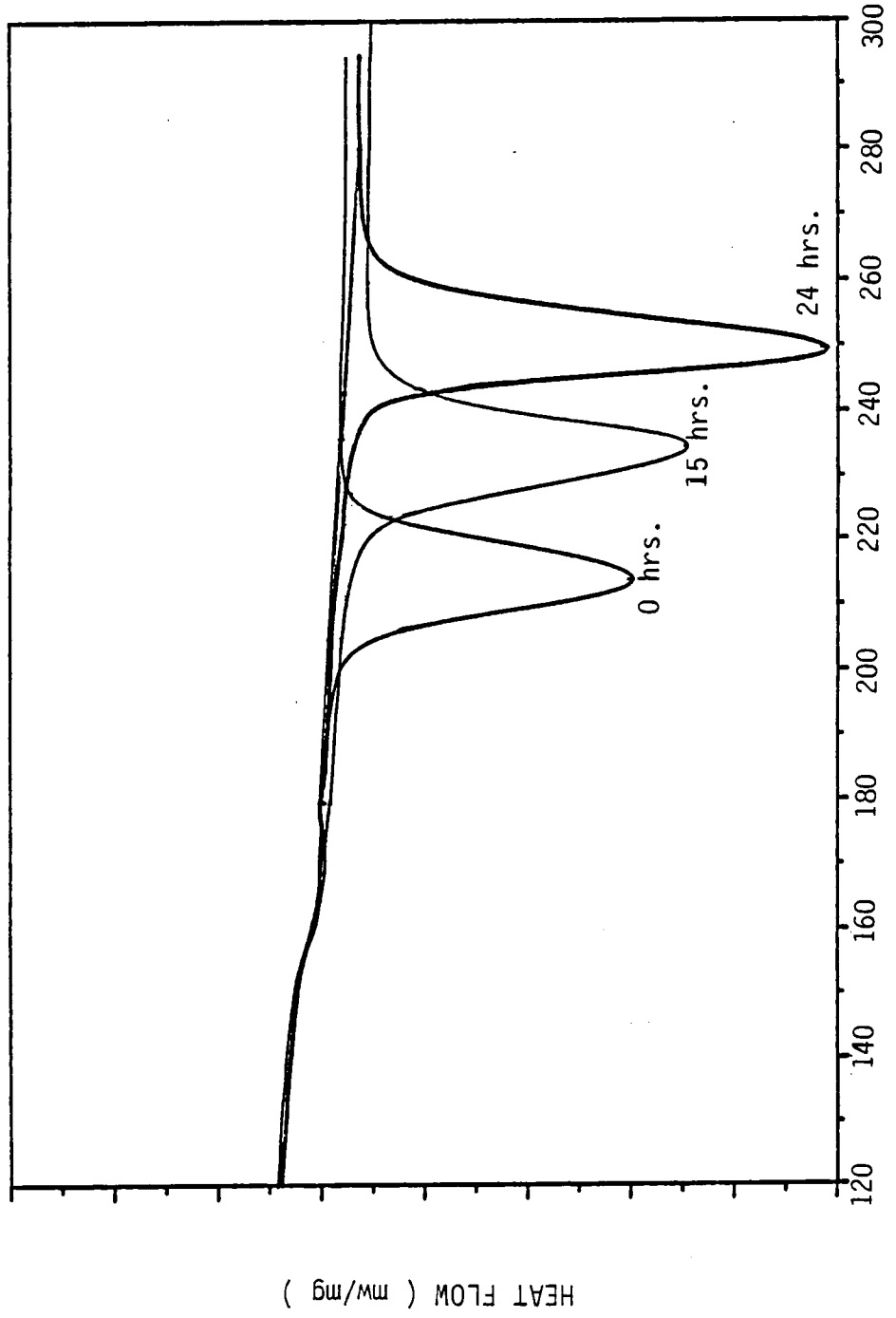


Figure VI-3. DSC results for acetone treated polycarbonate films (3 days acetone treated).

Table VI-1. Crystallinity and melting range of polycarbonate in different crystallization procedures.

	Orientation	T_g (°C)	T_m (°C)	ΔH_f(J/g)	X (%)
PC Film (Quenched)	-	153	-	-	-
PC Fiber (260°C, V_L/V_0=40)	8.2×10^{-4}	153	-	-	-
PC Fiber (220°C, V_L/V_0=165)	3.12×10^{-2}	153	160-231	0.85	1.6
PC Fiber (210°C, V_L/V_0=246)	6.5×10^{-2}	153	164-242	1.04	2.0
PC Film (2 Days heated)	-	156	180-245	0.80	1.5
PC Film (3 Days heated)	-	156	180-245	1.40	2.7
PC Film (5 Days heated)	-	156	180-250	3.08	5.9
PC Film (Acetone, 0 hrs. heated)	-	163	180-240	22.69	43.0
PC Film (Acetone, 15 hrs. heated)	-	163	180-260	25.93	49.6
PC Film (Acetone, 24 hrs. heated)	-	163	180-280	33.17	63.4

The only problem in our explanation is that the crystallinity in fiber is quite small. Thus it is necessary to make sure that heat flow change in DSC scanning is really due to the structure change in polycarbonate molecular chain. Therefore two additional experiments, thermal crystallization and partial swelling crystallization, were carried out. From Figures VI-2 and VI-3, we found some similarity when heat flow starts to change at 180°C. We also found melt enthalpy and the maximum melting temperature were increased depending on crystallization conditions. Thus we can deduce from these results that the maximum melting temperature can be decreased in less favorable crystallization condition such as stress induced crystallization.

In summary, polycarbonate fibers can be crystallized when they are spun with high stress. Consequently orientation is increased due to this crystallization.

CHAPTER VII

FIBRILLATION IN MELT SPUN POLYSTYRENE AND POLYCARBONATE FIBERS

7.1. INTRODUCTION

In this chapter we have sought to investigate fibrillation in our melt spun polystyrene and polycarbonate fibers. To investigate potential fibrillar structure a peeling technique (155, 138) was introduced by Scott (138). Each type of fiber has characteristic peeling behavior which can be affected by changes in structure. Another approach to characterizing fibrillar structure is small angle scattering of x-ray (SAXS). Statton (149) found that SAXS diagrams of fibers are characterized by two types of scattering: discrete scattering and diffuse scattering. Discrete diffraction at small angles is due to some periodicity in electron density of fibers. Diffuse scattering has a maximum intensity at an angle of 0° and decreases in intensity out to 1-2°. It is due to the inhomogeneities of electron density. Statton concluded that much diffuse scattering in fibers due to microvoids developed during solvent spinning (59) or drawing processes. There are many studies which deal with the drawn (30, 132, 149, 44), twisted and heat set (34, 51) fibers. Our experiments involved two powerful methods: scanning electron microscopy (SEM) and small angle x-ray scattering (SAXS).

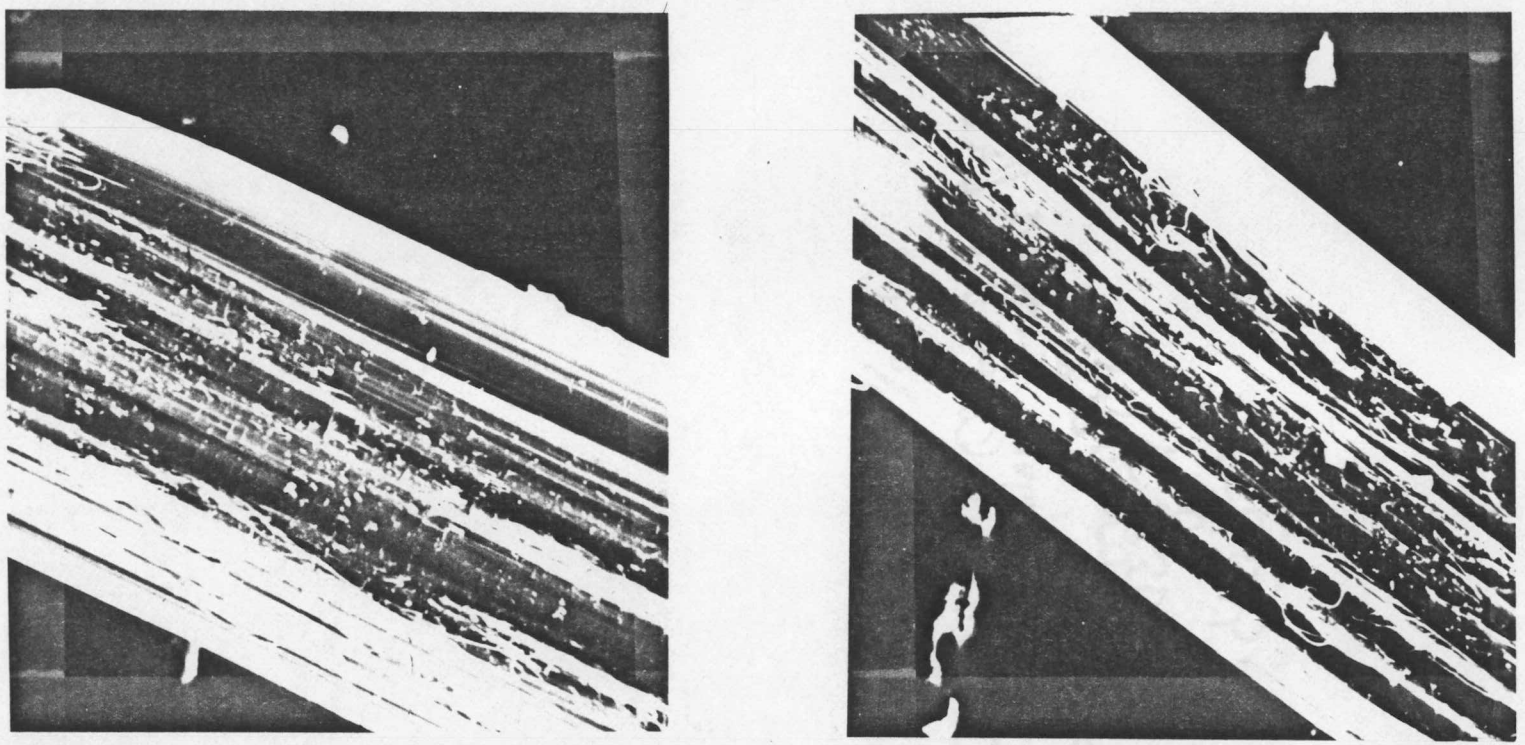
7.2. RESULTS

Fibrillar structures were found using SEM in peeled highly oriented polystyrene and polycarbonate fibers. The SEM results suggest that highly oriented polystyrene and polycarbonate fibers have fibrillated structures in which fibrils are parallel to the fiber axis (see Figures VII-1 and VII-2). However, fibers with lower orientation do not clearly show fibrillated structures (see Figure VII-3). Furthermore, peeling is impossible at lower orientation levels. It was also found that fibrillated structure is related to quenching conditions. Ice water quenching gave generally uniform fibrillated structures while the air cooling does not. We have also looked at other materials. The melt spun hydroxpropyl cellulose (HPC) and cellulose acetate butyrate (CAB) fibers were supplied by J. Chen. Figure VII-4 shows fibrillated structure in HPC fibers. The CAB fiber may be peeled but does not seem to have an apparently fibrillated structure.

Diffuse scattering patterns were obtained from SAXS. Maximum intensities shown at 0° and then decrease with increasing angle (see Figure VII-5). The HPC fiber exhibits much more intense SAXS scattering.

7.3. DISCUSSION

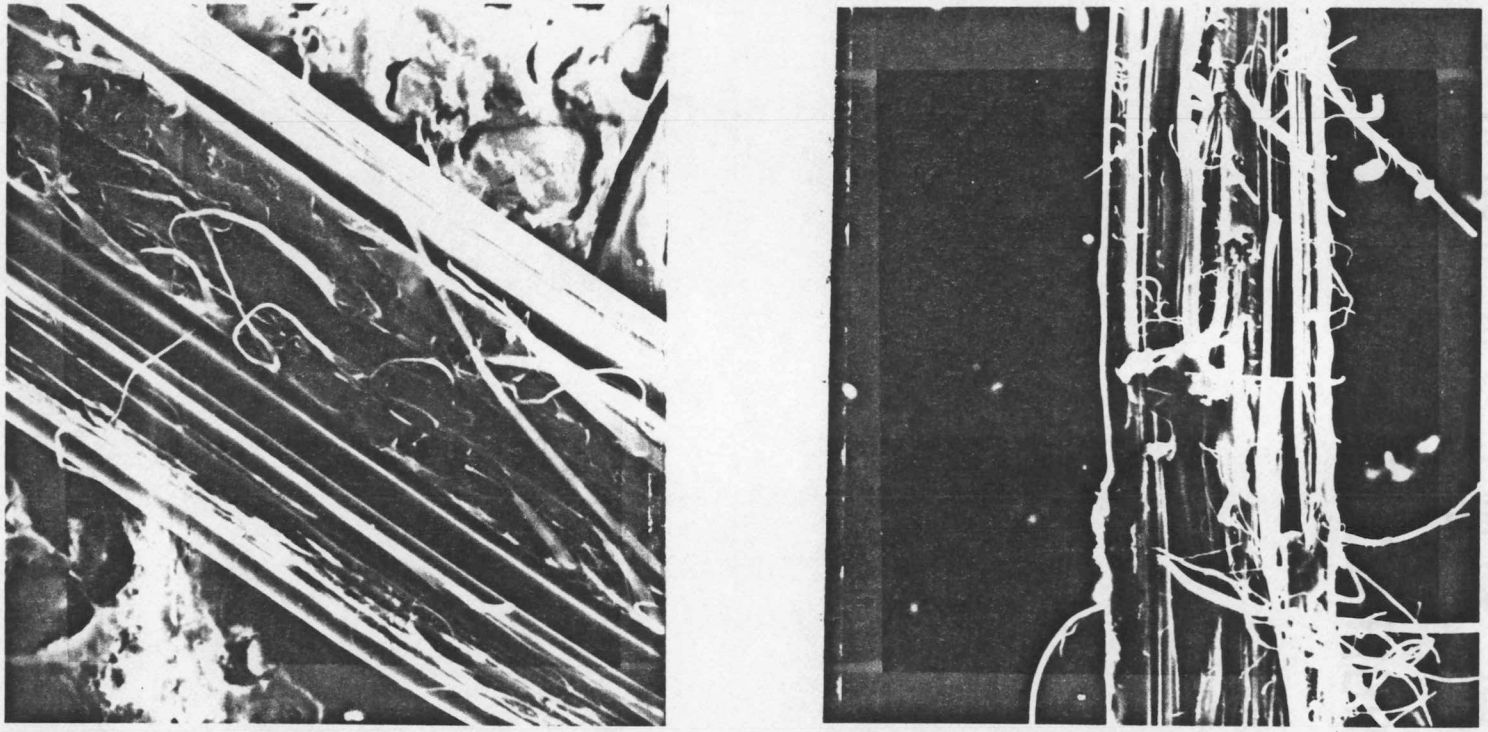
Fibrillated structures in amorphous melt spun fiber have not been described previously. The results are striking and unexpected. They are certainly associated with the orientation but its absolute



(a) (b)

Figure VII-1. SEM photomicrographs of peeled polystyrene fibers.

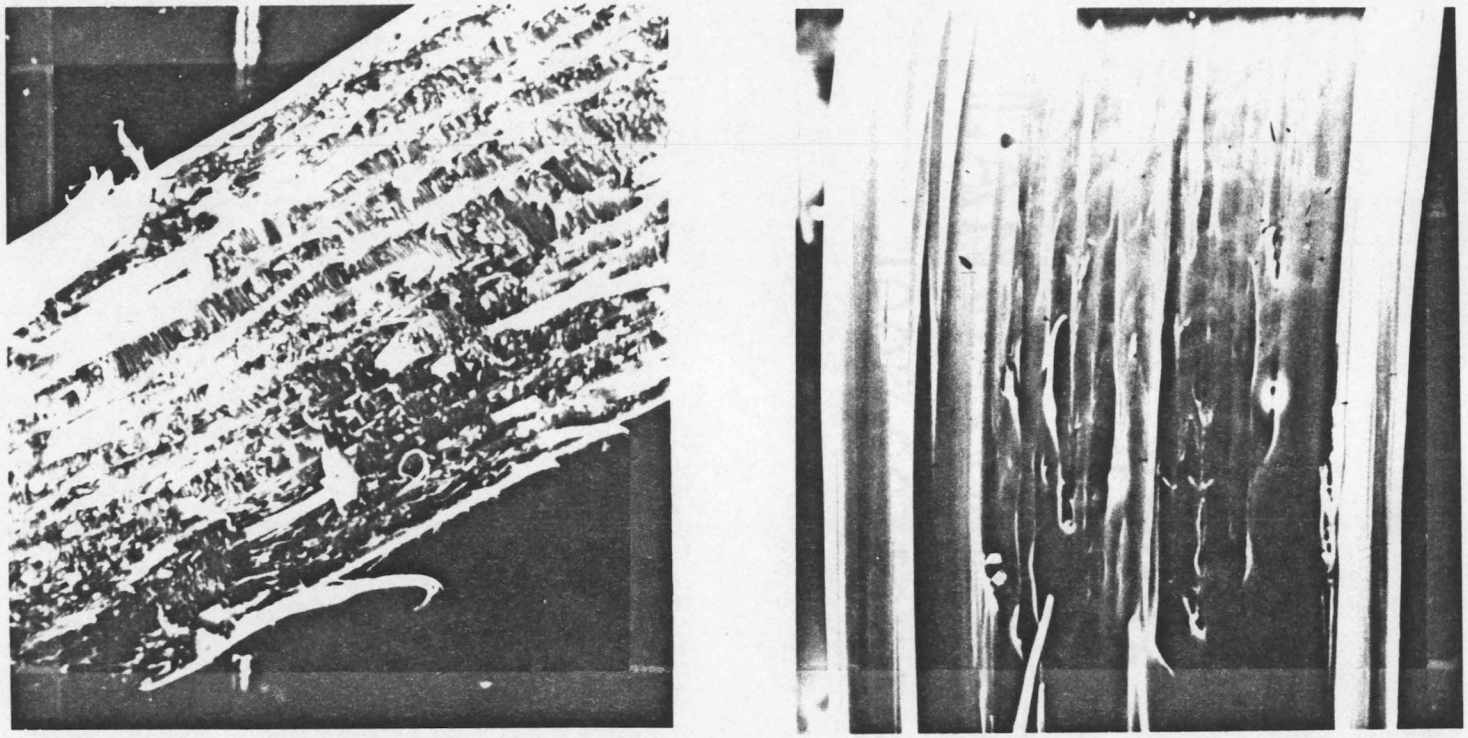
(a) Air cooling $-\Delta n = 2.9 \times 10^{-2}$ (200x)
(b) Ice water cooling $-\Delta n = 2.8 \times 10^{-2}$ (100x)



(a) (b)

Figure VII-2. SEM photomicrographs of peeled polycarbonate fibers.

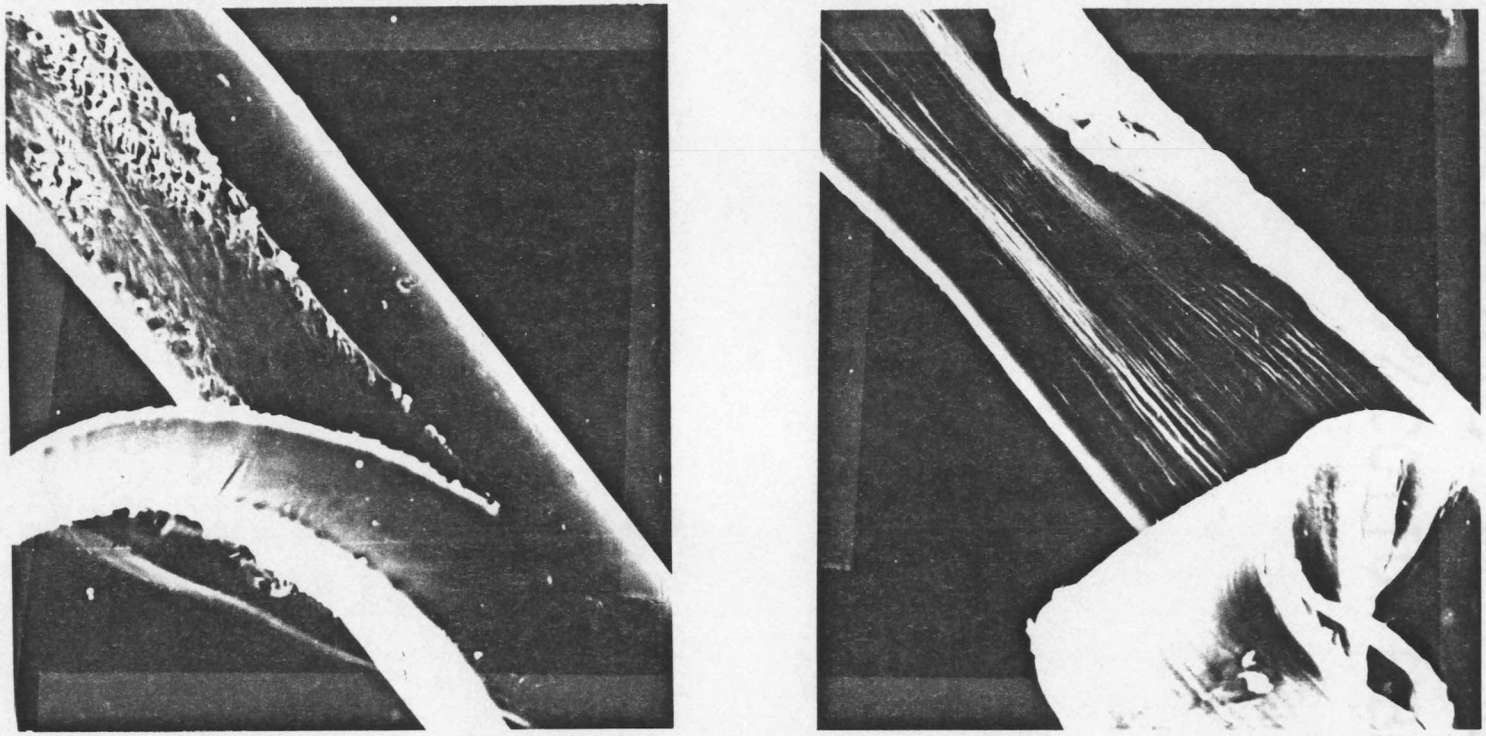
(a) Air cooling $\Delta n = 2.9 \times 10^{-2}$ (200x)
(b) Ice water cooling $\Delta n = 2.8 \times 10^{-2}$ (100x)



(a) (b)

Figure VII-3. SEM photomicrographs of peeled PS and PC fibers.

(a) PS Air cooling - $\Delta n = 9 \times 10^{-3}$ (100x)
(b) PC Ice water cooling $\Delta n = 1.0 \times 10^{-2}$ (100x)



(a) (b)

Figure VII-4. SEM photomicrographs of peeled fibers.

(a) HPC fiber $\Delta n = 1.3 \times 10^{-2}$
(b) CAB fiber $\Delta n = 3.8 \times 10^{-3}$

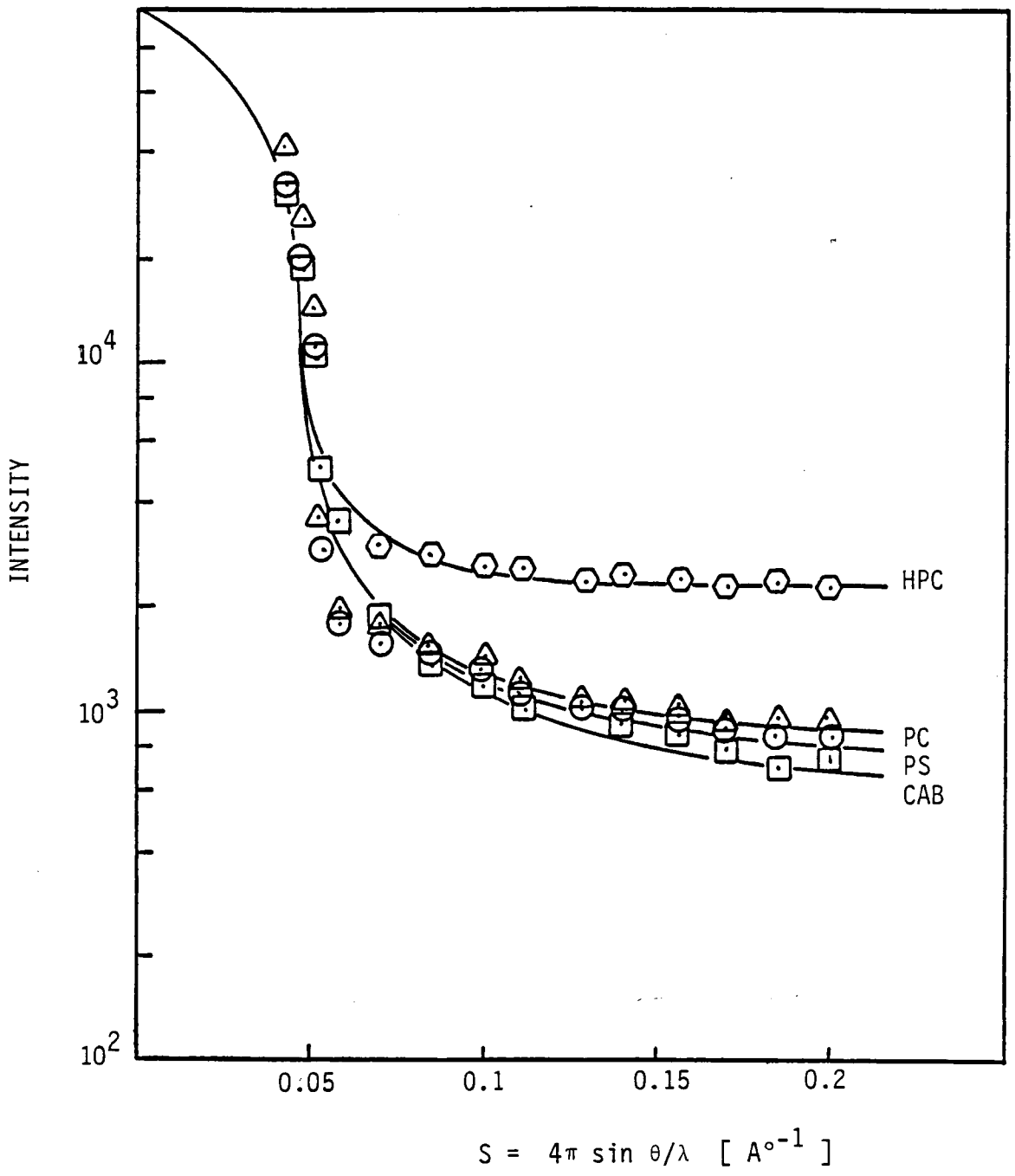


Figure VII-5. SAXS patterns for fibers (HPC, PC, PS, CAB).

level is low. Ther Hermans orientation factors are no more than about 0.1. Relatively the transverse direction orientation gets weaker.

The residual stresses caused by the quenching of the filament may induce this fibrillation. The magnitude of residual stresses varies with cooling conditions becoming more severe in severely quenched systems. High residual stresses could lead to fibrillated structures. Thus ice water cooling gives more fibrillated structures than air cooling.

To evaluate the fibrillar structure in more detail SAXS experiments were carried out. We expected diffuse equatorial scattering. Figure VII-5 shows only significant scattering in HPC but not in the PS or PC. The reason is unknown. Perhaps the void structures are too large to be detected.

In summary, we quantitatively found fibrillar structures in melt spun relatively highly oriented polycarbonate and polystyrene fibers. We also observed cooling effects on the fibrillar structures. We may conclude that those phenomena are due to the high level of orientation and perhaps residual stresses. However, more quantitative analysis is needed to develop this idea.

CHAPTER VIII

ESTIMATION OF THERMAL QUENCH STRESSES IN MELT SPUN FIBERS

8.1. APPROACH

In this chapter we will seek to estimate the magnitude of the thermal quench stresses in melt spun fibers. Residual stresses (thermal quench stresses) in thick fibers were calculated using O'Rourke and Saenz's (120) approach. They stated the existence of a state of ease at a temperature T^*, such that for a temperature $T > T^*$, all stresses in the body are negligibly small compared to the stresses for $T << T^*$. They also neglect the temperature variation of the "elastic" and "thermal" constants. To calculate the residual stresses in a body (A) quenched from the initial temperature T_1 to the temperature T_0 of cooling media ($T_1 > T_0$), one calculates the transient thermal stresses at time $t = t^*$ ($T = T^*$) in an elastic body (B) with the same elastic and thermal constant (A) whose initial temperature is T_1 and whose surface beginning at $t = 0$ is maintained at T_1. The stresses in (B) at $t = t^*$ are the negative of the residual stresses at $t \to \infty$ in (A). We now use this approach to calculate the residual stresses in melt spun fibers as equivalent to those in a quenched cylinder.

For a long cylinder, the transient thermal stresses are expressed as:

$$\sigma_{rr} = \frac{\alpha E}{1 - \nu} \left[\frac{1}{R^2} \int_0^b \theta r dr - \frac{1}{r^2} \int_0^r \theta r dr\right] \qquad [8\text{-}1a]$$

$$\sigma_{\theta\theta} = \frac{\alpha E}{1 - \nu} \left[\frac{1}{R^2} \int_0^b \theta r dr + \frac{1}{r^2} \int_0^r \theta r dr - \theta\right] \qquad [8\text{-}1b]$$

$$\sigma_{zz} = \frac{\alpha E}{1 - \nu} \left[\frac{2\nu}{R^2} \int_0^b \theta r dr - \theta\right] \qquad [8\text{-}1c]$$

where α is volumetric thermal expansion coefficient, E is Young's modulus, ν is Poisson's ratio, R is radius of fiber and θ is the temperature profile across the radius direction.

A fiber which has a known axially symmetric distribution of temperature and which is suddenly placed in contact with a convection fluid of constant temperature is considered. The boundary conditions are

$$\begin{aligned} t &= 0 \qquad & \theta &= f(r) \\ t &\quad 0 \qquad & \frac{\partial\theta}{\partial r} &= \frac{h}{k}\,\theta \end{aligned} \qquad [8\text{-}2]$$

where h is heat transfer coefficient and k is conductivity. This led to a solution of the heat conduction equation of the form:

$$\theta = 2Rh\ f(r) \sum_{n=1}^{\infty} \frac{J_0(r\beta_n/R)}{(Rh^2 + \beta_n{}^2)J_0(\beta_n)}\, e^{-P_n t^*} \qquad [8\text{-}3]$$

where β_n are the roots of

$$\beta_n \frac{J_1(\beta_n)}{J_0(\beta_n)} = N_{nu}$$

$f(r)$ is known temperature distribution along the radius direction. Using Equations [8-1] and [8-3], the resulting classical thermal stress fields are

$$\frac{(1-\nu)\sigma_{rr}}{E\,\alpha\,f(r)} = \sum_{n=1}^{\infty} \frac{2Rh\, e^{-k\beta_n^2 t/R^2\rho C_p}}{\beta_n(R^2h^2+\beta_n^2)J_0(\beta_n)} \left(J_1(\beta_n) - \frac{R}{r} J_1\left(\frac{r}{R}\beta_n\right)\right) \qquad [8\text{-}4a]$$

$$\frac{(1-\nu)\sigma_{\theta\theta}}{E\,\alpha\,f(r)} = \sum_{n=1}^{\infty} \frac{2Rh\, e^{-k\beta_n^2 t/R^2\rho C_p}}{\beta_n(R^2h^2+\beta_n^2)J_0(\beta_n)}$$

$$\left(J_1(\beta_n) + \frac{R}{r} J_1\left(\frac{r}{R}\beta_n\right) - J_0\left(\frac{r}{R}\beta_n\right)\right) \qquad [8\text{-}4b]$$

and if the resultant of the normal forces over the cross section of the fiber is zero

$$\sigma_{zz} = \sigma_{rr} + \sigma_{\theta\theta} \qquad [8\text{-}5]$$

According to O'Rourke and Sanenz the residual stresses are negative values of transient stresses at $t = t^*$ (solidification time). Thus, residual stresses are obtained in the form:

$$\sigma_{rr} = -\frac{E\,\alpha\,f(r)}{1-\nu} \sum_{n=1}^{\infty} \frac{2Rh\, e^{-k\beta_n^2 t^*/R^2\rho C_p}}{\beta_n(R^2h^2+\beta_n^2)J_0(\beta_n)} \left(J_1(\beta_n) - \frac{R}{r} J_1\left(\frac{r}{R}\beta_n\right)\right) \qquad [8\text{-}6a]$$

$$\sigma_{\theta\theta} = -\frac{E\,\alpha\,\theta_0}{1-\nu}\sum_{n=1}^{\infty}\frac{2Rh\,e^{-k\beta_n^2 t^*/R^2\rho C_p}}{\beta_n^2(R^2h^2+\beta_n^2)J_0(\beta_n)}$$

$$\left(J_1(\beta_n)+\frac{R}{r}J_1(\frac{r}{R}\beta_n)-J_0(\frac{r}{R}\beta_n)\right) . \qquad [8\text{-}6b]$$

In our analysis we neglect the influence of the deformation prehistory on the thermal stresses. The Young's modulus E, Poisson's ratio ν and volumetric thermal expansion coefficient which were used in this study are presented in Table VIII-1

Calculation of the residual stresses based on Equations [8-6a, 8-6b] has been carried out on the IBM computer with the computer programs as indicated in the Appendix. It is noted that properties of the material dramatically change at the transition temperature. As soon as the temperature is below T_g, it will rapidly solidify. Thus first we need to know how long the time elapsed from the beginning of quench to T_g. Equation [6-3] allows us to calculate the temperature profile when fiber surface is solidified. The solidification times along the radius direction were also calculated based on this equation. We input these values to program STRESS which was based on Equation [6-5] and calculate residual stress components σ_{rr} and $\sigma_{\theta\theta}$.

Figures VIII-1 and VIII-2 show the values of $(1-\nu)\sigma_r/E\alpha\theta_0$ and $(1-\nu)\sigma_\theta/E\alpha\theta_0$ with different dimensionless value $kt^*/R^2\rho C_p$. The Nusselt numbers are, respectively, 5 and 0.1. The result illustrates the influence of Nusselt number increase, that is, the quench becomes

Table VIII-1. Physical constants for PS and PC to calculate residual stresses.

	Unit	PS	PC
Young's Modulus	Pascal	3.4×10^{9}	2.5×10^{8}
Poisson's Ratio		0.325-0.333	0.38
Volumetric Thermal Expansion Coefficient	°K	$5.72\text{-}6.0 \times 10^{-4}$ ($T > T_g$)	2.0×10^{-4}
Thermal Diffusivity	cm^2/sec	7.5×10^{-4}	1.29×10^{-3}
Tensile Strength	Pascal	3.5×10^{7}	9×10^{7}

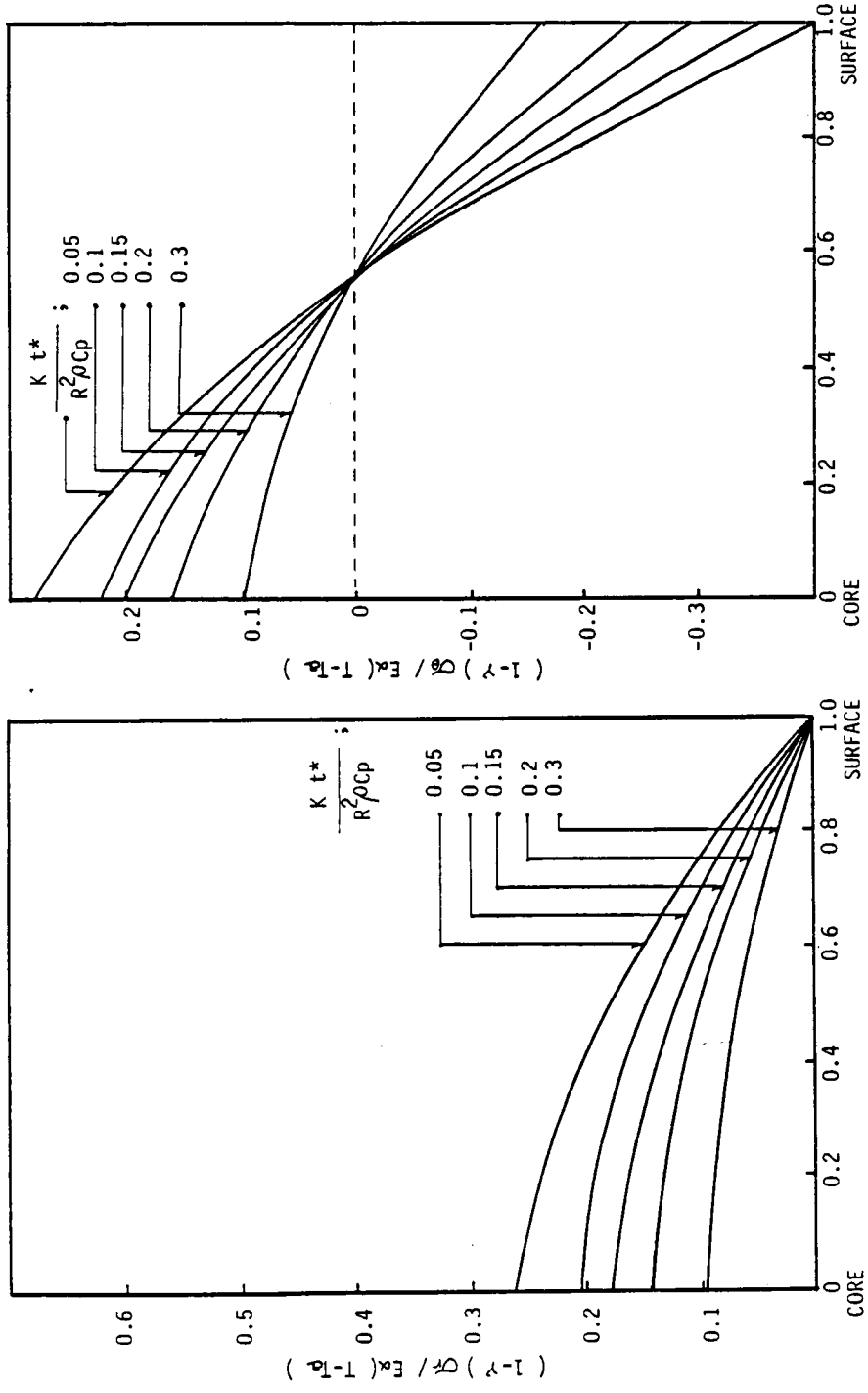


Figure VIII-1. Value of $(1 - \nu)\sigma_r/E\alpha(T - T_a)$ and $(1 - \nu)\sigma_\theta/E\alpha(T - T_a)$ as a function of $K\ t^*/R^2\rho C_p$ (Nusselt No. = 5).

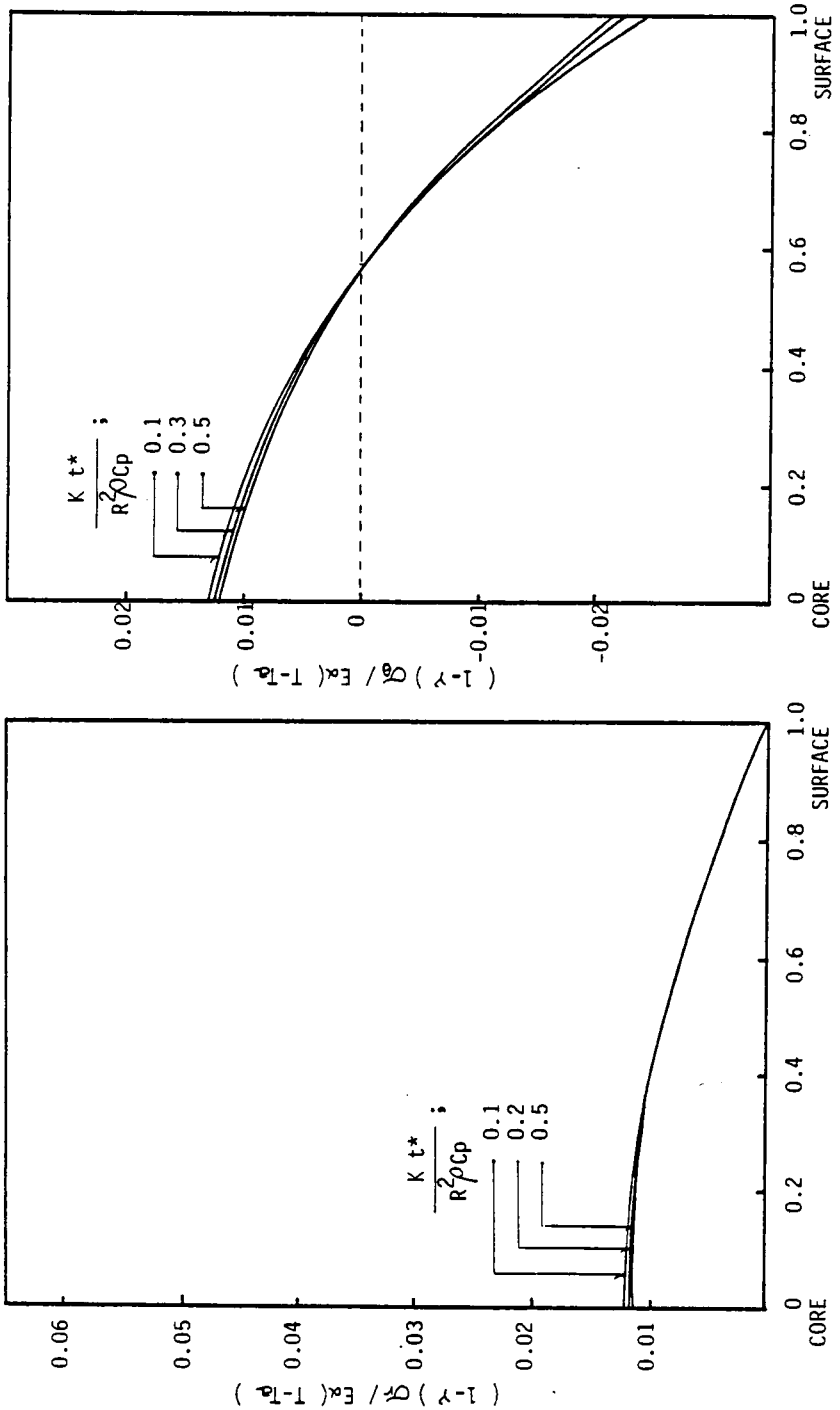


Figure VIII-2. Value of $(1 - \nu)\sigma_r/E\alpha(T - T_a)$ and $(1 - \nu)\sigma_r/E\alpha(T - T_a)$ as a function of $K\ t^*/R^2\rho C_p$ (Nusselt No. = 0.1).

more severe, the values of $(1 - \nu)\sigma_r/E\alpha\theta_0$ and $(1 - \nu)\sigma_r/E\alpha\theta_0$ will increase since thermal gradients increase. The results also illustrate the influence of value $\frac{k}{R^2\rho C_p}$ t*. The values of $(1 - \nu)\sigma_r/E\alpha\theta_0$ and $(1 - r)\sigma_\theta/E\alpha\theta_0$ are strongly affected with different dimensionless value $\frac{k}{R^2\rho C_p}$ t* in high value of Nusselt numbers. Low $\frac{k}{R^2\rho C_p}$ t* value results in high tensile stresses in the core and high compressive stresses at the surface. In other words, thick diameter, short solidification time and small diffusivity introduced this result. When the values of the Nusselt number are small the value $\frac{k}{R^2\rho C_p}$ t* does not strongly affect the residual stresses.

Residual stresses of polystyrene fibers and polycarbonate fibers were calculated for air cooling, ice water cooling and isopropanol cooling. The radius of those fibers are 0.0236 cm (V_L/V_0 = 30) and 0.112 cm (V_L/V_0 = 127). The quench becomes more severe, the magnitude of residual stresses will increase. Generally the σ_θ component is a tensile stress in the core, zero value at the surface. However, the component σ_r has only compressive stresses at the surface.

8.2. DISCUSSION

It was found that quench conditions affect the magnitude of the residual stresses. Severe quenching such as ice water cooling and isopropanol cooling results in high tensile stresses in the core and high compressive stresses at the surface. Since those quenching

introduced the high value of heat transfer coefficients and quick solidification across the radius direction. In other words, those severe quenchings have a high value of Nusselt number and dimensionless $\frac{k}{R^2\rho C_p}$ t*.

Residual stresses for polystyrene and polycarbonate fibers are shown in Figures VIII-3, VIII-4, VIII-5, VIII-6, VIII-7 and VIII-8 with three different quenching conditions: air quenching, ice water quenching and isopropanol quenching. The magnitudes of σ_θ for polystyrene fiber (V_L/V_0 = 127) were 2.5 x 10^6 pascal in the core and 4.8 x 10^6 pascal at the surface (air cooling), 5.0 x 10^7 pascal in the core and -3 x 10^8 pascal at the surface (ice water quenching) and 7.5 x 10^7 pascal in the core and -3.5 x 10^8 at the surface (isopropanol cooling). The stresses differ between the core and the surface in ice water and isopropanol quenching was larger than that due to air cooling. Fibrillated structures which we found in ice water quenched fiber may perhaps be interpreted by means of this difference. In the case of polycarbonate fiber (V_L/V_0 = 127), the magnitude of σ_θ is smaller than that of polystyrene since physical constants such as Young's modulus and thermal diffusivity are smaller than that of polystyrene. However, a similar tendency, stresses differ between a core and surface, are found.

Magnitude of σ_r for polystyrene fiber (V_L/V_0 = 127) is the same as σ_θ at a core but zero value at a surface.

It seems that radius difference does not have much affect on the residual stress because of small differences in the radius.

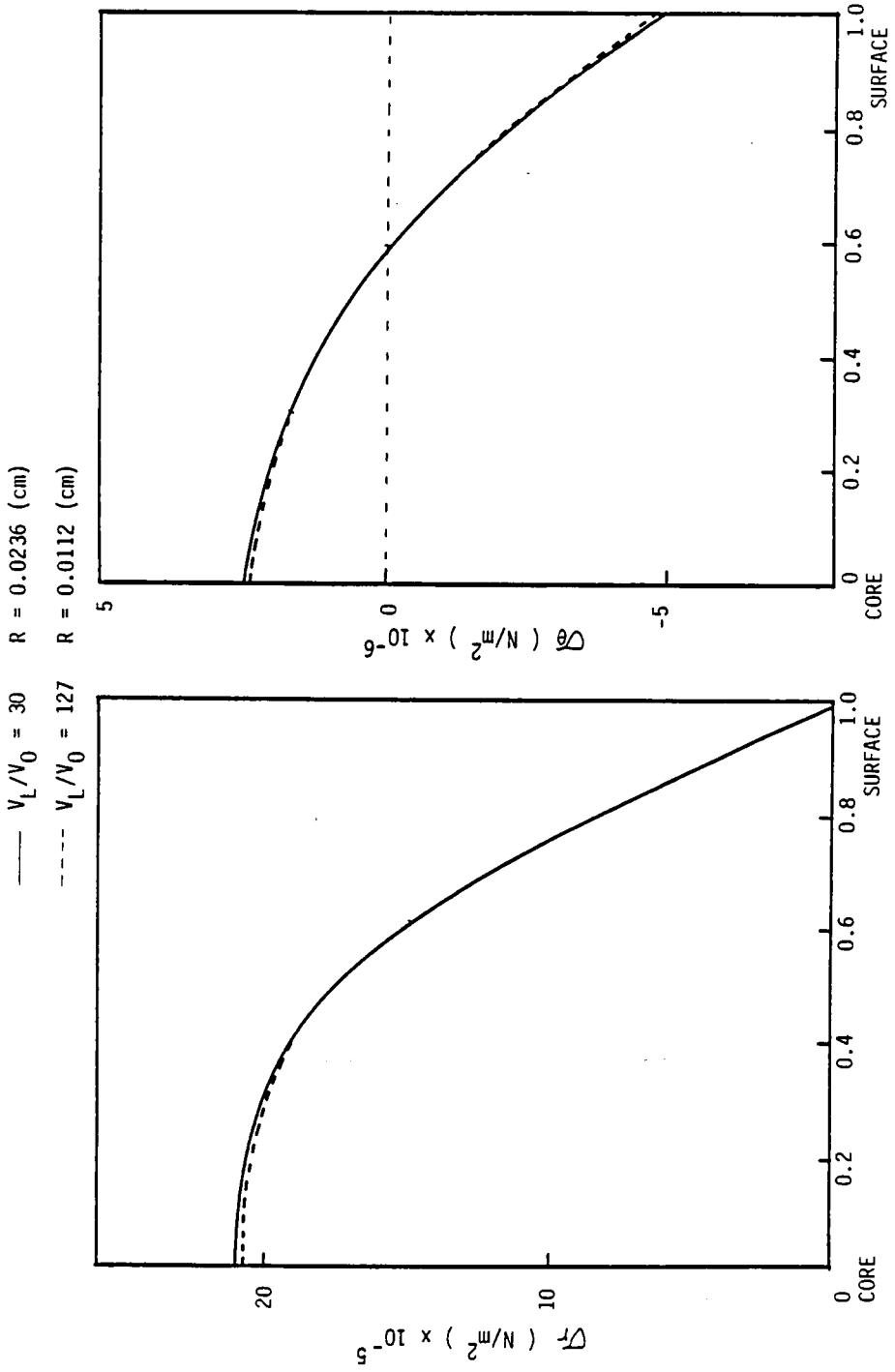


Figure VIII-3. Residual stresses for polystyrene fibers (air cooling).

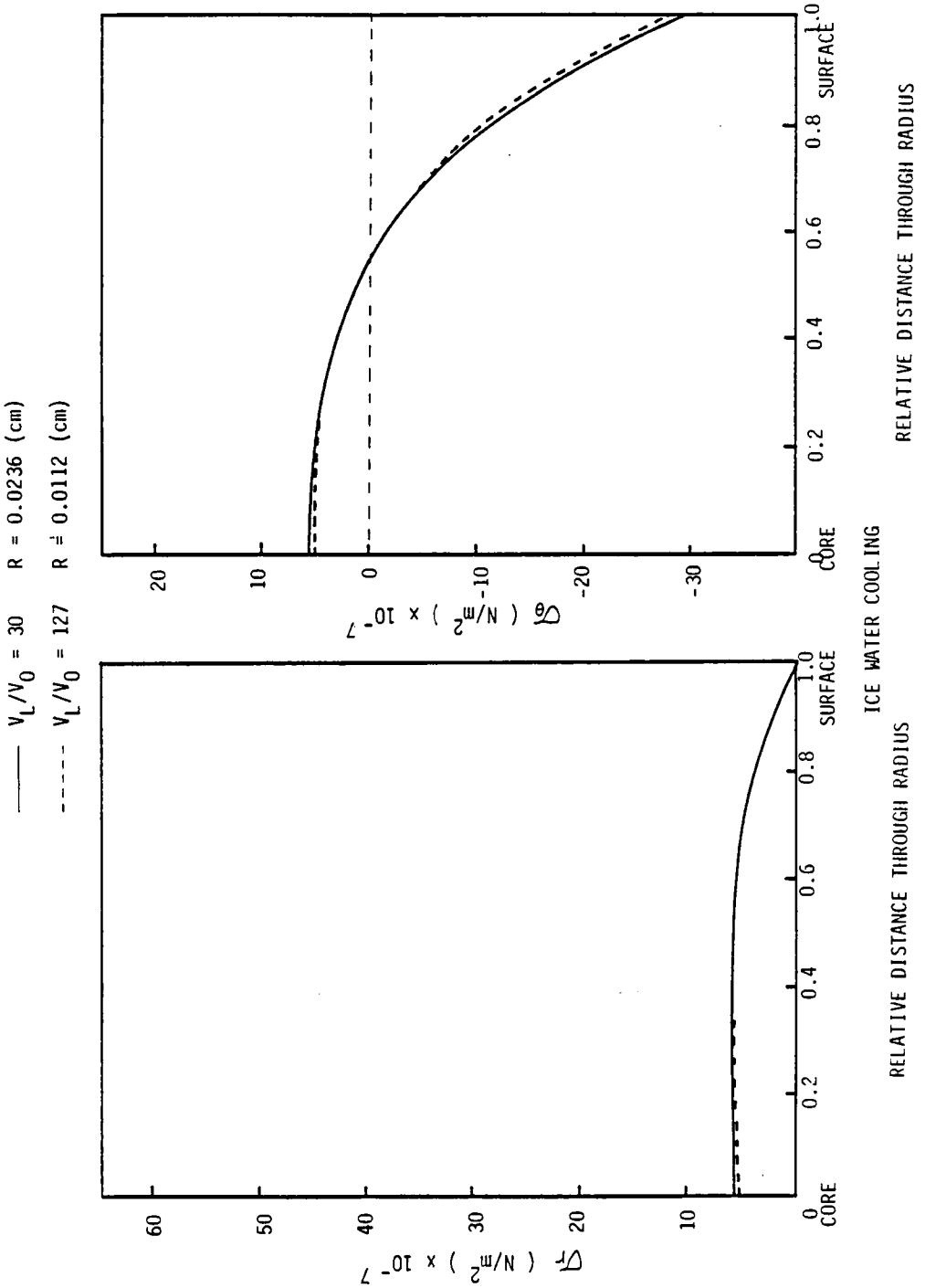


Figure VIII-4. Residual stresses for polystyrene fibers (ice water cooling).

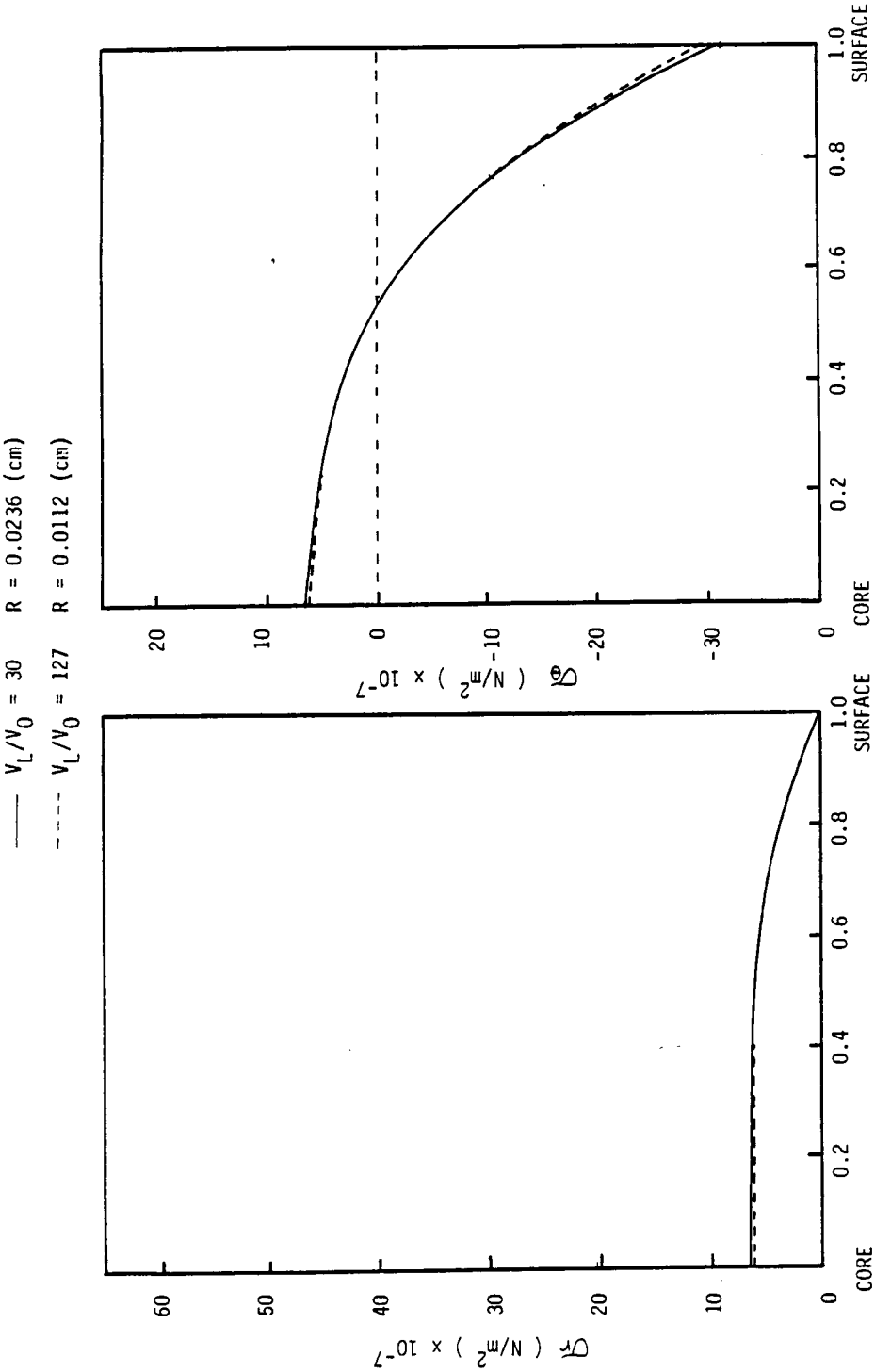


Figure VIII-5. Residual stresses for polystyrene fibers (isopropanol cooling).

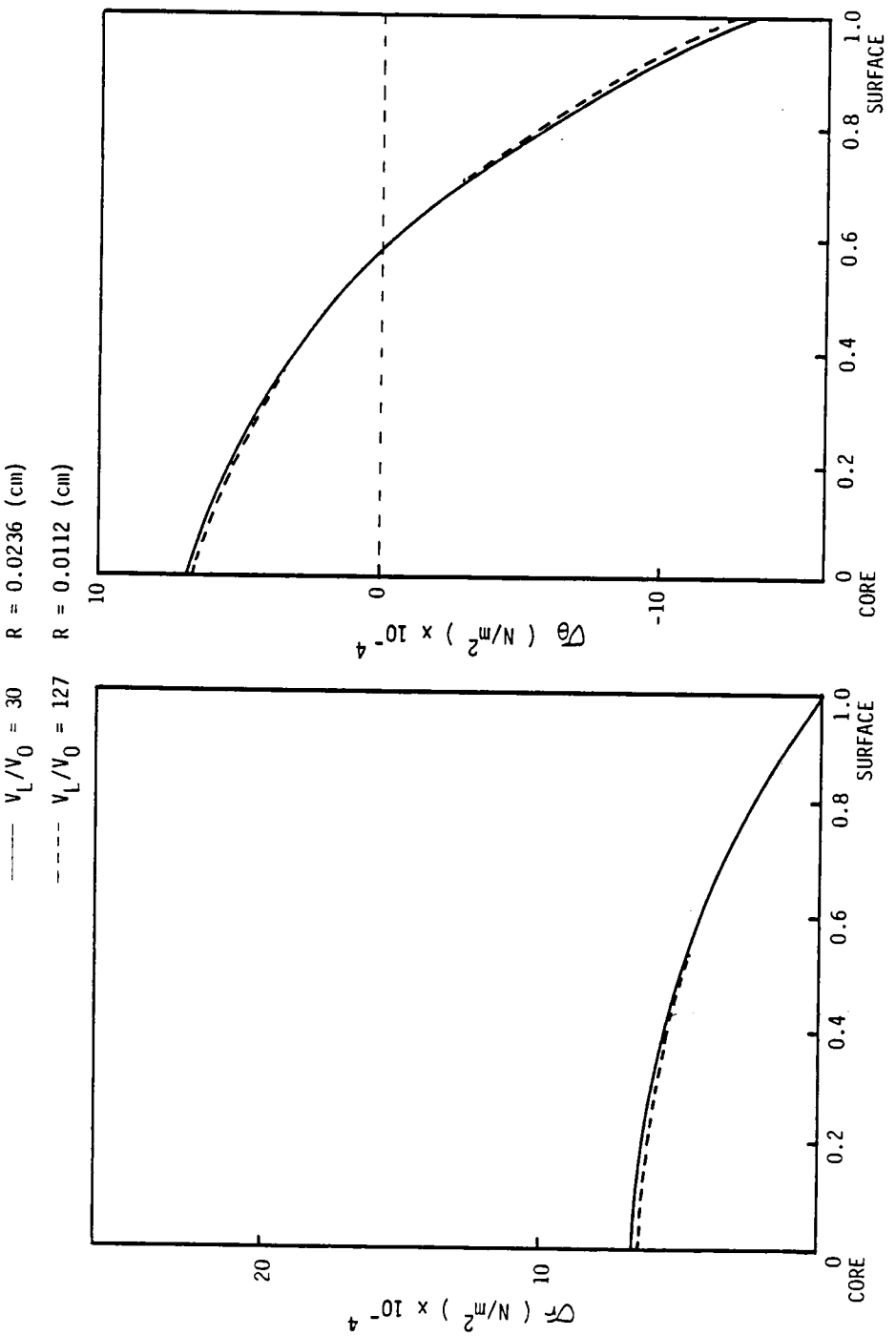


Figure VIII-6. Residual stresses for polycarbonate fibers (air cooling).

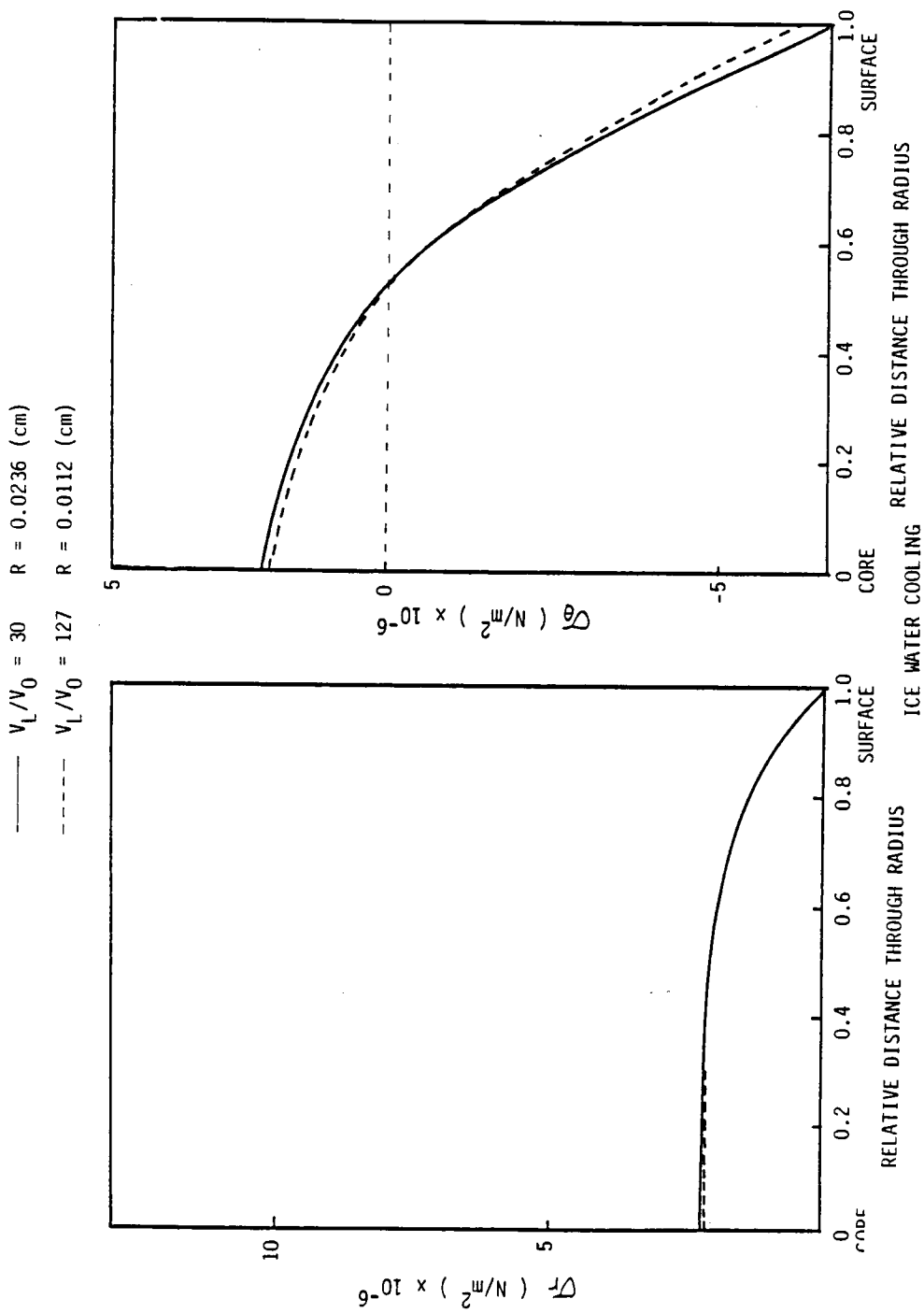


Figure VIII-7. Residual stresses for polycarbonate fibers (ice water cooling).

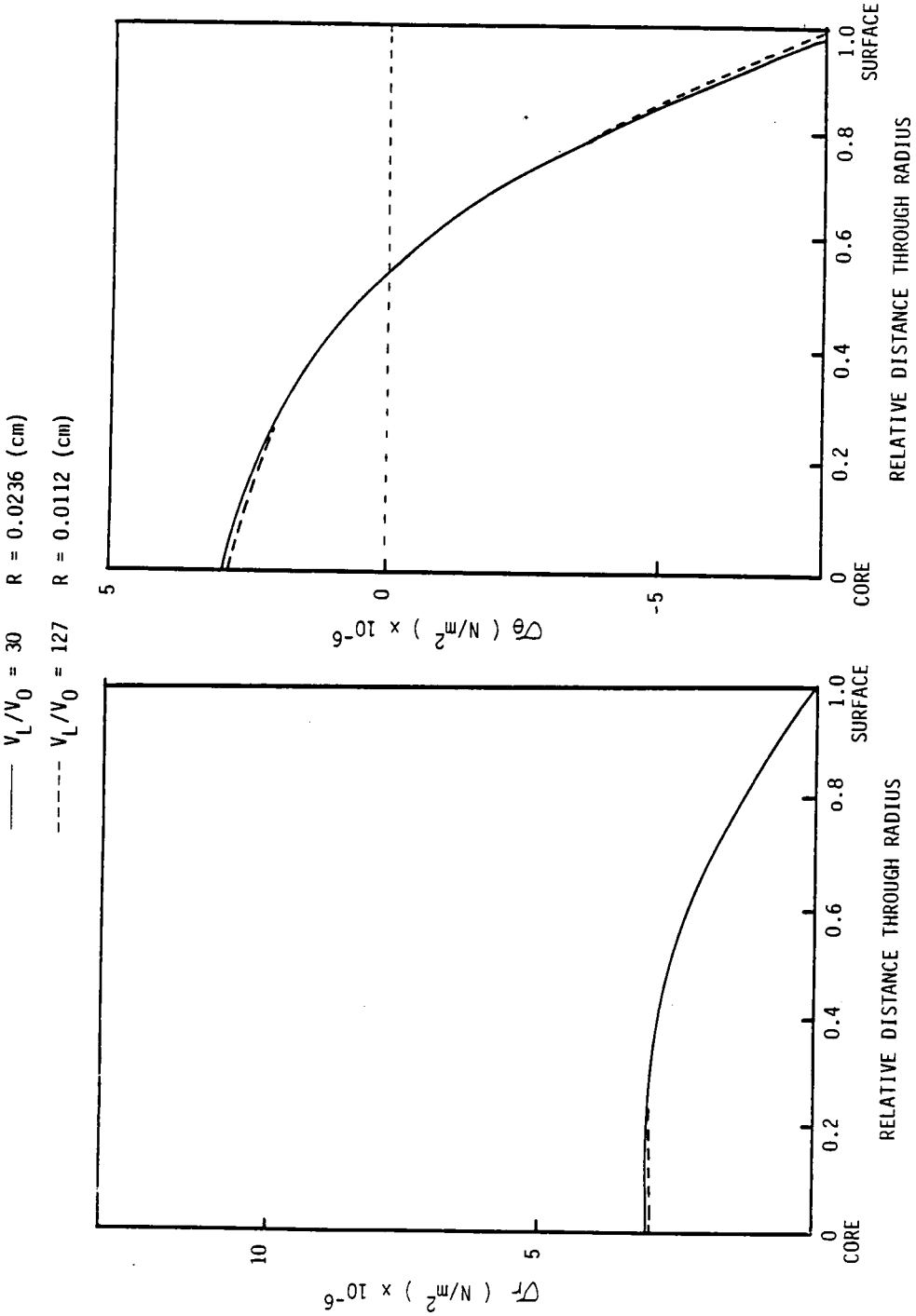


Figure VIII-8. Residual stresses for polycarbonate fibers (isopropanol cooling).

In our orientation study we found this polystyrene fiber was solidified at spinline stress (tensile stress) as 7×10^6 pascal. According to our calculation, residual stresses (σ_r) exceed the spinline stress near the surface (relative radius distance as 0.95) in the ice water quenching and isopropanol cooling. However, in air quenching residual stress does not exceed tensile stress. This might mean that fibrillated structure in severe quenching may be due to this large residual stress (σ_r) compared to the tensile stress.

From the viewpoint of tensile strength which was presented in Table VIII-1, residual stresses of ice water and propanol quenched polystyrene fiber also exceed tensile strength at the certain relative radius distance. However, the residual stresses of polycarbonate does not exceed tensile strength in any cooling systems. Generally residual stresses exceed the spinline stress or tensile strength in the severe cooling rather than in the air cooling. Consequently, fibrillated structures are more favorable in the severe quenched fiber than in the air cooled fiber.

We may conclude that fibrillated structures are caused by the two components of residual stresses. However, it is not clear which component has the main effect on fibrillated structure.

CHAPTER IX

SUMMARY AND CONCLUSION

The present work represents a major unique study about the formation of thick fibers from amorphous polymer glasses. Few concentrated investigations have been reported about the general problem of the thick fibers though the studies of thin fibers have been well established. In this research, the major emphasis was on the nonuniformity which results in nonuniform orientation distribution and residual stresses.

Linear relationships between birefringence and stresses were found for polystyrene and polycarbonate fibers. The stress optical coefficients were evaluated as -3500 Brewster for polystyrene and 5500 Brewster for polycarbonate. This behavior is independent of quenching conditions. In the case of polypropylene the behavior is not linear due to crystallization in the spinline. Low value of Δn for quenched polypropylene was found. This value may be associated with the formation of a smectic rather than monoclinic crystalline phase.

Birefringence distributions were measured with different quenching and processing conditions by measuring distances between fringes. Nonuniform distance between fringes was found—long distances near the center, short distances near the surface. Consequently birefringence distributions were obtained as high Δn

on the surface and low Δn in a core. Reduction of surface birefringence of 75 to 80% were obtained. Severe quenching and thicker diameter gave more pronounced birefringence profiles. These results were compared to the prediction of modelling.

Small amounts of crystallinity were suspected to exist in highly oriented melt spun polycarbonate fibers. This crystallinity may have an effect on relationship between birefringence and stresses. It was also found that polycarbonate can be crystallized by heat treatment and partial acetone swelling. Different histories resulted in different crystallinity.

Thermal quench stresses in melt spun fibers were modelled and established. Tensile stresses in the core were found and compressive stresses were predicted at the surface. The estimated values exceed the spinline stress and tensile strength near the surface by ice water and propanol quenched fibers.

Fibrillar structures were found in highly oriented polystyrene and polycarbonate using scanning electron microscopy. Fibrillar structures were more pronounced in severely quenched fibers. Oriented molecular chains resulted in low strength in the radical direction. High residual stresses may probably promote the fibrillar structure. SAXS experiments were also carried out. However, only low level diffuse equatorial scattering was observed indicating the level of existence of fibril on the level of hundreds of Angstroms.

REFERENCES

REFERENCES

1. Abbott, L. E. and J. L. White, Appl. Polym. Symp., 20, 247 (1973).

2. Acierno, D., J. N. Dalton, J. M. Rodriguez and J. L. White, J. Appl. Polym. Sci., 15, 2395 (1971).

3. Adams, E. B., J. C. Whitehead and D. C. Bogue, AIChE J., 11, 1026 (1965).

4. Adams, L. H. and E. D. Williamson, J. Franklin Inst., 190, 597 (1920).

5. Aggarwala, B. D. and E. Saibel, Phys. Chem. Glasses, 2, 137 (1961).

6. Alexander, L. E., "X-ray Diffraction Methods in Polymer Science," Wiley, New York (1969).

7. Andrews, E. H., Brit. J. Appl. Phys., 10, 39 (1964).

8. Andrews, R. D., J. Appl. Phys., 25, 1223 (1954).

9. Arai, T. and H. Hatta, J. Soc. Rheo. Japan, 7, 173 (1979).

10. Ballman, R. L. and H. Toor, Mod. Plastic, 38, 113 (1960).

11. Ballman, R. L. and G. B. Jackson, SPE J., 16, 1147 (1960).

12. Bartenev, G. M., "Tempering of Glass," Zh. Tekhn. Fiz., 19, 1423 (1949).

13. Beer, M., Proc. Rheo. Soc., A 236, 136 (1965).

14. Bogue, D. C. and F. N. Peebles, Trans. Soc. Rheol., 6, 317 (1962).

15. Born, M. and E. Wolf, "Principles of Optics," 4th ed., Pergamon, Oxford (1970).

16. Bower, D. I., J. Polym. Sci. Polym. Phys., 10, 2135 (1973).

17. Brewster, D., Phil. Trans. R. Soc., 106, 156 (1816).

18. Briziksky, V. I., G. V. Vinorgradov, A. I. Isayev and Y. Y. Prodolsky, J. Appl. Polym. Sci., 22, 751 (1981).

19. Broutman, L. J. and P. Sou, Poly. Eng. Sci., 16, 785 (1976).

20. Broutman, L. J. and S. M. Krishnakumar, Poly. Eng. Sci., 14, 249 (1974).

21. Broutman, L. J. and S. M. Krishnakumar, Polym. Eng. Sci., 16, 74 (1976).

22. Carslaw, H. W. and J. C. Jaeger, "Conduction of Heat in Solids," Clarendon Press, Oxford (1974).

23. Chen, I. J., G. E. Hagler, L. E. Abbott, D. C. Bogue and J. L. White, Trans. Soc. Rheology, 16, 473 (1972).

24. Clark, E. S. and C. A. Garber, Int. J. Poly. Mat., 1, 31 (1971).

25. Cleereman, K. J., H. J. Karam and J. L. Williams, Modern Plas., 30, 125 (1953).

26. Choi, K. J., J. L. White and J. E. Spruiell, A. Appl. Polym. Sci., 25, 2777 (1980).

27. Choi, K. J., J. E. Spruiell and J. L. White, J. Polym. Sci. Polym. Phys., 20, 27 (1982).

28. Conix, A. and L. Jeurissen, Adv. Chem. Series, Plasticizers and Plasticization Processes, Symposium, Philadelphia (1964).

29. Conix, A. and L. Jeurissen, L. Adv. Chem. Sci., 48, 172 (1965).

30. Corneliussen, R. and Peterlin, J., J. Polym. Sci., A2, 6, 1273 (1968).

31. Coxon, L. D. and J. R. White, Polym. Eng. Sci., 20, 230 (1980).

32. Dees, J. R. and J. E. Spruiell, J. Appl. Polym. Sci., 18, 1053 (1974).

33. Denn, M. M., C. J. S. Petrie and P. Avenas, AIChE J., 21, 791 (1975).

34. Dent, R. W. and W. S. Hearle, Text. Res. J., 30, 805 (1960).

35. Desper, C. R. and I. Kimura, J. Appl. Phys., 38, 4225 (1967).

36. Desper, C. R., Crit. Rev. Macromol. Sci., 1, 501 (1973).

37. Dinnik, A., "Applications of Bessel's Function to Elasticity Problem," Ekaterinoslav (1915).

38. Dietz, W. and J. L. White, Rheol. Acta, 17, 676 (1978).

39. Dietz, W., J. L. White and E. S. Clark, Polym. Eng. Sci., 18, 273 (1974).

40. Dumbleton, J. H., J. Polym. Sci., A-2, 6, 795 (1968).

41. Dumbleton, J. H., Textile Res. F., 40, 1035 (1971).

42. Falkai and G. Hinrichsen, J. Polym. Sci. Polym. Symp., 58, 225 (1977).

43. Fisher, R. J. and M. M. Deen, AIChE J., 22, 236 (1976).

44. Fisher, R. J. and M. M. Deen, AIChE J., 23, 23 (1977).

45. Fleissner, M., Kunstoffe, 63, 579 (1973).

46. Frasier, R. D. B., J. Opt. Soc. Am., 43, 929 (1953).

47. Frasier, R. D. B., J. Chem. Phys., 21, 1511 (1953).

48. Frasier, R. D. B., J. Chem. Phys., 28, 1113 (1958).

49. Fukutome, T., J. Conta. Micro. Tech. in Japan, 12, 9 (37).

50. Gallez, F., R. Legras and J. P. Mercier, Pol. Eng. Sci., 16, 276 (1976).

51. Gordon, M. S., J. E. Spruiell and J. L. White, J. Appl. Polym. Sci., 20, 1823 (1976).

52. Gortemaker, F. H., M. G. Hanson, B. Decindio, H. H. Laun and H. Janeshitz-Kriegl, Rheol. Acta, 16, 327 (1977).

53. Glicksman, L. R., Glass Technol., 9, 131 (1968).

54. Gurnee, E. F., J. Appl. Phys., 25, 1232 (1954).

55. Hamana, I., "39 Kagakudojin," pp. 128 (4569).

56. Hamana, I., M. Matsui and S. Kato, Meilland Textiles Berichte, 59, 382 (1969).

57. Han, C. D. and L. E. Drexler, J. Appl. Polym. Sci., 17, 2329 (1973).

58. Han, C. D., J. Appl. Polym. Sci., 19, 2403 (1975).

59. Haynes, W., "Cellulose, The Chemical that Grows," Doubleday, Garden City (1953).

60. Heckmann, W. and G. Spilgies, Koll. Z-Z Polym., 250, 1150 (1972).

61. Heckmann, W. and U. Johnoson, Colloid Polym. Sci., 252, 876 (1974).

62. Heiss, H. L., Polym. Eng. Sci., 19, 625 (1979).

63. Hermans, J. J., P. H. Hermans, D. Vermass and A. Weidinger, J. Polym. Sci., 3, 1 (1947).

64. Hermans, P. H. and P. Platzek, Kolloid Z., 88, 68 (1939).

65. Hermans, P. H. and J. Debooys, Kolloid Z., 88, 73 (1939).

66. Hermans, P. H., J. J. Hermans, D. Vermass and A. Weidinger, Rec. Tran. Chem., 65, 427 (1946).

67. Isayev, A. I., C. A. Heiber and D. L. Crouthamel, SPE ANTEC Technical Papers, 27, 110 (1981).

68. Isayev, A. I., SPE ANTEC Technical Papers, 28, 288 (1982).

69. Ishizuka, O. and K. Koyama, Polymer, 18, 913 (1977).

70. Indendom, V. L., J. Tech. Phys., 24, 925 (1954).

71. Indendom, V. L., Fizika. Tverdega Tela. Sobornik Statey, 1, 236 (1959).

72. Jager, R. C., Phil. Mag., 7, 36 (1945).

73. Janeshitz-Kriegl, H. and F. H. Gortemaker, Delft. Prog. Rep. Series, A1, 73 (1974).

74. Janeshitz-Kriegl, H., Rheol. Acta., 16, 377 (1977).

75. Janeshitz-Kriegl, H., Adv. Polym. Sci., 6, 170 (1969).

76. Jasse, B. and J. L. Koenigm, J. Macromol. Sci. Rev. Macromol. Chem., C17, 61-135 (1979).

77. Jasse, B., R. S. Chao and J. I. Koenig, J. Polym. Sci. Polym. Phys., 16, 2157 (1978).

78. Jenkins, F. A. and H. E. White, "Fundamentals of Optics," McGraw-Hill, Inc., New York (1950).

79. Kase, S. and T. Matsuo, J. Polym. Sci., A3, 2541 (1965).

80. Kase, S. and T. Matsuo, J. Appl. Polym. Sci., 11, 251 (1967).

81. Kase, S. and T. Matsuo, Appl. Polym. Sci., 20, 367 (1976).

82. Kambour, R. P., F. E. Karasz and J. H. Daane, J. Polym. Sci., Part A-2, 4, 327 (1966).

83. Katayama, K., T. T. Amano and K. Nakamura, Kolloid-Z. Polym., 226, 125 (1968).

84. Kikudani, K., Personal Communication.

85. Kitao, T., S. Ohya, J. Furukawa, and S. Yamashita, J. Polym. Sci. Polym. Phys., 11, 1091 (1973).

86. Kolb, A. F. and L. Sturkey, Dow Chemical Company (unpublished work).

87. Krigbaum, W. R. and R. J. Roe, J. Chem. Phys., 41, 737 (1965).

88. Kuhn, W. and F. Grun, Kolloid Z., 101, 248 (1943).

89. Lamonte, R. R. and C. D. Han, J. Appl. Polym. Sci., 16, 3285 (1972).

90. Lorenz, L., Ann. and Phys. and Chem., 11, 70 (1880).

91. Lees, C. H., Proc. Roy. Soc. (London), 101, 411 (1922).

92. Lee, E. H., T. G. Rogers and T. C. Woo, J. Am. Cer. Soc., 48, 480 (1965).

93. Lee, E. H. and T. G. Rogers, J. Appl. Mech., 30, 127 (1963).

94. Lodge, A. S., Trans. Faraday Soc., 52, 984 (1956).

95. Maddams, W. F. and J. F. Preedy, J. Appl. Polym. Sci., 22, 2721 (1978).

96. Maddams, W. F. and J. E. Preedy, J. Appl. Polym., 22, 2739 (1978); Ibid., 22, 2751 (1978).

97. Matsui, M. and D. C. Bogue, Polym. Eng. Sci., 16, 735 (1976).

98. Matsumoto, T. and D. C. Bogue, J. Polym. Sci., A2, 14, 1663 (1977).

99. Maxwell, J. C., "On the Equilibrium of Elastic Solids," Roy. Soc. Ed. Trans., 20, 87 (1853).

100. McBrierty, V. J. and I. M. Ward, Brit. J. Appl. Phys., 1, 1592 (1969).

101. Mercier, J. P., G. Groeninckx and M. Lesne, J. Polym. Sci. C, 16, 2059 (1967).

102. Mercier, J. and R. Legras, Poly. Lett., 8, 645 (1970).

103. Minoshima, W., M.S. Thesis, The University of Tennessee, Knoxville (1980).

104. Morey, D. R., Textile Res. J., 3, 325 (1933).

105. Morrison, M. E., AIChE J., 16, 57 (1970).

106. Muki, R. and E. Steinberg, J. Appl. Mech., 127 (1963).

107. Muller, A. C., Trans. AIChE, 38, 613 (1942).

108. Muller, F. H., Kolloid Z, 95, 136-207 (1941).

109. Nadella, H. P., H. M. Henson, J. E. Spruiell and J. L. White, J. Appl. Polym. Sci., 21, 3003 (1977).

110. Nakamura, K., T. Watanabe, T. Amano and K. Katayama, J. Appl. Polym. Sci., 16, 1077 (1972).

111. Nakamura, K., T. Watanabe, T. Amano and K. Katayama, J. Appl. Polym. Sci., 17, 1031 (1973).

112. Nakamura, K., T. Watanabe, T. Amano and K. Katayama, J. Appl. Polym. Sci., 18, 615 (1974).

113. Nomura, S., H. Kawai, I. Kimura and S. Kagiyama, J. Polym. Sci., A-2, 5, 479 (1967).

114. Nomura, S., H. Kawai, I. Kimura and S. Kagiyama, J. Polym. Sci., A-2, 8, 383 (1970).

115. Nomura, S., N. Nakamura and H. Kawai, J. Polym. Sci., A-2, 9, 407 (1971).

116. Oda, K., J. L. White and E. S. Clark, Polym. Sci. Eng., 16, 585 (1976).

117. Oda, K., J. L. White and E. S. Clark, Polym. Eng. Sci., 18, 53 (1978).

118. Omotoso, M., J. L. White and J. F. Fellers, J. Appl. Polym. Sci., 25, 1573 (1980).

119. Omotoso, M., Ph.D. Dissertation, University of Tennessee, Knoxville (1983).

120. O'Rourke, R. C. and A. W. Saenz, Quart. Appl. Math., 8, 303 (1950).

121. Pearson, J. R. A. and M. A. Matovich, IEC Fund, 8, 512 (1969).

122. Pearson, J. R. A. and Y. T. Shah, Polym. Eng. Sci., 10, 219 (1972).

123. Peilstocker, G., Brit. Plast., July, 365 (1962).

124. Philipoff, W., J. Appl. Phys., 27, 984 (1956).

125. Preston, J. M., J. Soc. Dyers. Col., 47, 312 (1931).

126. Prietzschk, A., Kolloid-A, 156, 8 (1958).

127. Rayleigh, Lord, Phil. Mag., 1, 169 (1901).

128. Reichle, A. and H. Wilsing, U. S. Patent 3,005,236 (1961).

129. Roe, R. J. and W. R. Krigbaum, J. Appl. Phys., 35, 2215 (1964).

130. Roe, R. J. and W. R. Krigbaum, J. Chem. Phys., 40, 2608 (1964).

131. Sack, R. A., J. Polym. Sci., 54, 543 (1961).

132. Samuels, R. J., J. Polym. Sci., A, 3, 1741 (1965).

133. Samuels, R. J., J. Macromol. Sci.-Phys., B4, 701 (1970).

134. Samuels, R. J. J. Appl. Polym. Sci., 26, 1383 (1981).

135. Sano, Y. and S. Nishikawa, Kagaku Kogaku, 2, 100 (1964).

136. Schael, G. W., J. Polym. Sci., 8, 2717 (1964).

137. Schael, G. W., J. Polym. Sci., 12, 903 (1968).

138. Scott, R. G., A S T M Bull., No. 257, 121 (1959).

139. Sheldon, R. P. and P. R. Blakeey, Nature, 195, 972 (1962).

140. Shimizu, J., K. Shimazaki, K. Toriumi and T. Mitsui, J. Text. Mach. Soc. Japan, 18, 125 (1972).

141. Shimizu, J. and K. Shimazaki, Sen-i-Gakkaishi, 29, T-205 (1973).

142. Shimizu, J. and K. Shimazaki, Sen-i-Gakkaishi, 29, T-443 (1973).

143. Shimomura, Y., J. E. Spruiell and J. L. White, J. Appl. Polym. Sci., 27, 1663 (1982).

144. Siegmann, A., M. Narkis and N. Rosenzweig, Polym. Eng. Sci., 19, 223 (1979).

145. Siegmann, A., A. Buchman and S. Kenig, Polym. Eng. Sci., 22, 40 (1982).

146. Sisson, W. A. and G. L. Clark, Ind. Eng. Annal Ed., 5, 296 (1933).

147. Spencer, R. S. and G. D. Gilmore, Mod. Plast., 27, 97 (1950).

148. Spruiell, J. E. and J. L. White, Polym. Eng. Sci., 15, 660 (1975).

149. Statton, W. O., J. Polym. Sci., 58, 205 (1962).

150. Stein, R. S. and F. H. Norris, J. Polym. Sci., 21, 381 (1956).

151. Stein, R. S., J. Polym. Sci., 31, 327 (1958).

152. Stein, R. S., J. Appl. Phys., 32, 1280 (1961).

153. Thakkar, B. S. and L. J. Broutman, Poly. Eng. Sci., 20, 1214 (1980).

154. Trouton, F. T., Proc. Royal Soc. (London), A77, 426 (1906).

155. Van Veld, R. D., G. Morris and H. R. Billica, J. Appl. Polym. Sci., 12, 2709 (1968).

156. Vasudevan, G. and S. Middleman, AIChE J., 16, 614 (1970).

157. Wahlstrom, E. E., "Optical Crystallography," John Wiley and Sons, Inc., New York (1950).

158. Wales, J. L. S., "The Application of Flow Birefringence to Rheological Studies of Polymer Melt," Monograph (Delft, 1976).

159. Wales, J. L. S., Rheol. Acta, 8, 39 (1969).

160. Wales, J. L. S., J. Van Leeuween and R. Vander Vigh, Polym. Eng. Sci., 12, 358 (1972).

161. Wilchinsky, Z. W., J. Appl. Polym. Sci., 7, 923 (1963).

162. Wilchinsky, Z. W., J. Appl. Phys., 30, 792 (1959).

163. White, J. L. and Y. Ide, J. Appl. Polym. Sci., 22, 3057 (1978).

164. White, J. L. and J. E. Spruiell, Polym. Eng. Sci., 21, 859 (1981).

165. White, J. L. and W. Dietz, J. Non-Newt. Fluid-Mech., 4, 299 (1979).

166. White, J. L. and A. Agrawal, Polym. Eng. Review, 1, 267 (1981).

167. Wilkes, G. L., Adv. Polym. Sci., 8, 91 (1971).

168. Woo, T. C., J. W. Jones and T. C. T. Ting, Devel. in Mech., 6, 429 (1973).

169. Yasida, H., H. Sugiyama and H. Yanggawa, Sen-i-Gakkaishi, 35, T-370 (1979).

170. Yoo, H. J. and C. D. Han, J. Rheol., 25, 115 (1981).

171. Zbinden, R., "Infrared Spectroscopy of High Polymer," Academic, New York (1964).

172. Zeichner, G., M.S. Thesis, University of Delaware (1972).

173. Ziabicki, A., Appl. Polym. Symp., 6, 1 (1967).

174. Ziabicki, A., "Man Made Fibers," Vol. 1, Ed. by H. Mark, F. Cernia and S. M. Atlas, Wiley, New York (1968).

175. Ziabicki, A., Zolloid Z., 125, 14 (1961).

176. Ziabicki, A. and K. Kedzierska, Kolloid Z., 171, 51 (1960).

APPENDIX

COMPUTER PROGRAMS

```
00010 C
00020 C
00040 C
00050 C     ***PROGRAM ' STRESS'*********************************************
00060 C     *                                                                *
00070 C     * THIS PROGRAM WAS MADE TO CALCULATE THE RESIDUAL STRESSES IN    *
00080 C     * MELT SPUN FIBERS USING O'ROURKE AND SAENZAPPROACH              *
00090 C     * THE PROGRAM    ' CALTEM ' WAS EXCUTED AS SUBROUTINE            *
00100 C     *                                                                *
00110 C     ******************************************************************
00120 C
00130 C     ****** POLYMER PROPERITIES *******
00140 C       YOUNG'S MODULUS          ;   E     (PASCAL)
00150 C       POSSIPON'S RATIO         ;   PO
00160 C       EXPANSION COEFFICIENT    :   AL
00170 C     *********************************
00180 C
00190         E=3.4D9
00200         PO=0.33


00210         AL=5.8D-4
00220 C
00230 C
00240         DIMENSION SRA(20),STA(20),SRI(20),STI(20),FOA(20),FOI(20)
00250        9         ,TEM(20),TEMI(20)
00260 C
00270         CALL CALTEM(ROA,ROI,FOA,FOI,BINA,BINI,TI,TA,TICE,TEM,
00280        9              TEMI)
00290 C
00300 C
00310         DO 10 J=1,10
00320         CA  = AL*E*(TEM(J)-TA)/(1.-PO)
00330         CI  = AL*E*(TEMI(J)-TICE)/(1.-PO)
00340         DR      = 0.1*J
00350         X =ROA*DR
00360         Y =ROA
00370         CALL CALBE(X,Y,B0X,B0Y,B1X,B1Y)
00380         SRA(J) =-2*CA*BINA*EXP(-FOA(J)*ROA**2)/(ROA*(BINA**2+ROA**2)*B0Y)
00390        9              *(B1Y-B1X/DR)
00400         STA(J) =-2*CA*BINA*EXP(-FOA(J)*ROA**2)/(ROA*(BINA**2+ROA**2)*B0Y)


00410        9              *(B1Y+B1X/DR-ROA*B0X)
00420         WRITE(6,*)  J,SRA(J),STA(J)
00430       10  CONTINUE
00440 C
00450         DO 20 J=1,10
00460         DR      = 0.1*J
00470         X =ROI*DR
00480         Y =ROI
00490         CALL CALBE(X,Y,B0X,B0Y,B1X,B1Y)
00500         SRI(J) =-2*CI*BINI*EXP(-FOI(J)*ROI**2)/(ROI*(BINI**2+ROI**2)*B0Y)
00510        9              *(B1Y-B1X/DR)
00520         STI(J) =-2*CI*BINI*EXP(-FOI(J)*ROI**2)/(ROI*(BINI**2+ROI**2)*B0Y)
00530        9              *(B1Y+B1X/DR-ROI*B0X)
00540         WRITE(6,*)  J,SRI(J),STI(J)
00550       20  CONTINUE
00560 C
00570         STOP
00580         END
```

```
00020 C
00030 C
00040 C   **** PROGRAM ' CALTEM ' ***********************************************
00050 C   *
00060 C   *    THIS PROGRAM WAS MADE TO CALCULATE THE TEMPERTURE DISTRIBUTION
00070 C   *    AND BIREFRINGENCE DISTRIBUTION.
00080 C   *    IT WAS ALSO USED TO CALCULATE RESIDUAL STRESS AS SUBROUTINE
00090 C   *
00100 C   *    TENA , SPIN , CALBE  AND CLABR WERE USED AS SUBROUTINE
00110 C   *
00120 C   *    *** SUBROUTINES ******
00130 C   *    TENA -      INPUT : POLYMER PROPERTIES ,PROCESSING CONDITIONS
00140 C   *                OUTPUT: TENSION,MEAN BIREFRINGENCE
00150 C   *    SPIN -      INPUT : OUTPUT FROM TENA ,INPUT OF TENA
00160 C   *                OUTPUT: TEMPERATURE PROFILE,VELOCITY PROFILE
00170 C   *                        HEAT TRANSFER PROFILE,RADIUS   PROFILE
00180 C   *                        NUSSELT NUMBER PROFILE
00190 C   *    CARBE-      CALCULATION FOR BESSEL FUNCTION FIRST KIND ( J0,J1)
00200 C   *    CARBR-      CALCULATION FOR ROOTS ( RO*J1(RO)/J0(RO) = NU.


00210 C   *
00220 C   ************************************************************************
00230 C
00240       DIMENSION R(100),TIM(100),TIMI(100),BIN(100),TEM(20),TEMM(20)
00250      9          ,TEMI(20),DA(100),DAI(100),T(100),TIC(100),TIMF(100)
00260      9          ,TEMA(20),TISOLA(20),TISOLI(20),FOA(20),FOI(20)
00270 C
00280 C
00290       CALL SPIN(PI,PDEN,PCP,PC,C,TI,TA,TICE,TISO,TG,II,III,T,R,RW,TIM
00300      9          ,BIN, DA,DAI,TIC,TIMI,TIMF,BINI,DXF,VW,BIR)
00310 C
00320       L       =10
00330       TIM(1)  =TI
00340 C
00350 C
00360 C
00370       WRITE(6,100)
00380       DO 10 I=30,II
00390       CALL CALBR(RO,BIN,I)
00400       P       =PC*RO**2./(PDEN*PCP*R(I)**2.)


00410 C
00420       DO 20 J=1,L
00430       X       =RO*J/L
00440       Y       =RO
00450       CALL CALBE(X,Y,B0X,B0Y,B1X,B1Y)
00460       COR     =(T(I)-TA)*RO/(2*(TI-TA)*EXP(-P*TIM(I))*B0Y)
00470       TEM(J)  =TA+2*(TI-TA)*EXP(-P*TIM(I))*B0X*COR/RO
00480       CORI    =(TIC(I)-TA)*RO/(2*(TI-TA)*EXP(-P*TIMI(I))*B0Y)
00490       TEMI(J) =TA+2*(TI-TA)*EXP(-P*TIMI(I))*B0X*CORI/RO
00500       BIRA    =BIR*VC(TEM(J))
00510       BIRI    =BIR*VC(TEMI(J))
00520       WRITE(6,200)I,J,TEM(J),BIRA,TEMI(J),BIRI
00530    20 CONTINUE
00540 C
00550    10 CONTINUE
00560 C
00570 C
00580       I=II
00590       CALL CALBR(RO,BIN,I)
00600       ROA =RO
```

```
00610          PA       =PC*ROA**2./(PDEN*PCP*RW**2.)
00620 C
00630          I=III
00640          BIN(III)=BINI
00650          CALL CALBR(RO,BIN,I)
00660          ROI      =RO
00670          PII      =PC*ROI**2./(PDEN*PCP*RW**2.)
00680 C
00690          DO 30 JJ=1,1000
00700          TIFA     =TIFA+0.0001*JJ
00710          FO       =PC*TIFA/(PDEN*PCP*RW**2.)
00720 C
00730          DO 40 J=1,L
00740          X        =ROA*J/L
00750          Y        =ROA
00760          CALL CALBE(X,Y,B0X,B0Y,B1X,B1Y)
00770          TEMA(J) =TEM(J)
00780          TEMA(J) =TA+ 2*(TEMA(J)-TA)*EXP(-PA*TIFA)*B0X*B1Y/
00790        9           ((B0Y**2+B1Y**2)*ROA)
00800          IF(TEMA(J).GE.TEM(J))GO TO 1


00810          GO TO 2
00820       1  TEMA(J) =TEM(J)
00830       2  BIRA =BIR*VC(TEMA(J))
00840          K1=I+JJ
00850      40  CONTINUE
00860          LL=L-K-1
00870          IF(TEMA(LL).LE.TG)GO TO 4
00880          GO TO  4
00890       3  K=K+1
00900          TISOLA(10)     = 0
00910          TISOLA(LL)     =TIFA
00920          FOA(10)        =PC*TISOLA(10)/PDEN*PCP*RW**2)
00930          FOA(LL)        =PC*TISOLA(LL)/PDEN*PCP*RW**2)
00940       4  CONTINUE
00950          IF(TEMA(1).LE.TG) GO TO 7
00960 C
00970      30  CONTINUE
00980       7  CONTINUE
00990 C
01000 C


01010          DO 50 JJ=1,1000
01020          TIFI     =TIFI+0.0001*JJ
01030          FO       =PC*TIFI/(PDEN*PCP*RW**2.)
01040          WRITE(6,300)
01050 C
01060          DO 60 J=1,L
01070          X        =ROI*J/L
01080          Y        =ROI
01090          CALL CALBE(X,Y,B0X,B0Y,B1X,B1Y)
01100          TEMM(J) =TEMI(J)
01110          TEMM(J) =TICE+ 2*(TEMM(J)-TICE)*EXP(-PII*TIFI)*B0X*B1Y/
01120        9           ((B0Y**2+B1Y**2)*ROI)
01130          IF(TEMM(J).GE.TEMI(J))GO TO 11
01140          GO TO 12
01150      11  TEMM(J) =TEMI(J)
01160      12  BIRI =BIR*VC(TEMM(J))
01170          K1=I+JJ
01180          WRITE(6,400)K1,J,TEMM(J),BIRI
01190      60  CONTINUE
01200          KK=L-K2-1
```

```
01210          IF(TEMM(KK).LE.TG)GO TO 13
01220          GO TO  14
01230     13   K2=K2+1
01240          TISOLI(10) =0
01250          TISOLI(KK) =TIFI
01260          F0I(10)    =PC*TISOLI(10)/(PDEN*PCP*RW**2)
01270          F0I(KK)    =PC*TISOLI(KK)/(PDEN*PCP*RW**2)
01280     14   CONTINUE
01290          IF(TEMM(1).LE.TG) GO TO 15
01300     50   CONTINUE
01310     15   CONTINUE
01320    100   FORMAT(////,30X,'** TEMPERATURE AND BIREFRINGENCE PROFILE **',//)
01330    200   FORMAT( 1X,I4,3X,I4,5X,F7.3,5X,E13.5,5X,F7.3,5X,E13.4)
01340    300   FORMAT(/,4X,'I',6X,'J',7X,'TEM',13X,'BIR',10X,'TEM',13X,'BIR')
01350    400   FORMAT( 1X,I4,3X,I4,8X,'-',15X,'-',9X,F7.3,5X,E13.4)
01360          STOP
01370          END
01380 C
01390 C
01400 C



01410          SUBROUTINE CALBR(RO,BIN,I)
01420 C
01430          DIMENSION BIN(1300)
01440          NN=4
01450          BN0=0
01460      1   BN=BN0+0.001
01470 C
01480          X      =BN0
01490          Y      =BN
01500          CALL CALBE(X,Y,B0X,B0Y,B1X,B1Y)
01510          A      =-X*B1X/B0X+BIN(I)
01520          C      =-Y*B1Y/B0Y+BIN(I)
01530          AC     =A*C
01540          BN0    =BN
01550          IF(AC.GT.0)GO TO 1
01560          RO      =BN
01570 C
01580 C
01590          WRITE(6,100)BIN(I),RO
01600          WRITE(6,200)



01610          WRITE(6,300)
01620    100   FORMAT(////,4X,'BIOT NO.=',4X,F7.5,5X,'1ST ROOT=',F7.5)
01630    200   FORMAT(/,22X,'AIR COOLING',16X,'ICE WATER COOLING')
01640    300   FORMAT(/,4X,'I',6X,'J',7X,'TEM',13X,'BIR',11X,'TEM',13X,'BIR')
01650          RETURN
01660          END
01670 C
01680 C
01690          SUBROUTINE CALBE(X,Y,B0X,B0Y,B1X,B1Y)
01700 C
01710          DIMENSION BX0(40),BY0(40),BX1(40),BY1(40)
01720 C
01730          IP1=1.
01740          IP2=1.
01750 C
01760          DO 10 M=1,6
01770          IP1= IP1*M
01780          IP2= IP2*(M+1.)
01790          BX0(M)   = (-1.)**M*X**(2.*M)/(2.**(2.*M)*IP1**2.)
01800          BY0(M)   = (-1.)**M*Y**(2.*M)/(2.**(2.*M)*IP1**2.)
```

```
01810          BX1(M)   = (-1.)**M*X**(2.*M+1)/(2.**(2.*M+1)*IP1*IP2)
01820          BY1(M)   = (-1.)**M*Y**(2.*M+1)/(2.**(2.*M+1)*IP1*IP2)
01830          IF(M.EQ.1)GO TO 1
01840          BX0(M)   =BX0(M-1 )+BX0(M)
01850          BY0(M)   =BY0(M-1 )+BY0(M)
01860          BX1(M)   =BX1(M-1 )+BX1(M)
01870          BY1(M)   =BY1(M-1 )+BY1(M)
01880          GO TO 2
01890        1 BX0(M)   =1.+BX0(M)
01900          BY0(M)   =1.+BY0(M)
01910          BX1(M)   =X/2.+BX1(M)
01920          BY1(M)   =Y/2.+BY1(M)
01930        2 CONTINUE
01940       10 CONTINUE
01950          B0X      =BX0(M)
01960          B0Y      =BY0(M)
01970          B1X      =BX1(M)
01980          B1Y      =BY1(M)
01990          RETURN
02000          END



02010 C
02020 C
02030 C
02040          SUBROUTINE SPIN(PI,PDEN,PCP,PC,C,TI,TA,TICE,TISO,TG,
02050        9   II,III,T,R,RW,TIM,BIN, DA,DAI,TIC,TIMI,TIMF,BINI,DXF,VW,BIR)
02060 C
02070          DIMENSION T(100),R(100),A(100),V(100),X(100),HE(100)
02080        9 ,DX(100),DVE(100),DA(100),DAI(100),TIM(100),BIN(100)
02090        9 ,DXI(100),XI(100),TIC(100),TIMI(100)
02100 C
02110 C
02120          CALL TENA(PI,N,PDEN,PCP,PC,C,W,G,TEN,TI,VI,RI,DI,AI,TG,VW,RW,DW,
02130        9               AW,TA,TICE,TISO,BIR)
02140 C
02150 C
02160          HEC = 4.73 D-5
02170          HECI=76.3*HEC
02180          HECP=52.2*HEC
02190 C
02200 C



02210          DT   = 2.0
02220          MN   = N-1
02230 C
02240 C
02250          T(1)      = TI
02260          A(1)      = AI
02270          R(1)      = RI
02280          V(1)      = VI
02290          X(1)      = 0
02300          TIM(1)    = 0
02310 C
02320 C
02330          WRITE(6,100)
02340          WRITE(6,200)
02350          WRITE(6,300) T(1),V(1),R(1)
02360 C
02370 C
02380          DO 10 L=2,1300
02390          T(L)         =T(1)-DT*L
02400          H            =(T(1)-T(L))/FLOAT(N)
```

```
02410           TOT          =ABS(TE(T(L)))+ABS(TE(T(1)))
02420 C
02430            DO 20 K=1,MN
02440            TOT         =TOT+2*ABS(TE(T(L)+FLOAT(K)*H))
02450    20     CONTINUE
02460           ATOT         =H*TOT/2.0
02470 C
02480 C
02490           A(L)         =(1000*TEN*PCP*PDEN**(1.334)*ATOT*G**(-0.334)
02500         9               +A(1)**(-0.167))**(-1./0.167)
02510           R(L)         =(A(L)/PI)**0.5
02520           V(L)         =G/(PDEN*A(L))
02530           HE(L)        =HEC*A(L)**(-0.334)*V(L)**(0.334)
02540           DVE(L)       =V(L)-V(L-1)
02550           DX(L)        =PCP*G**(0.666)*PDEN**(0.334)*A(L)**(0.167)
02560         9               /(1.67D-4*(T(L)-TA))
02570           DA(L)        =DVE(L)/DX(L)
02580           X(L)         =X(L-1)+DX(L)
02590           TIM(L)       =DX(L)/V(L)
02600           TIM(L)       =TIM(L-1)+TIM(L)



02610           BIN(L)       =HE(L)*R(L)/PC
02620 C
02630           XW=X(L)
02640           II=L
02650 C
02660           WRITE(6,400)L,X(L),T(L),V(L),R(L),HE(L),TIM(L),BIN(L)
02670           IF(V(L).GE.VW) GO TO 1
02680    10     CONTINUE
02690 C
02700 C
02710 C
02720     1     TIC(1) =TI
02730           XB     =5
02740 C
02750 C
02760           HEI    =HECI*AW**(-0.334)*VW**(0.334)
02770           BINI   =HEI*RW/PC
02780 C
02790 C
02800           WRITE(6,500)



02810           WRITE(6,600) TIC(1),V(1),R(1)
02820 C
02830 C
02840 C
02850           DO 30 K=2,II
02860           DXI(K)       =DX(K)*XB/XW
02870           XI(K)        =XI(K-1)+DXI(K)
02880           DAI(K)       =DVE(K)/DXI(K)
02890           TIMI(K)      =DXI(K)/V(K)
02900           TIMI(K)      =TIMI(K-1)+TIMI(K)
02910           TIC(K)       =TIC(K-1)-2*PI*R(K)*HE(K)*(TIC(K-1)-TA)*DXI(K)
02920         9               /(W*PCP)
02930 C
02940 C
02950           TAF          =TIC(K)
02960           XAF          =XI(K)
02970           TIMF         =TIMI(K)
02980 C
02990           WRITE(6,700)K,XI(K),TIC(K),V(K),R(K),HE(K),TIMI(K),BIN(K)
03000    30     CONTINUE
```

```
C
C
      III=II+1
      DXF    =(TAF-TG)*PCP*W/((TG-TICE)*PI*2*RW*HEI)
      XF     =XAF+DXF
      TIMF   =TIMF+DXF/VW
C
      WRITE(6,800)III,XF,TG,VW,RW,HEI,TIMF,BINI
C
C
C
  100 FORMAT(///,30X,'***** CALCULATION OF FIBER DYNIMIC *****'
     9       ,/,10X,//,'**** AIR COOLING ****')
  200 FORMAT(//,4X,'L',10X,'SPINLINE',8X,'TEMP',8X,'VEL',10X,'RIA',
     9        11X,'HE',10X,'TIM',10X,'BIN')
  300 FORMAT(4X,'1',13X,'-',9X,F8.2,4X,E10.3,3X,E10.3,8X,'-',11X,'-'
     9       ,12X,'-')
  400 FORMAT(1X,I4,4X,F13.4,6X,F8.2,4X,E10.3,3X,E10.3,3X,E10.3,3X,
     9        E10.3,3X,E10.3)
  500 FORMAT(///,10X,'**** ICE WATER OR PROPANOA COOLING ****',///,


     9        4X,'L',10X,'SPINLINE',9X,'TEMP',8X,'VEL',10X,'RIA',
     9        10X,'HE',10X,'TIM',10X,'BIN')
  600 FORMAT(4X,'1',13X,'-',9X,F8.2,4X,E10.3,3X,E10.3,8X,'-',11X,'-'
     9       ,12X,'-')
  700 FORMAT(1X,I4,4X,F13.4,6X,F8.2,4X,E10.3,3X,E10.3,3X,E10.3,3X,
     9        E10.3,3X,E10.3)
  800 FORMAT(1X,I4,4X,F13.4,6X,F8.2,4X,E10.3,3X,E10.3,3X,E10.3,3X,
     9        E10.3,3X,E10.3)
      RETURN
      END
C
C
       SUBROUTINE TENA(PI,N,PDEN,PCP,PC,C,W,G,TEN,TI,VI,RI,DI,AI,
     9  TG,VW,RW,DW,AW,TA,TICE,TISO,BIR)
C
C
C      ******** POLYMER PROPERTIES ************************************
C      *
C      *   POLYMER DENSITY                    ;    PDEN       (G/CM**3)


C      *   POLYMER SPECIFIC HEAT COEEF.       ;    PCP        (CAL/ G DEG C
     )
C      *   POLYMER CONDUCTIVITY               ;    PC        (CAL/SEC CM C
C      *   POLYMER TRANSIENT TEMPERATURE      ;    TG         (DEG C)
C      *   OR SOLIDIFICATIONTEMPERATURE            TP
C      *   ARHENIOUS CONSTANT                 ;    AR ,ER
C      *   STRESS OPTICS COEFFI.              ;    C          (CM**2/ DYNE
C      *
C      ******** PROCESSING CONDITIONS *********************************
C      *
C      *   FLOW INTENSITY                     ;    G          (G/SEC)
C      *   POLYMER MELT TEMPERATURE           ;    T(N)       (DEG C)
C      *      ALONG THE SPINLINE
C      *   DIAMETER AND RADIOUS               ;    D(N) ,R(N) (CM)
C      *      ALONG THE SPINLINEDW,RW
C      *   FIBER CROSS SECTION AREA           ;    A(N),AW    (CM**2)
C      *   VELOCITY ALONG THE SPINLINE        ;    V(N),VW    (CM/SEC)
C      *      AND TAKE UP VELOCITY '
C      *
C      ******** COOLING CONDITIONS ************************************
```

```
03590 C        *
03600 C        *    AIR COOLING TEMPERATURE          ;    TA        (DEG C)
03610 C        *    WATER COOLING TEMPERATURE        ;    TW        (DEG C)
03620 C        *    ISO PROPANAL COOLING TEMPERATURE ,    TI        (DEG C)
03630 C        *
03640 C        ***************************************************************
03650 C
03660 C
03670          PI        =3.1415
03680 C
03690 CC        POLYMER PROPERTIES
03700 C
03710          PDEN      =
03720          PCP       =
03730          PC        =
03740          TG        =
03750          C         =
03760 C
03770 CC       PROCESSING CONDITIONS
03780 C



03790          W         =
03800          G         =W*PDEN
03810          DI        =
03820          TI        =
03830          VW        =
03840 C
03850 C
03860          RI        =DI/2.
03870          AI        =PI*RI**2.
03880          VI        =G/(AI*PDEN)
03890          AW        =G/(VW*PDEN)
03900          DW        =2*(AW/PI)**0.5
03910          RW        =DW/2
03920 C
03930 C
03940         TA        =
03950         TICE      =
03960         TISO      =
03970 C
03980 C



03990          N         =1000
04000 C
04010          H1     =(AI-AW)/FLOAT(N)
04020          SUMA   =ABS(F(AW))+ABS(F(AI))
04030          MN=N-1
04040            DO 10 K=1,MN
04050          SUMA   =SUMA+2.*ABS(F(AW+FLOAT(K)*H1))
04060    10     CONTINUE
04070          AREAA =H1*SUMA/2.0
04080 C
04090 C
04100          H2     =(TI-TG)/FLOAT(N)
04110          SUMT   =ABS(TE(TG))+ABS(TE(TI))
04120            DO 20 K=1,MN
04130          SUMT   =SUMT+2*ABS(TE(TG+FLOAT(K)*H2))
04140    20     CONTINUE
04150          AREAT =H2*SUMT/2.0
04160 C
04170 C
04180          CON    =0.000167*G**(0.334)*PCP**(-1.0)*PDEN**(-1.334)
```

```
04190          TEN    =CON*AREAA/AREAT
04200          ST     =TEN/AW
04210          BIR    =C*ST
04220 C
04230          WRITE(6,100)
04240          WRITE(6,200)DW
04250          WRITE(6,300)TEN,ST,BIR
04260 C
04270    100   FORMAT(/,10X,'*****  MAXIMUM  BIREFRINGENCE  ,FINAL DIAMETER'
04280       9 ,',TENSION, AND STRESS *****')
04290    200   FORMAT(/,1X,'DIAMETER = ',1X,E12.5)
04300    300   FORMAT(/,1X,'TENSION A=',1X,E12.5,/,1X,'STRESS  A=',1X,E12.5,/
04310       9 ,1X,/,1X,'MAXIMUM BIREFRINGENCE   =',1X,E10.3,//)
04320          RETURN
04330          END
04340 C
04350 C
04360 C
04370          FUNCTION F(X)
04380          F=X**(-1.167)



04390          RETURN
04400          END
04410 C
04420 C
04430          FUNCTION TE(X)
04440 C
04450          AR=
04460          ER=
04470          TA=
04480 C
04490 C
04500          TE=(AR*EXP(ER/(X+273.))*(X-TA))**(-1.0)
04510          RETURN
04520          END
04530 C
04540 C
04550          FUNCTION VC(X)
04560 C
04570          AR=
04580          ER=



04590 C
04600          VC= EXP(ER/(X+273.))/EXP(ER/(100+273.))
04610          RETURN
04620          END
```

VITA

Ho-Jong Kang was born in Seoul, Korea, on November 27, 1958. In 1977, he graduated from Young-Dong High School in Seoul, and entered The Yonsei University. He received a Bachelor of Science degree with a major in Chemical Engineering in February 1982.

The author entered The University of Tennessee, Knoxville, the following September 1982 and transferred to The University of Akron as a transient student in September 1983 where he carried out his research studies in the Polymer Engineering Center.

After two years, he officially re-enrolled at The University of Tennessee, Knoxville, and received the Master of Science degree with a major in Polymer Engineering in August 1985.

On June 2, 1984, he married Jheeyoun Han.

The author is a member of the Society of Plastic Engineers.